Necessity of non-rigid body models for launch vehicles

Master Thesis

K.L. Eppenga

TUDelft

Necessity of non-rigid body models for launch vehicles

Master Thesis

by

K.L. Eppenga

Version 1.0
to obtain the degree of Master of Science
at the Delft University of Technology,
to be defended publicly on May 19, 2021 at 13:30.

Student number:	4370996
Project duration:	July 13, 2020 – May 19, 2021
Thesis supervisors:	Ir. M. C. Naeije, TU Delft, supervisor
	Ir. N. Bernving, Royal Netherlands Aerospace Centre
	Ir. A. Haagsma, Royal Netherlands Aerospace Centre

An electronic version of this thesis is available at `http://repository.tudelft.nl/`.

T̃U Delft

Preface

Before you lies my Master thesis about the necessity of non-rigid body models for launch vehicle ascent models. This report is written to obtain the degree of Master of Science at the TU Delft. It is written in accordance with the requirements of the AE5810 Thesis Space and the Royal Netherlands Aerospace Centre (NLR).

I would like to express my gratitude towards Niels Bernving and Alexander Haagsma for giving me the opportunity to work on the launch ascent simulator that has been developed by NLR for both the literature study and this thesis. I am very grateful for the trust that both supervisors put in my work and the opportunities I had to assist them with other activities within NLR as well.

I would also like to thank Marc Naeije for his supervision throughout this study. Similar to Alexander and Niels, he always showed his admiration for the work I performed, motivating me to move onwards when I got stuck. His approach to supervision was a great help in limiting stress in difficult situations.

Furthermore, I would like to thank Charles Cossette for his assistence with the energy check. His help allowed me to further deepen my knowledge of the equations of motion, enabling me to solve some very difficult problems I was facing.

Finally, I would like to express my deepest gratitude to Jildou Stapert for listening to my ramblings about sloshing masses in inertial spaces, always nodding in agreement.

K.L. Eppenga
Delft, Wednesday 28th April, 2021

Contents

Nomenclature

Acronyms

DARE   Delft Aerospace Rocket Engineering

DCM   3x3 Direction Cosine Matrix

GNC   Guidance, Navigation and Control

NLR   Royal Netherlands Aerospace Centre

SMILE   SMall Innovative Launcher for Europe

Greek Symbols

α	Angle of attack	[rad]
δ	Local deformation	[m]
$\bar{\eta}$	Mode performance (time dependent flexibility parameter)	[-]
Ψ_k	Bessel parameter	[-]
$\bar{\lambda}$	Langrangian multipliers	[-]
$\boldsymbol{\Lambda}$	Constraint matrix	[-]
μ	Deflection angle	[rad]
ρ	Density	[kg/m^3]
$\boldsymbol{\Phi}$	Modal deformation matrix	[m]
$\varphi_k(x)$	Nodal deformation parameter of the kth mode	[m]
$\boldsymbol{\Omega}$	Matrix with natural frequencies as diagonal elements	[rad/s]

Symbols

$\tilde{a}$	Deformed position of mass element w.r.t. inertial frame	[m]
$\mathbf{C}_{BI}$	Direction cosine matrix from frame i to b	
C_L	Lift coefficient	[-]
D	Vehicle diameter	[m]
d	Tank diameter	[m]
$\bar{e}$	Local deformation vector	[m]
E	Energy	[J]
$\bar{f}$	6x1 Forces and moments vector	
F	Tank fill ratio	[-]
$\bar{f}^{\text{non}}$	Euler forces	[N]

h	Tank height	[m]
$\mathbf{I}$	3x3 Inertia matrix	kgm^2
K_{slip}	Propellant slipping ratio	[-]
$\dot{m}$	Mass flow rate	[kg/s]
n	Total number of nodes	[-]
$\bar{q}$	Generalized (vehicle orientation) coordinates	[-]
r	Tank inner radius	[m]
T	Thrust	[N]
$\bar{v}$	State vector with (angular) velocities	[m/s, rad/s]
V_∞	Free stream velocity	[m/s]
$\mathbf{Z}$	Matrix with damping ratios as diagonal elements	[-]
ω	Angular velocity	rad/s

Subscripts, Superscripts and Conventions

L/D	Length over Diameter ratio	[-]
ANOVA	ANalysis Of VAriances	
B	Body motion	
c	Slosh mass center of gravity	
$\ddot{x}$	Second time derivative of x	
$\dot{x}$	First time derivative of x	
F_b	Body frame	
F_i	Inertial frame	
p	Slosh rod attachment point	
w	Inertial frame origin	
$\mathbf{X}$	Matrix X	
$\bar{x}$	Vector x	
$\bar{x}_{b/i}$	Vector x of frame i w.r.t. frame b	
x_j	Variable x of element j	
x_k	k^{th} mode of variable x	
x'	First spatial derivative of x	
z	Body frame origin (center of gravity)	

List of Figures

List of Tables

Summary

Many new initiatives are started that aim to build a competitive small-sat launch vehicle. An important parameter for these new launch vehicle designs remains weight optimisation. Higher thrust to weight ratios and smaller diameters for lower aerodynamic drag result in more noticeable elastic dynamics for a launch vehicle. In previous research, the necessity of non-rigid body simulators was stated to be a requirement for long, slender bodies. Despite past research, it remains unclear for which vehicle design parameters non-rigid body effects become destabilising.

A set of 2+N linearly independent equations of motions can be combined in a single matrix to determine the motion of a flexible launch vehicle with N slosh masses. Three different motions are considered. These are the rigid body motion, sloshing motion and flexibility motion. The flexibility of the vehicle is modelled by modelling the vehicle as a mass-spring-damper system. This method of assumed modes is often used in literature when non-rigid body models are designed. The sloshing motion is modelled by assuming that the slosh mass behaves like a pendulum. To couple the different motions, a constraint matrix is used. This modular matrix allows fixing the attachment point of the slosh mass to the *deflected* state of the vehicle. As a result, the slosh mass and flexibility motion are directly coupled by this constraint. Since the matrix is modular, the model can be extended to allow for any number N of slosh masses.

The model is developed in Matlab Simulink. Custom library blocks are used to allow for a modular set-up. Additionally, a detailed environment model is created. Different models can be chosen to simulate the Earth shape, gravity, atmosphere, wind and aerodynamics depending on the user requirements. For the launch vehicle, a custom mass model is created. The slosh mass parameters can vary, depending on the state of the vehicle. Using simplified scenarios, both the rigid body and slosh mass constraint were verified with analytical equations. This resulted in a difference of less than 0.1%. Using non-quiescent starting conditions with no external forces acting on the vehicle except gravity, it was found that the energy of the system remained constant. Since the energy of the system is conserved, it provides strong evidence that the equations of motion are implemented correctly. The model is run using a fixed-step integrator with a time step between 1E-2 and 1E-3 seconds. These settings allow the model to run faster than real-time. This means that the model can be used in embedded systems for future NLR customers.

The flight data from the Stratos III launch vehicle was obtained and compared to the simulated non-rigid body model data. It is speculated that this vehicle failed due to non-rigid body effects. It was found that slosh motion can result in destabilisation when this vehicle experiences a sudden decrease in acceleration. For Stratos III, such a decrease in acceleration could have occurred when the vehicle transitioned from the liquid to the gaseous burn phase. The destabilisation that occurred could not be observed when rigid body equations of motion were used. The non-rigid body model was able to accurately estimate the acceleration and Mach number for most of the flight but did show large inconsistencies in the roll rate.

Using ANOVA, it was found that the length, diameter, mass flow rate and fill ratio are launch vehicle design parameters that significantly influence non-rigid body effects such as sloshing and flexibility. The length-diameter interaction is also significant for flexibility. A slenderness ratio was found from which flexibility and sloshing effects become prominent. Based on a sensitivity analysis over a range of vehicle parameters, it is recommended for length over diameter (L/D) ratios above 20 to consider the use of non-rigid body models. From this ratio, the maximum and total flexibility strongly increase. A maximum deflection sensitivity was found for an L/D of 27, decreasing again for even larger ratios. This peak was attributed to an interaction between the limited sloshing motion, vehicle flexibility and aerodynamics. For L/D ratios below 20, flexibility is negligible and sloshing becomes the main perturbing factor. This suggests modelling flexibility is not required for accurate GNC models for small-sat launch vehicles which generally have an L/D below 18. It was found that a PID controller that is designed using a rigid body model is still able to stabilise the non-rigid body during flight. The error of the rigid and non-rigid body model was equivalent and both negligible for the first stage burn. This is well after the point of maximum dynamic pressure which occurred at 28 seconds. During the staging event, 2 seconds of microgravity result in a tumbling slosh mass which increases the error for the non-rigid body. Regardless, the rigid body controller was still able to correct this after second stage ignition. Oscillations occurred in both the rigid and non-rigid body model when a single set of gains was used. For both models, the oscillations were removed by introducing gain scheduling.

1

Introduction

Over the past decade, the demand for dedicated small satellite launches has steadily increased. As a result, many new initiatives are started that aim to build a competitive small-sat launch vehicle. Given the strong competition from major players such as SpaceX, new designs are required to be cost-effective. To be cost-effective, different strategies can be implemented. New, efficient engine designs, air-based launches and completely 3D printed launch vehicles are currently in development [1, 2, 24].

To increase the technological readiness of cost-effective small-sat launch vehicles, fourteen European companies and institutes have worked together on the Horizon2020 SMall Innovative Launcher for Europe (SMILE) [27]. The goal of the project was to design a launch vehicle that is able to deliver a payload of 70 kg to a (near) polar orbit and to design a launch facility in Andøya, Norway. Different vehicle designs have been considered. Commercial off-the-shelve avionics are used and 3D printed subsystems such as injectors have been manufactured and tested. Liquid and hybrid engine hot-fires have been conducted successfully. A three-stage liquid and three-stage hybrid vehicle were proposed.

An important parameter for these new launch vehicle designs remains weight optimisation. Higher thrust to weight ratios and smaller diameters for lower aerodynamic drag result in more noticeable elastic dynamics for a launch vehicle [12, 15].

In previous research, the necessity of non-rigid body simulators was stated to be a requirement for long, slender bodies. This suggest that there is a slenderness ratio from which non-rigid body effects become destabilising. Multiple non-rigid body models have been developed that aim to model these effects to allow for a more robust Guidance, Navigation and Control (GNC) system [7, 16, 30]. Generally a single vehicle is used for the non-rigid body analysis. The definition of long and slender is unclear since analysed vehicle parameters are often not presented. Mooij [17] makes use of the PacAstro launch vehicle which has a length-over-diameter (L/D) ratio of 14.6 [8]. Cossette is expected to use a similar vehicle with an L/D ratio of approximately 14 based on the Matlab visualisation. It is unclear how these vehicle would behave compared to an equivalent rigid body model since this data was not presented. Stratos III, a suborbital sounding rocket developed by the student team Delft Aerospace Rocket Engineering, had an L/D of 29.3 [9]. This vehicle is speculated to have failed due to non-rigid body effects [29]. The L/D ratio of the SMILE vehicle is 14.5. Current and historical orbital vehicles have L/D ratios between 9.4 (Ariane V) and 18.9 (Falcon 9). An overview of L/D ratios of 5 well-known orbital launch vehicles is presented in Table 1.1. For newly developed launch vehicles it might be interesting to determine which L/D ratios require extra attention due to non-rigid body effects. Despite current research, it remains unclear for which vehicle design parameters non-rigid body effects become destabilising.

In this research, a non-rigid body model is developed based on existing models in literature. The rigid body equations of motion are extended to include launch vehicle flexibility. This motion is modelled using the method of assumed modes [20]. Slosh masses are included by adding pendulums. This results in a set of linearly independent equations of motion that can be solved simultaneously. This model is equivalent to the implementation proposed by Cossette [7]. The model is extended by including various environmental settings to determine the aerodynamic loads on the vehicle during flight. The three-stage SMILE vehicle is modelled as a liquid bi-propellant with 6 slosh masses, one for each propellant tank. The model is also designed in a Simulink environment which allows for rapid controller prototyping and easier hardware implementation.

1

Table 1.1: L/D ratios of past and current launch vehicles

Vehicle	Developer	Length [m]	Diameter [m]	L/D [-]	Source
Falcon 9	SpaceX	70	3.7	18.9	[25]
Electron	Rocket Lab	18	1.2	15	[23]
Ariane V	ArianeGroup	50.5	5.4	9.35	[4]
Soyuz-2	Progress Rocket Space Centre	46.2	2.95	15.7	[5]
Saturn V	NASA	110	10.1	10.9	[18]

This research aims to answer the following question:

Are non-rigid body models required to keep the SMILE small-sat launch vehicle stable during ascent?

Where the following sub-questions considered:

Q1 *Which launch vehicle parameters play a significant role in determining the sensitivity for non-rigid body motion?*

Q2 *For which values of the parameters from Q1 is the use of non-rigid body models recommended?*

Q3 *Can rigid body model controllers succesfully stabilise non-rigid body small-sat launch vehicles?*

A sensitivity analysis is performed that aims to determine for which parameter values non-rigid body effects become most prevalent. Simple PID controllers are used to determine the difference in control response between rigid and non-rigid launch vehicles.

In Chapter 2, a summary of available non-rigid body models in literature is presented. In Chapter 3, an overview of the Simulink model implementation is given. The model implementation is verified in Chapter 4. The model validity for sounding rockets is determined using flight data in Chapter 5. Finally, the non-rigid body sensitivity parameters and critical values are determined in Chapter 6.

2

Literature study summary

In [10], a modular mathematical model was derived that allowed for the propagation of a non-rigid launch vehicle. The non-rigid body effects are estimated through mechanically equivalent modelling. Propellant sloshing effects are approximated using a normal pendulum and flexibility effects are estimated with the method of assumed modes. In this chapter, a detailed derivation of the equations of motion is presented. This derivation includes the forces and moments acting on the different elements in the equations of motion.

2.1. Rigid body equations of motion

In this section, the equations of motion for a rigid body are derived. Although this derivation has already been performed many times in literature, it is once more presented here to give a complete overview of the modular equations of motion.

A body B is assumed to be a rigid body with constant mass m_B and centre of gravity z in the body frame F_b moving in an inertial frame F_i with its origin located in point w. A graphical representation of the system is given in Figure 2.1. Its kinetic energy is given by

$$E_{kin} = \frac{1}{2} m_B (\bar{v}^{wz})^2 + \frac{1}{2} \bar{\omega}^{b/i} \mathbf{I}^B \bar{\omega}^{b/i} \tag{2.1}$$

where $\bar{\omega}^{b/i}$ represents the angular velocity of frame F_b with respect to F_i. $\mathbf{I}^B$ is the second mass moment of inertia of body B about point z. To use Lagrangian Mechanics to find the equations of motion of this rigid body, it is assumed that at an initial point, the body has no potential energy and the generalized coordinate is chosen to be

$$\bar{q} = \begin{pmatrix} \bar{r}_i^{zw} \\ \bar{q}^{bi} \end{pmatrix} \tag{2.2}$$

where $\bar{r}_i^{zw}$ represents the position vector from point w to point z, resolved in F_i. Vector $\bar{q}^{bi}$ represents the generalized coordinates of the attitude parameters. It should be noted that this can be Euler angles, quaternions, the nine elements of a Direction Cosine Matrix stacked in a $[9x1]$ vector or any other representation that the user requires. The Lagrange Equation can be used to find

$$\begin{bmatrix} m_B \dot{\bar{v}}_i^{zw/i} \\ \mathbf{J}_b^{Bz} \dot{\bar{\omega}}_b^{bi} + \bar{\omega}_b^{bi\times} \mathbf{J}_b^{Bz} \bar{\omega}_b^{bi} \end{bmatrix} = \begin{bmatrix} \bar{f}_i^B \\ \bar{m}_b^{Bz} \end{bmatrix} + \mathbf{\Lambda}^\top \lambda \tag{2.3}$$

where the forces and moments on the rigid body are indicated by $\bar{f}_i^B$ and $\bar{m}_b^{Bz}$.
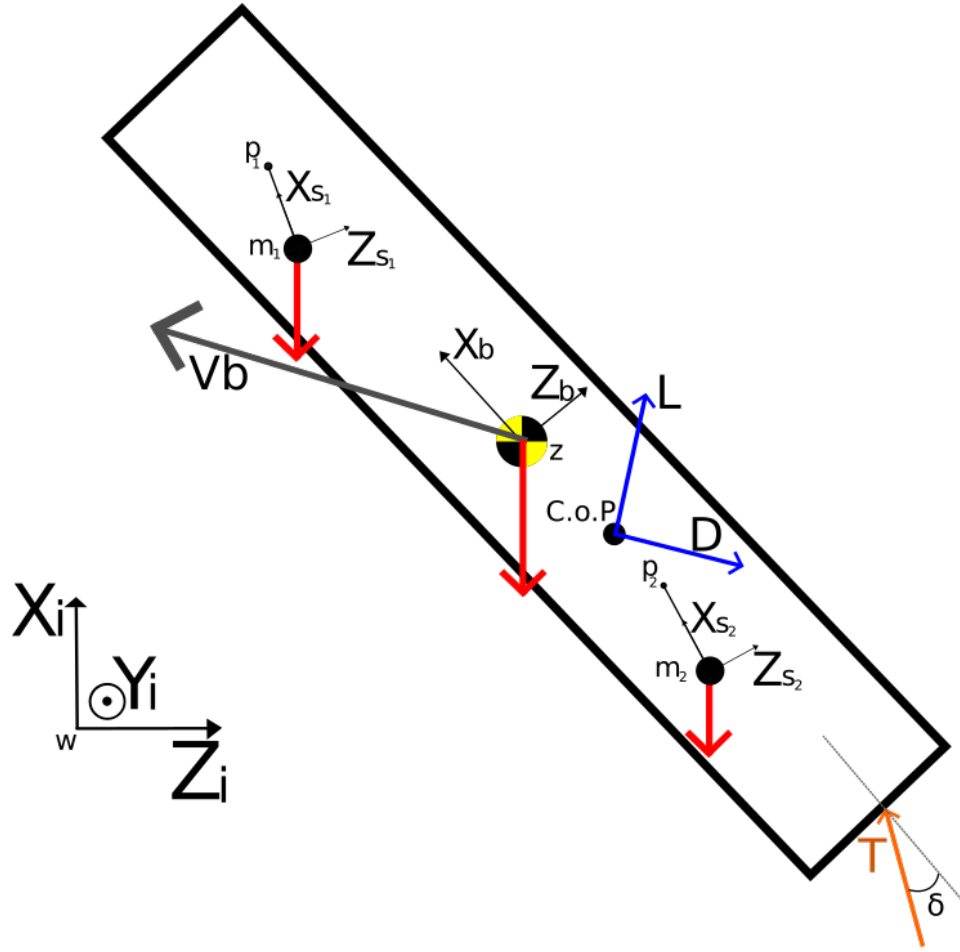
Figure 2.1: Free body diagram of the rigid body

The skew-symmetric matrix $\bar{\omega}_b^{bi\times}$ is defined as

$$\bar{\omega}_b^{bi\times} = \begin{bmatrix} 0 & -\bar{\omega}_b^{bi}(3) & \bar{\omega}_b^{bi}(2) \\ \bar{\omega}_b^{bi}(3) & 0 & -\bar{\omega}_b^{bi}(1) \\ -\bar{\omega}_b^{bi}(2) & \bar{\omega}_b^{bi}(1) & 0 \end{bmatrix} \tag{2.4}$$

Matrix $\mathbf{\Lambda}$ represents a constraint matrix with Lagrangian multipliers λ that is chosen such that, as shown by Forbes [11]

$$\mathbf{\Lambda}\bar{v} = 0 \quad ; \quad \bar{v} = \begin{bmatrix} \bar{v}_i^{zw/i} \\ \bar{\omega}_b^{bi} \end{bmatrix} \tag{2.5}$$

It should be noted that $\bar{v} \neq \dot{q}$ as the derivative of the generalized coordinates is generally not equal to the angular velocity of the body. The result of Equation (2.3) can be rewritten to a more familiar form

$$\underbrace{\begin{bmatrix} m_{\mathcal{B}}1 & 0 \\ 0 & \mathbf{J}_b^{Bz} \end{bmatrix}}_{\mathbf{M^B}} \underbrace{\begin{bmatrix} \dot{\bar{v}}_i^{zw/i} \\ \dot{\bar{\omega}}_b^{bi} \end{bmatrix}}_{\dot{v}^{\mathbf{B}}} + \underbrace{\begin{bmatrix} 0 \\ \bar{\omega}_b^{bi\times}\mathbf{J}_b^{Bz}\bar{\omega}_b^{bi} \end{bmatrix}}_{\bar{f}^{\mathrm{non},\mathbf{B}}} \underbrace{\begin{bmatrix} \bar{f}_i^B \\ \bar{m}_b^{Bz} \end{bmatrix}}_{f^B} + \mathbf{\Lambda}^{\top}\lambda \tag{2.6}$$

Which is shortened to

$$\mathbf{M}^B \dot{\bar{v}}^B + \bar{f}^{\mathrm{non,B}} = \bar{f}^B + \mathbf{\Lambda}\bar{\lambda} \tag{2.7}$$

where $\bar{f}^{\mathrm{non},B}$ represent the addition of the Euler rotation equation due to the body frame being a non-inertial frame. This set of equations can be considered a well-known set of equations for rigid body motion.

The external forces couple the rigid body motion with the motion of the flexibility and slosh masses. The forces acting on the vehicle are the gravity, aerodynamic forces and thrust. The gravity also acts on the slosh masses. If these masses don't lie directly in line with the center of gravity of the vehicle, the slosh mass creates a moment acting on the rigid body. The free body diagram can be seen in Figure 2.1. In Equation (2.6), the forces are resolved in the inertial frame. The moments are resolved in the body frame.

Using Figure 2.1, it becomes clear that the force vector acting on the rigid body can be defined as the sum of gravity, aerodynamic forces and thrust, resulting in

$$\bar{f}_i^B = m\bar{g} + \mathbf{C}_{bi}^T \mathbf{C}_{ba} \bar{f}^{\mathrm{aero}} + \mathbf{C}_{bi}^T \mathbf{C}_{bt} \bar{T} \tag{2.8}$$

Where the frame transformation from the inertial to the body frame is given by the Direction Cosine Matrix (DCM) $\mathbf{C}_{bi}$. The frame transformation from the aerodynamic frame to the body frame is given by $\mathbf{C}_{ba}$. The transformation from the engine (thrust) frame to the body frame is given by $\mathbf{C}_{bt}$.

The moment equation is given by

$$\bar{m}_B^B = r_B^{ez} \times \bar{T} + \bar{m}_B^{aero} \tag{2.9}$$

The slosh masses do not contribute explicitly in the force and moment equation of the rigid body since this interaction will be handled by the constraint that is applied in Section 2.4. Although it is not explicitly placed in the moment equation for the rigid body, it can be seen that destabilising effects can occur due to propellant slosh. The slosh masses will cause the center of gravity to move in the $Y_B - Z_B$ plane. Assuming that the equivalent thrust is generally pointing through the axis of symmetry of the vehicle, the thrust itself will cause a destabilizing moment within the vehicle.

2.2. Flexibility equations of motion - Method of assumed modes

The equations of motion that describe the flexibility of the vehicle are described in this section. The flexibility equations of motion make use of the method of assumed modes [20], which requires eigenmode analysis of a given structure.

The method of assumed modes makes use of the natural vibration modes of a structure. Different node locations of the system are used. The actual displacement of this node can be described with a linear combination of natural vibration modes at a given node. This is then summed to achieve the final deformation of this node. The deformation itself is given with respect to the rigid body. A graphical representation of a rocket and its first bending mode is given in Figure 2.2.

This method is often used when flexible rocket bodies are modelled [7, 14, 26, 30]. The deflections of rockets are generally small and the axi-symmetry of most launch vehicles allow for relatively simple equivalent beam models. Following the procedure as described by Li [14], an undeformed, rigid launch vehicle is considered. This launch vehicle can be modelled as a simple beam. This beam is discretised in n elements. The position of the center of mass of the vehicle relative to the inertial frame is given by $\bar{r}^{wz}$. Parameter $\bar{r}^{w\tilde{a}}$ represents the position of the jth mass element relative to the inertial frame. In Figure 2.2, it can be seen that $\bar{r}^{w\tilde{a}} = \bar{r}^{wz} + \bar{r}^{z\tilde{a}}$, where $\bar{r}^{z\tilde{a}} = \bar{r}^{za} + \bar{e}$ is the position of the mass element relative to the body-fixed coordinates. Position vector $\bar{r}^{za}$ can be considered the position of the jth mass element as if the body was modelled as a rigid body. Vector $\bar{e}$ is specifically of interest, as this defines the position of the mass element in its deformed shape. The method of assumed modes calculates this vector according to

$$\bar{e} = \begin{pmatrix} 0 \\ \delta_y \\ \delta_z \end{pmatrix} = \begin{pmatrix} 0 \\ \sum_{k=1}^n \eta_k(t)\varphi_k(x) \\ \sum_{k=1}^m \zeta_k(t)\varphi_k(x) \end{pmatrix} \tag{2.10}$$
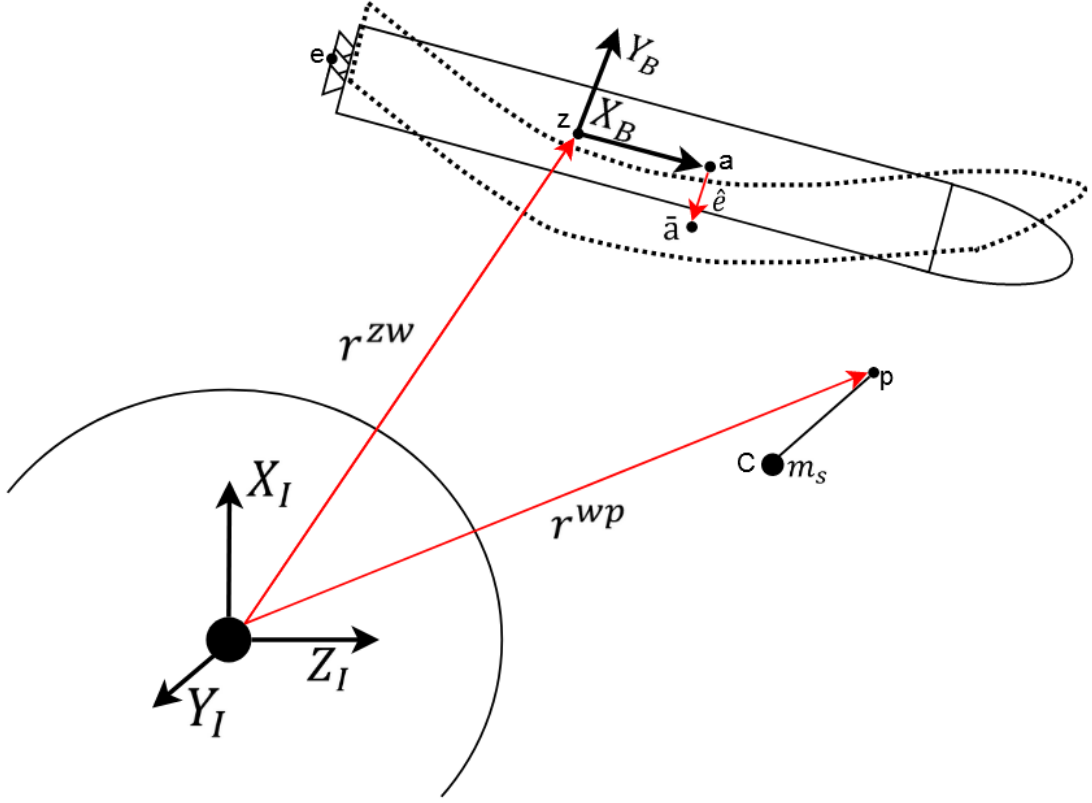
Figure 2.2: Graphical representation for derivation of the equations of motion

where δ_y and δ_z are the local deformations of the mass element around the y and z axis. The local deformation in the Y_B and Z_B axis are considered to affect the aerodynamic properties of the vehicle. For axial deformation, this effect is limited if no buckling occurs. Therefore, the local deformation in the x axis is assumed to be negligible. Parameters $\eta_k(t)$ and $\zeta_k(t)$ can be considered the performance parameter of the kth mode and are dependent on time. As stated above, since most launch vehicles can be considered axisymmetric, the kth mode shapes around both axis are considered to be equal. Parameter $\varphi_k(x)$ indicates the nodal deformation of the k_{th} mode and is dependent on the axial location of the node.

Equation (2.10) can be rewritten in matrix form to obtain

$$\bar{e} = \sum_{k=1}^{n} \bar{\eta}_k(t) \mathbf{\Phi}_k \tag{2.11}$$

$$\bar{\mu} = \bar{e}' = \sum_{k=1}^{n} \bar{\eta}_k(t) \mathbf{\Phi}_k' \tag{2.12}$$

where $\mathbf{\Phi}_k$ is the modal deformation matrix. The matrix $\mathbf{\Phi}_k'$ is the spatial derivative of $\mathbf{\Phi}_k$, which is a direct result the well-known Euler-Bernoulli beam theory. Euler-Bernoulli beam theory assumes small displacements. For orbital launch vehicles, this is considered a valid assumption. If this is not the case, Timoshenko beam theory [28] should be applied and the nodal rotation matrix described as $\mathbf{\Phi}_k'$ should be determined separately.

Applying Lagrangian mechanics to Equation (2.11) following Hang and Cossette [7, 30], the equations of motion of the flexible body can be written as

$$\ddot{\bar{\eta}}_k + 2\mathbf{Z}\boldsymbol{\Omega}\dot{\bar{\eta}}_k + \boldsymbol{\Omega_k}^2\bar{\eta}_k = \bar{f}^\eta \tag{2.13}$$

where $\mathbf{Z}$ and $\boldsymbol{\Omega}$ correspond to the natural frequency and damping coefficient of the kth mode, where the values are placed in the diagonal of a $k \times k$ matrix. These values can be obtained by performing a modal analysis on the design. This analysis can be performed by a variety of Finite Element Analysis programs such as ANSYS. The result of this modal analysis is a mass-normalized nodal displacement of selected nodes, as well as the eigenfrequency of each mode. The modal deformation matrices $\boldsymbol{\Phi_k}$ of the different nodes is given by these displacements. The number of modes that is considered can be set by the program. A larger number of modes is expected to increase the model accuracy at the cost of additional computational time.

Parameter $\bar{f}^\eta$ represents the force that excites the flexible modes. For the model proposed by Cosette, this includes only the thrust force. This is also used in this model. It is recommended to consider adding the aerodynamic forces as well to increase the accuracy of this model.

To achieve this, a new coordinate system $X_v Y_v Z_v$ is defined. Equivalent to the aerodynamic coordinate system, the X_v axis is aligned with the velocity vector of the centre of gravity of the body. Y_v is orthogonal to X_v in the $X_B Y_B$ plane and Z_v completes the right-hand system. The additional angle of attack over the vehicle length due to vehicle deflection is given by

$$\alpha_1(x) = \sum_{k=1}^{n} \varphi'_{yk} q_{yk} \tag{2.14}$$

Next, Hang provides the aerodynamic damping angle caused by the rotation of the body and the elastic deformation velocity

$$\alpha_2(x) = -\omega_z \frac{x}{|V^{wz}|} - \frac{\dot{u}(x, y, z, t)}{|V^{wz}|} \tag{2.15}$$

where $|V^{wz}|$ represents the magnitude of $\bar{V}^{wz}$ and x is the location along X_B. This results in a total angle of attack equal to

$$\alpha_T(x) = \alpha + \underbrace{\sum_{k=1}^{n} \varphi'_{yk} q_{yk}}_{\alpha_1} \underbrace{- \omega_z \frac{x}{|V^{wz}|} - \frac{\dot{u}(x, y, z, t)}{|V^{wz}|}}_{\alpha_2} \tag{2.16}$$

Next, the vehicle is sub-divided into a set of infinitesimally small strips along the length of the vehicle. The lift on each strip is modelled as if it had an infinite span. This method is called strip theory, and can be used to find the lift coefficient $C_L(x)$ of the vehicle according to

$$C_L(x) = \frac{dC_L}{d\alpha}\alpha(x) = C'_L \alpha(x) \tag{2.17}$$

With this equation, the lift of an infinitesimally small body section can be written by rewriting the lift equation to

$$d_L(x) = \frac{1}{2}\rho V_\infty^2 l(x) C'_A \alpha(x) dx \tag{2.18}$$

where ρ is the air density and V_∞ is the free stream velocity. Integrating this over the length of the body, the total lift on the vehicle is found to be

$$Lift = \int_0^L \frac{1}{2}\rho V_\infty^2 l(x) C'_A (\alpha + \sum_{k=1}^{n} \varphi'_{yk} q_{yk} - \omega_z \frac{x}{|V^{wz}|} - \frac{\dot{u}(x, y, z, t)}{|V^{wz}|}) dx \tag{2.19}$$
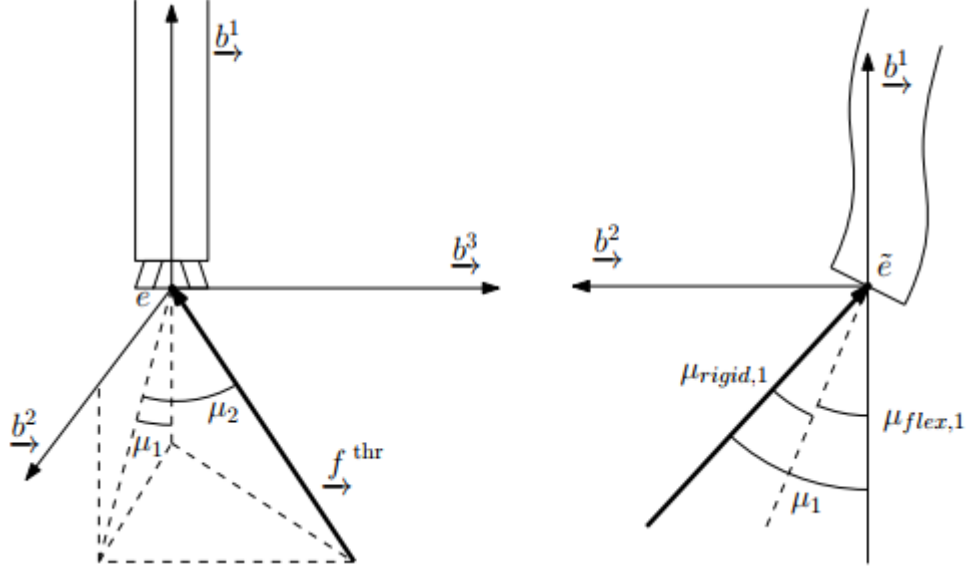
Figure 2.3: Definition of effective thrust angle due to deformations [7]

This integration can't be solved analytically since the modal deformation is discretised in nodes. The lift per node can be established and summed to obtain the total lift over the vehicle. Similar strategies can be applied to obtain the drag and side loads.

For the thrust force, Figure 2.3 is considered. The thrust force can be defined as

$$\bar{f}_B^{thr} = |\bar{f}_B^{thr}| \begin{bmatrix} \cos(\mu_1)\cos(\mu_2) \\ -\sin(\mu_1)\cos(\mu_2) \\ -\sin(\mu_2) \end{bmatrix} \approx |\bar{f}_B^{thr}| \begin{bmatrix} 1 \\ -\mu_1 \\ -\mu_2 \end{bmatrix} = |\bar{f}_B^{thr}| \begin{bmatrix} 1 \\ -(\mu_{\text{rigid},1} + \mu_{\text{flex},1}) \\ -(\mu_{\text{rigid},2} + \mu_{\text{flex},2}) \end{bmatrix}$$
(2.20)

where small engine deflection angles are assumed. The engine deflection due to body flexibility is given by

$$\mu_{\text{flex}} = \sum_{k=1}^{n} \Phi'^{,k} \eta_k$$
(2.21)

which is resolved at the engine connection point e. The induced moment also changes due to this deflection and can be written as

$$\bar{m}_B^{thr} = (\bar{r}^{\tilde{e}e} + \bar{r}^{ez})^{\times} \bar{f}_B^{thr}$$
(2.22)

2.3. Sloshing equations of motion

The sloshing motion of the liquid is approximated by using an equivalent mechanical representation. A normal pendulum attached to the launch vehicle body is used. The sloshing propellant is lumped together in an equivalent mass rigid body. Such a model has been proposed in multiple papers [3, 7, 19].

There are two elements that are considered. The first element is the lumped propellant mass that is close to stationary. This propellant mass is modelled similarly to a full rigid body simulator where the mass, inertia and center of gravity are calculated as if the propellant is a solid cylinder with uniform density. The second element is the slosh mass itself. This is modelled as a moving normal pendulum. The angle of the pendulum is equivalent to the portion of mass that sloshes for a given mode. As an example, a single pendulum for the first sloshing mode is shown in Figure 2.4. Subscripts j and k represent the tank number and mode number respectively.
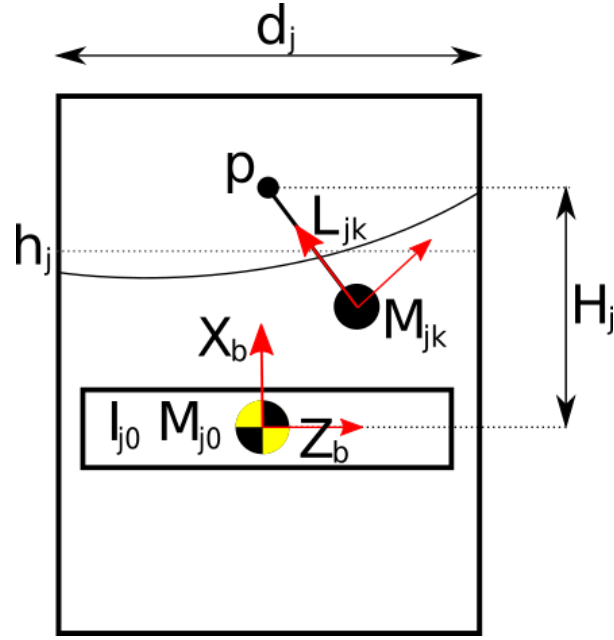
Figure 2.4: Equivalent pendulum model for propellant sloshing.

Table 2.1: Parameter overview for the pendulum sloshing model

	Fixed mass	**Sloshing mass**
Represents	Propellant mass that does not contribute to sloshing forces	Propellant mass that contributes to sloshing forces
Mass	M_{j0}	m_{jk}
Inertia	I_{j0}	I_{jk}
Location	Origin	H

A set of moveable masses m_{jk} is distributed along the X_b axis when the tank is at rest, represented as pendulums with a massless rod of length L_{jk}.

The liquid tanks are assumed to be spherical. From Roberts [22], an analytical solution can be found for the parameters in the pendulum system. First, a new parameter κ_j is defined

$$\kappa_j = \frac{\Psi_k h_j}{d_j} \tag{2.23}$$

where h_j is the liquid height and d_j is the tank diameter. The parameter Ψ_k represents the kth root of the Bessel function derivative of the first kind and order which values are tabulated by Roberts. The Bessel equation is given as

$$J_k(x) = x^2 y'' + x^2 y' + (x^2 - n^2)y = 0 \tag{2.24}$$

This equation has two linearly independent solutions for a fixed value n. For a circular liquid tank, the standing wave solution can be expressed as the Bessel function of the first kind when $J_k(d_j/2) = 0$. Only the first sloshing mode will be analysed. For this sloshing model, it can be assumed that the first sloshing mode is the most present, meaning that only $k = 1$ needs to be considered. This results in a value for the Bessel function parameter $\Psi_1 = 1.84119$. Subscript k is dropped to increase clarity.

Next, Roberts and Amani [3] find for the model elements that the slosh mass m_j in terms of total fluid mass m_{tot_j} is given by

$$m_j = m_{tot_j}[\frac{2\tanh{(\kappa_j)}}{(\Psi2-1)\kappa_j}] \tag{2.25}$$

The total fluid mass m_{tot_j} can be simply calculated when a spherical tank is assumed using

$$m_{tot_j} = \frac{pi}{4}\rho_j h_j d_j^2 - \int_0^t (\dot{m}) \tag{2.26}$$

where ρ_j is the density of the propellant in tank j and $\dot{m}$ is the mass flow rate.

The length of the pendulum defines the natural frequency of the liquid. The natural frequency of the liquid depends on the diameter of the tank and the liquid level. It can be calculated using

$$L_j = \frac{g}{\omega_j^2} = \frac{d_j}{\Psi_k \tanh \kappa_j} \tag{2.27}$$

where ω_j is the natural frequency of the liquid in tank j. Parameter g is the acceleration on the pendulum. The position of the mass on the pendulum with respect to the center of moment of the liquid is given to be

$$H_j = L_j + \frac{h_j}{2} - [\frac{4h_j}{\kappa_j}\tanh\frac{\kappa_j}{2}] \tag{2.28}$$

A portion of the propellant has no sloshing effect. This fixed mass is simply calculated using

$$m_{j0} = m_{tot_j} - \sum_1^j m_j \tag{2.29}$$

The equations of motion can simply be added to the set of equations, since the pendulum can be considered as a new rigid body. Using the parameters above, Equation (2.6) can be used for the slosh pendulum as well. The mass will then be simply m_j for each sloshing mass that is considered. The inertia tensor is the inertia through the body center of gravity. The inertia of the slosh mass is calculated by multiplying the inertia of the complete tank with the fraction of the slosh mass to the total mass. The inertia calculation will be further explained in Section 4.1.3.

The force acting on the slosh mass becomes more complex due to the interaction of the attachment point and the rigid body. A slosh mass below the rigid body center of gravity is shown on the left in Figure 2.5 with the corresponding free body diagram of the slosh mass on the right.

In Figure 2.5, the launch vehicle undergoes an angular and inertial acceleration. The angular acceleration of the launch vehicle results in a displacement of the slosh mass from its neutral position. When the launch vehicle rotates in the Y_B+ direction, the slosh mass moves in the Y_S- direction from the perspective of the sloshing frame. The location of the slosh mass in inertial space is set by means of a constraint in the equations of motion, which can be seen in Section 2.4.2. This constraint will take into account all interactions between the rigid body and the slosh mass. Therefore, it is only required to apply the external forces and moments, which can be expressed as

$$\sum F_S = \sum_{i=1}^N m_{s_i} * \bar{g}_I + F_{damp_{i_I}} \tag{2.30}$$

where the acceleration due to gravity is given by $\bar{g}$. This acceleration vector should be resolved in the inertial frame, and can be determined by using different environment models. These models are further explained in Section 3.2. $F_{damp_{i_I}}$ represents the damping forces acting on the slosh mass.

The slosh masses are modelled as point masses. Therefore, the moments on the slosh mass simply become

$$\sum M_S = \bar{0} \tag{2.31}$$
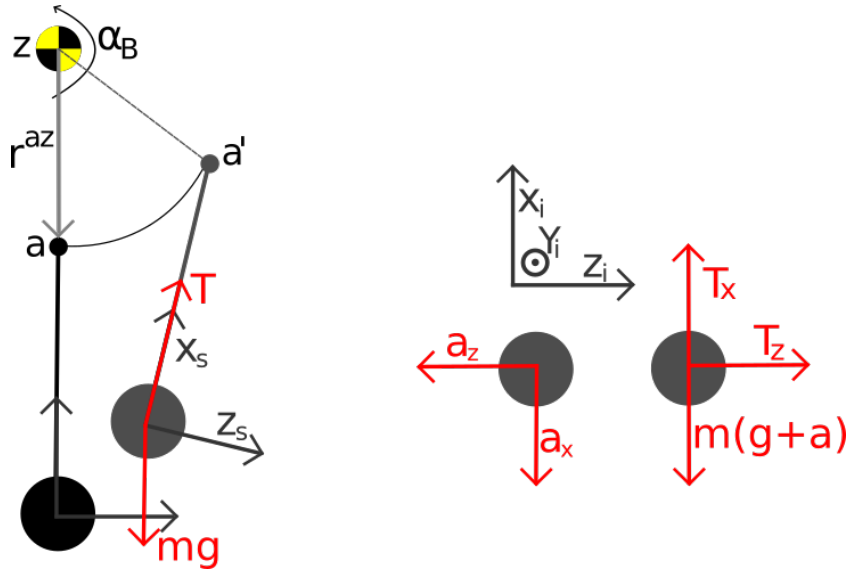
Figure 2.5: Slosh mass below the body center of gravity [L] and free body diagram [R]

2.4. Combining the motions with constraints

In this section, the different equations of motion are combined in a single set of independent equations that can be solved simultaneously. First, the equations of motion are combined in Section 2.4.1. In Section 2.4.2, the constraints for the slosh mass are derived and implemented in the system. In Section 2.4.3, constraint propagation is removed to eliminate constraint drift.

2.4.1. Combining the motions

In the previous sections, different equations of motion where derived. Since these equations of motion are linearly independent, they can be combined in a single matrix notation. The rigid body motion is described by Equation (2.7). For each slosh mass that is added, the rigid body mass and orientation parameters in Equation (2.7) are changed to the sloshing mass and orientation parameters. Combining Equation (2.7) and Equation (2.13), the equations of motion for a single slosh mass become

$$
\begin{bmatrix} \mathbf{M}^B & 0 & 0 \\ 0 & 1 & 0 \\ 0 & 0 & \mathbf{M}^S \end{bmatrix} \begin{bmatrix} \dot{\bar{v}}^B \\ \ddot{\bar{\eta}} \\ \dot{\bar{v}}^S \end{bmatrix} + \begin{bmatrix} 0 & 0 & 0 \\ 0 & 2\mathbf{Z}\mathbf{\Omega} & 0 \\ 0 & 0 & 0 \end{bmatrix} \begin{bmatrix} \bar{v}^B \\ \dot{\bar{\eta}} \\ \bar{v}^S \end{bmatrix} + \begin{bmatrix} 0 & 0 & 0 \\ 0 & \mathbf{\Omega}^2 & 0 \\ 0 & 0 & 0 \end{bmatrix} \begin{bmatrix} \bar{q}^B \\ \bar{\eta} \\ \bar{q}^S \end{bmatrix}
$$
$$
+ \begin{bmatrix} \bar{f}^{\text{non}B} \\ 0 \\ \bar{f}^{\text{non}S} \end{bmatrix} = \begin{bmatrix} \bar{f}^B \\ \bar{f}^\eta \\ \bar{f}^S \end{bmatrix} + \mathbf{\Lambda}\bar{\lambda}
$$

(2.32)

These equations can be extended for an arbitrary amount of rigid bodies and slosh masses if the constraints in $\mathbf{\Lambda}$ are implemented correctly. For an arbitrary number of slosh masses n, the equations of motion can simply be extended as shown in Equation (2.33).

$$
\begin{bmatrix}
\mathbf{M}^B & 0 & 0 & \dots & 0 & 0 \\
0 & 1 & 0 & \dots & 0 & 0 \\
0 & 0 & \mathbf{M}_1^{S1} & \dots & 0 & 0 \\
\vdots & \vdots & \vdots & \vdots & \vdots & \vdots \\
0 & 0 & 0 & \dots & \mathbf{M}_{n-1}^{SN-1} & 0 \\
0 & 0 & 0 & \dots & 0 & \mathbf{M}_n^{SN}
\end{bmatrix}
\begin{bmatrix}
\dot{\bar{v}}^B \\
\ddot{\bar{\eta}} \\
\dot{\bar{v}}_1^{S1} \\
\vdots \\
\dot{\bar{v}}_{n-1}^{SN-1} \\
\dot{\bar{v}}_n^{SN}
\end{bmatrix}
+
\begin{bmatrix}
0 & 0 & 0 & \dots & 0 & 0 \\
0 & 2\mathbf{Z}\mathbf{\Omega} & 0 & \dots & 0 & 0 \\
0 & 0 & 0 & \dots & 0 & 0 \\
\vdots & \vdots & \vdots & \vdots & \vdots & \vdots \\
0 & 0 & 0 & \dots & 0 & 0
\end{bmatrix}
\begin{bmatrix}
\bar{v}^B \\
\dot{\bar{\eta}} \\
\bar{v}_1^{S1} \\
\vdots \\
\bar{v}_n^{SN}
\end{bmatrix}
+ \dots
$$

$$
\dots
\begin{bmatrix}
0 & 0 & 0 & \dots & 0 & 0 \\
0 & \mathbf{\Omega}^2 & 0 & \dots & 0 & 0 \\
0 & 0 & 0 & \dots & 0 & 0 \\
0 & 0 & 0 & \dots & 0 & 0 \\
\vdots & \vdots & \vdots & \vdots & \vdots & \vdots \\
0 & 0 & 0 & \dots & 0 & 0
\end{bmatrix}
\begin{bmatrix}
\bar{q}^B \\
\bar{\eta} \\
\bar{q}_1^{S1} \\
\vdots \\
\bar{q}_n^{SN}
\end{bmatrix}
+
\begin{bmatrix}
\bar{f}^{\text{non}B} \\
0 \\
\bar{f}_1^{\text{non}S1} \\
\vdots \\
\bar{f}_n^{\text{non}SN}
\end{bmatrix}
=
\begin{bmatrix}
\bar{f}^B \\
\bar{f}^\eta \\
\bar{f}_1^{S1} \\
\vdots \\
\bar{f}_1^{SN}
\end{bmatrix}
+ \mathbf{\Lambda}\bar{\lambda}
$$

$$(2.33)$$

2.4.2. Slosh mass constraints

The matrix $\mathbf{\Lambda}$ contains the constraints associated with the system. For this model, one constraint is applied. It is obtained by the assumption that the attachment point of the pendulum (on the pendulum) p is fixed to the deformed position of the actual attachment point on the vehicle $\hat{a}$, rather than the attachment point on the non-deformed vehicle a. Similar to Cossette [7], the constraint can be written such that

$$\bar{r}_i^{\hat{a}w} = \bar{r}_i^{pw} \tag{2.34}$$

$$\bar{r}_i^{\hat{a}a} + \bar{r}_i^{aw} = \bar{r}_i^{pw} \tag{2.35}$$

which can be rewritten in terms of the elastic coordinates $\bar{\eta}$

$$\mathbf{C}_{ib}\mathbf{\Psi}_b^a\bar{\eta} + \bar{r}_i^{ai} = r_i^{pi} \tag{2.36}$$

where $\mathbf{\Psi}_b^a$ is the modal matrix at the node which is fixed to a. This constraint is not yet in the form of $\mathbf{\Lambda}\bar{v} = 0$. To achieve this it is required to take the time-derivative. Making use of the Poisson equation $\dot{\mathbf{C}}_{bi} = -\bar{\omega}_b^{bi}\mathbf{C}_{bi}$, the time derivative becomes

$$\dot{\mathbf{C}}_{ib}\Psi_b^a\bar{\eta} + \mathbf{C}_{ib}\Psi_b^a\dot{\bar{\eta}} + \bar{v}_i^{aw/i} - \bar{v}_i^{pw/i} = 0$$

$$\left(-\bar{\omega}_b^{bi\times}\mathbf{C}_{bi}\right)^\top \Psi_b^a\bar{\eta} + \mathbf{C}_{ib}\Psi_b^a\dot{\bar{\eta}} + \left(\bar{v}_i^{az/i} + \bar{v}_i^{ai/i}\right) - \left(\bar{v}_i^{pe/i} + \bar{v}_i^{ci/i}\right) = 0 \tag{2.37}$$

Next, the transport theorem is used. Using the definition of the transport theorem

$$\dot{\bar{x}}^{F_1} = \dot{\bar{x}}^{F_2} + \omega^{F_1 F_2} \times \bar{x} \tag{2.38}$$

results in

$$\left(\mathbf{C}_{ib}\bar{\omega}_b^{bi\times}\right)\Psi_b^a\bar{\eta} + \mathbf{C}_{ib}\Psi_b^a\dot{\bar{\eta}} + \left(\bar{v}_i^{az/b} + \bar{\omega}_i^{bi\times}\bar{r}_i^{az} + \bar{v}_i^{zw/i}\right) - \left(\bar{v}_i^{pc/s} + \bar{\omega}_i^{si\times}\bar{r}_i^{pc} + \bar{v}_i^{cw/i}\right) = 0$$

$$-\mathbf{C}_{ib}\left(\Psi_b^a\bar{\eta}\right)^\times \bar{\omega}_b^{bi} + \mathbf{C}_{ib}\Psi_b^a\dot{\bar{\eta}} - \mathbf{C}_{ib}\bar{r}_b^{az\times}\omega_b^{bi} + \bar{v}_i^{zw/i} + \mathbf{C}_{is}\bar{r}_s^{pc\times}\bar{\omega}_s^{si} - \bar{v}_i^{cw/i} = 0 \tag{2.39}$$

which can finally be put in the correct form

$$\underbrace{\left[\begin{array}{cccc} 1 & -\mathbf{C}_{ib}(\mathbf{\Psi}_b^a\bar{\eta} + \mathbf{r}_b^{az})^{\times} & \mathbf{C}_{ib}\mathbf{\Psi}_b^a & -1 \quad \mathbf{C}_{is}\mathbf{r}_s^{pc\times} \end{array}\right]}_{\Lambda} \underbrace{\begin{bmatrix} \bar{v}_i^{zw/i} \\ \bar{\omega}_b^{bi} \\ \dot{\eta} \\ \bar{v}_i^{cw/i} \\ \bar{\omega}_s^{si} \end{bmatrix}}_{\bar{v}} = 0 \qquad (2.40)$$

2.4.3. Eliminating constraint drift

Although the constraint of Equation (2.40) allows the user to solve the equations of motion, the Lagrangian multipliers need to be integrated besides the rigid body equations of motion, which can induce constraint drift over time. Therefore Cossette proposes the use of the null space method to remove the constraint integration. First, a new set of coordinates is defined that follows

$$\bar{v} = \mathbf{\Upsilon}\hat{\bar{v}} \qquad (2.41)$$

where $\hat{v}$ is the new set of independent velocities and $\mathbf{\Upsilon}$ lies in the null space of Λ, meaning that

$$\Lambda\bar{v} = 0 \qquad (2.42)$$
$$\Lambda\mathbf{\Upsilon}\hat{v} = 0 \qquad (2.43)$$
$$\Lambda\mathbf{\Upsilon} = 0 \qquad (2.44)$$
$$(\mathbf{\Upsilon}\Lambda)^T = 0 \qquad (2.45)$$

When the constraint is applied, the inertial velocity of the slosh mass becomes redundant since this velocity is described as a function of the other state parameters. As a result, the new parameter $\mathbf{\Upsilon}$ becomes

$$\begin{bmatrix} \bar{v}_i^{zw/i} \\ \omega_b^{bi} \\ \dot{\eta} \\ \bar{v}_i^{cw/i} \\ \omega_s^{si} \end{bmatrix} = \underbrace{\begin{bmatrix} 1 & 0 & 0 & 0 \\ 0 & 1 & 0 & 0 \\ 0 & 0 & 1 & 0 \\ 1 & -\mathbf{C}_{ib}\left(\mathbf{\Psi}_b^a\bar{\eta} + \bar{r}_b^{az}\right)^x & \mathbf{C}_{ib}\mathbf{\Psi}_b^a & \mathbf{C}_{is}\bar{r}_s^{zc} \\ 0 & 0 & 0 & 1 \end{bmatrix}}_{\mathbf{\Upsilon}} \begin{bmatrix} \bar{v}_i^{zw/i} \\ \omega_b^{bi} \\ \dot{\eta} \\ \omega_s^{si} \end{bmatrix} \qquad (2.46)$$

This constraint matrix can also be adapted to include multiple slosh masses. For an arbitrary number of slosh masses, the contraint matrix $\mathbf{\Upsilon}$ becomes

$$\mathbf{\Upsilon} = \left[\begin{array}{ccc|cccc} 1 & 0 & 0 & 0 & \dots & 0 \\ 0 & 1 & 0 & 0 & \dots & 0 \\ 0 & 0 & 1 & 0 & \dots & 0 \\ \hline 1 & -\mathbf{C}_{ib}\left(\mathbf{\Psi}_b^a\bar{\eta} + \bar{r}_b^{az}\right)^x & \mathbf{C}_{ib}\mathbf{\Psi}_b^a & \mathbf{C}_{is}\bar{r}_s^{zc} & \dots & 0 \\ 0 & 0 & 0 & 1 & \dots & 0 \\ \vdots & \vdots & \vdots & \vdots & \vdots & \vdots \\ 1 & -\mathbf{C}_{ib}\left(\mathbf{\Psi}_b^a\bar{\eta} + \bar{r}_b^{az}\right)^x & \mathbf{C}_{ib}\mathbf{\Psi}_b^a & 0 & \dots & \mathbf{C}_{is}\bar{r}_s^{zc} \\ 0 & 0 & 0 & 0 & \dots & 1 \end{array}\right] \qquad (2.47)$$

Knowing that

$$\mathbf{\Upsilon}^T\Lambda^T = 0 \qquad (2.48)$$
$$\dot{\bar{v}} = \dot{\mathbf{\Upsilon}}\hat{v} + \mathbf{\Upsilon}\dot{\hat{v}} \qquad (2.49)$$

the final equations of motion can be obtained by pre-multiplying Equation (2.32) with $\mathbf{\Upsilon}^T$, resulting in

$$\mathbf{\Upsilon}^\top \mathbf{M} \mathbf{\Upsilon} \dot{\hat{v}} + \mathbf{\Upsilon}^\top \mathbf{M} \dot{\mathbf{\Upsilon}} \hat{v} + \mathbf{\Upsilon}^\top \mathbf{D} \mathbf{\Upsilon} \hat{v} + \mathbf{\Upsilon}^\top \mathbf{K} \bar{q} + \mathbf{\Upsilon}^\top \mathbf{f}^{\mathrm{non}} = \mathbf{\Upsilon}^\top \bar{f} \tag{2.50}$$

In order to solve for $\dot{\hat{v}}$, Equation (2.50) is rewritten to

$$\underbrace{(\mathbf{\Upsilon}^\top \mathbf{M} \mathbf{\Upsilon})}_{A} \dot{\hat{v}} = \underbrace{\mathbf{\Upsilon}^\top \bar{f} - \mathbf{\Upsilon}^\top \mathbf{M} \dot{\mathbf{\Upsilon}} \hat{v} - \mathbf{\Upsilon}^\top \mathbf{D} \mathbf{\Upsilon} \hat{v} - \mathbf{\Upsilon}^\top \mathbf{K} \bar{q} - \mathbf{\Upsilon}^\top \bar{f}^{\mathrm{non}}}_{b} \tag{2.51}$$

which can be solved for $\dot{\hat{v}}$ by multiplying the inverse of matrix A with the vector b, resulting in

$$\dot{\hat{v}} = (\mathbf{\Upsilon}^\top \mathbf{M} \mathbf{\Upsilon})^{-1} * (\mathbf{\Upsilon}^\top \bar{f} - \mathbf{\Upsilon}^\top \mathbf{M} \dot{\mathbf{\Upsilon}} \hat{v} - \mathbf{\Upsilon}^\top \mathbf{D} \mathbf{\Upsilon} \hat{v} - \mathbf{\Upsilon}^\top \mathbf{K} \bar{q} - \mathbf{\Upsilon}^\top \bar{f}^{\mathrm{non}}) \tag{2.52}$$

which can be integrated using an integrator scheme such as Runge-Kutta-4 or ODE45 to obtain the values for $\hat{v}$ over time. More information on the accuracy of different integrators is given in Section 4.5.

3

Simulink model

In this chapter, the implementation of the equations of motion that are presented in Chapter 2 is given. The entire model is built using Matlab Simulink blocks. The blocks are placed in separate libraries to allow for easy version control of the model. In Section 3.1, the main blocks and their links are explained. Section 3.2 shows the different environment model options.

3.1. Equations of motion implementation

The Simulink model consists of a variety of library blocks, with up to 7 layers per block. A total of 6910 blocks are used in this model. A flow diagram is created that shows the interaction between different model elements. This also shows the flow of the different signals in the model. This block diagram is nearly equivalent to Simulink, since Simulink code also consists of blocks with signal lines that indicate the flow of parameters.

The model is built to resemble a standard Controller-Plant layout and can be seen in Figure 3.1. The controller choice is arbitrary to the lay-out of the model if a linear control algorithm is considered. For this model, a PID controller is used. The control signal can consist of the mass flow rate (throttle) and engine deflection angle (Thrust Vector Control / Reaction Control System).

The environment is taken out of the plant model such that it can be modelled as a disturbance to the input in the controller design. The environment itself is discussed further in Section 3.2. The launch vehicle model performs three basic actions

- Determine the instantaneous mass parameters

- Determine the sum of forces and moments

- Use this information to integrate the state parameters
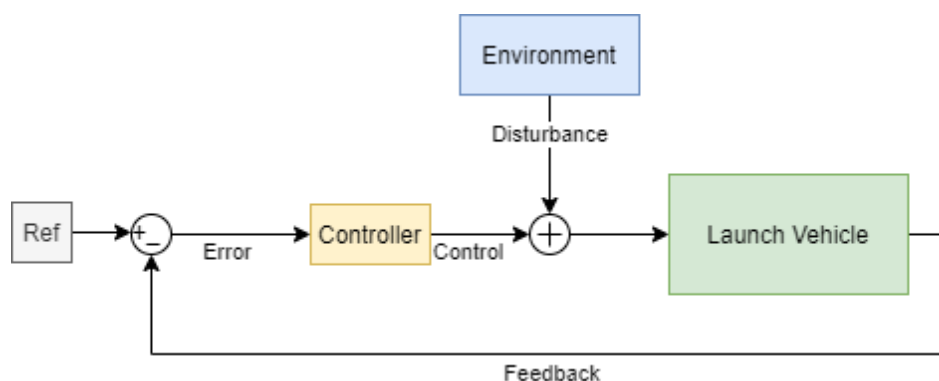
Figure 3.1: Top-level overview of the Simulink model
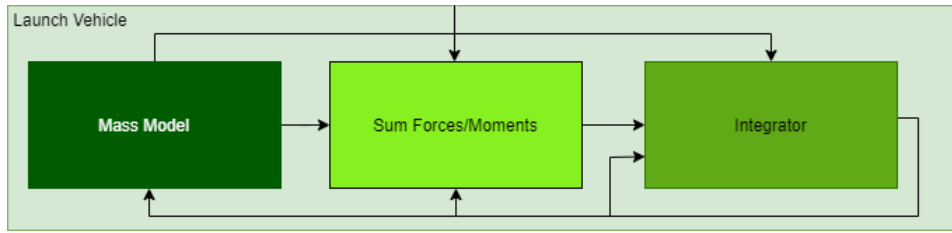
Figure 3.2: Launch vehicle model
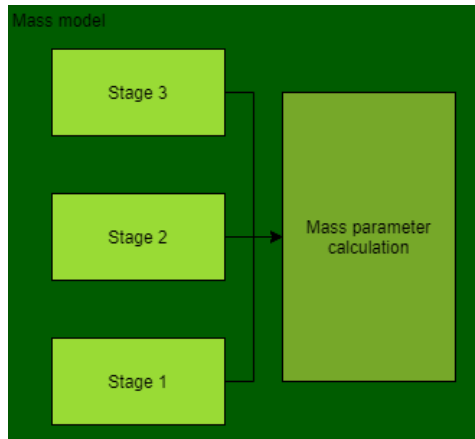
Figure 3.3: Schematic overview of the multi-stage mass model

The graphical overview of the flow between these items is given in Figure 3.2. The state parameters integration is a loop which takes the previous state, mass parameters and the resultant forces and moments to determine the next state. The mass model requires the current state to determine the inertia and center of gravity of the launch vehicle. Summing the forces and moments requires information from both the state, environment and mass model.

The mass model can be seen in more detail in Figure 3.3. The mass model consists of three stages, equivalent in set-up. If the user requires less than 3 stages, all other stages are set to have zero mass and inertia such that they do not contribute to the vehicle. The aerodynamic properties of different stages are handled in the environment block. The mass parameters are calculated with respect to the top of each stage. The origin of the system is the nose tip of the vehicle. The mass parameter calculation block calculates the center of gravity, inertia and mass of the multi-body with respect to this origin. This includes all the parameters for the slosh masses.

It is possible for a user to specify a hybrid propellant stage. When this happens, a separate model is used to calculate the inertia of the propellant, and all slosh parameters are set to zero.

The integrator block is the main difference from a rigid body model, as it includes calculations for the slosh parameters. An overview can be found in Figure 3.4. Parameters ν and q are the two state vectors that are also described in Chapter 2. Each of these state vectors is determined based on the current state. Using the current state vectors, the derivatives are calculated. A constraint matrix is used to combine the motions as discussed in Section 2.4.3. Since the constraint matrix depends on the state, it needs to be calculated at each time step as well. All this information is used to calculate the A matrix and b vector, from which the state derivative vector can be calculated using

$$\mathbf{A}\bar{x} = \bar{b} \rightarrow \bar{x} = \mathbf{A}^{-1}\bar{b} \tag{3.1}$$

This result is integrated. By default, Runge-Kutta-4 with a time-step of 1E-2 seconds is chosen. More details on the integrator can be found in Section 4.5. An example of the implementation in Simulink is given in Figure 3.5. The black dots on the left are separate strands of a bus signal and represent an input. A complete overview of the launch vehicle model can be found in Figure 3.6. Each signal line in the block diagrams can contain multiple individual values.
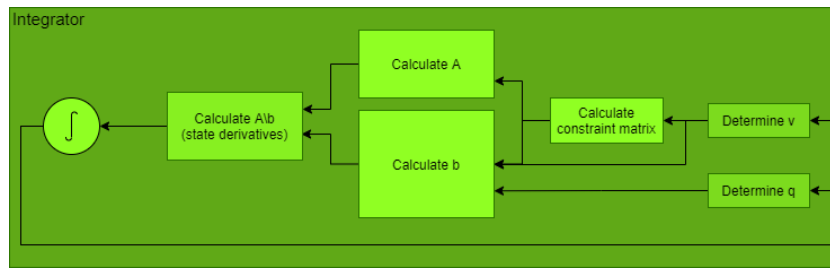
Figure 3.4: Schematic overview of the integrator block

In this case, the rigid body orientation, mode performance, node performances and distance from each node to the body C.G. are required. For the slosh section of the constraints, the orientation of each slosh mass as well as the slosh rods are required. The computation that is presented here is equivalent to Equation (2.47) when 6 slosh masses are considered.

3.2. Environment model

The environmental parameters such as pressure, wind speed and gravity change rapidly throughout the flight of a launch vehicle. A schematic overview of the environment model is given in Figure 3.7. Simulink blocks from the Aerospace Toolbox are used, unless specified otherwise.

In the wind block, 4 different options can be selected.

- Horizontal Wind Model

- Wind profile

- Discrete wind gust (custom)

- No wind (Default, custom)

The atmosphere selector is included in the aerodynamics block. The different options for the atmosphere model are

- Exponential atmosphere (custom)

- NLRMSISE-00

- COESA / US76-Standard (Default)

The models are selected using embedded subsystems and a multiport switch. In the initialisation file, the model settings are defined. A similar set-up is used for the gravity models. The available gravity models are

- Central gravity (custom)

- WGS84 gravity

- EGM2008 Spherical Harmonics [21] degree and order N (Default, N=4)

Aerodynamic coefficients are required to determine the aerodynamic forces and moments acting on the vehicle. The user has two options to supply the aerodynamic coefficients, depending on the available data. If wind tunnel data is used, this generally consists of 3D data with 2 orthogonal parameters such as C_L and C_D and one pitching parameter such as C_m. The model expands this 3D data to the 6DOF model by assuming that the vehicle is axi-symmetric. If available, it is also possible to use 6DOF aerodynamic coefficients. These can be obtained using empirical programs such as DATCOM. For both models, lookup tables are used to determine the current coefficient value. The lookup parameters are angle of attack and Mach number (3DOF) and can include angle of sideslip (6DOF). If required, altitude can also be added as a lookup parameter. The simulink implementation of the aerodynamic forces and moments is shown in Figure 3.8. For more details on the different environmental options, the reader is referred to [10].

Constraint Matrix for N slosh masses looks as follows

$$X_1 = \begin{pmatrix} 1 & 0 & 0 \\ 0 & 1 & 0 \\ 0 & 0 & 1 \end{pmatrix} \rightarrow size = 8 \times 8$$

$$X_2 = \begin{pmatrix} 1 & A & B \\ 0 & 0 & 0 \\ \vdots & 1 & A & B \\ 0 & 0 & 0 \\ \vdots \end{pmatrix} \rightarrow size = 6N \times 8$$

$$X_3 = 0 \rightarrow size = 8 \times 3N$$

$$X_4 = \begin{pmatrix} C & 0 & 0 \\ 1 & 0 & 0 \\ 0 & C & 0 \\ 0 & 1 & 0 \\ \vdots \end{pmatrix} \rightarrow size = 6N \times 3N$$

$$Y = \begin{pmatrix} X_1 & X_3 \\ X_2 & X_4 \end{pmatrix} \rightarrow size = 8 + 6N \times 8 + 3N$$
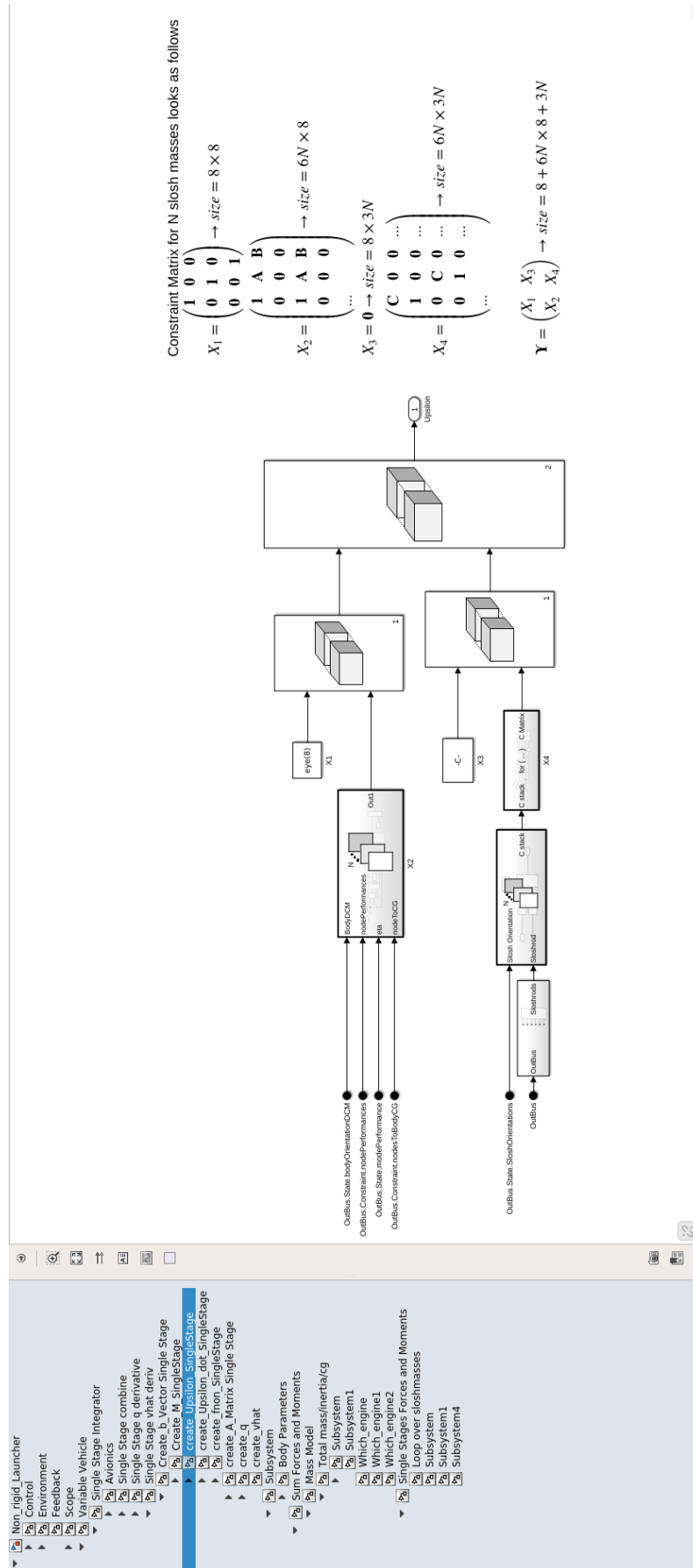
Figure 3.5: Constraint matrix calculation in Simulink. The left hand side is the model tree, and shows the current level in the model
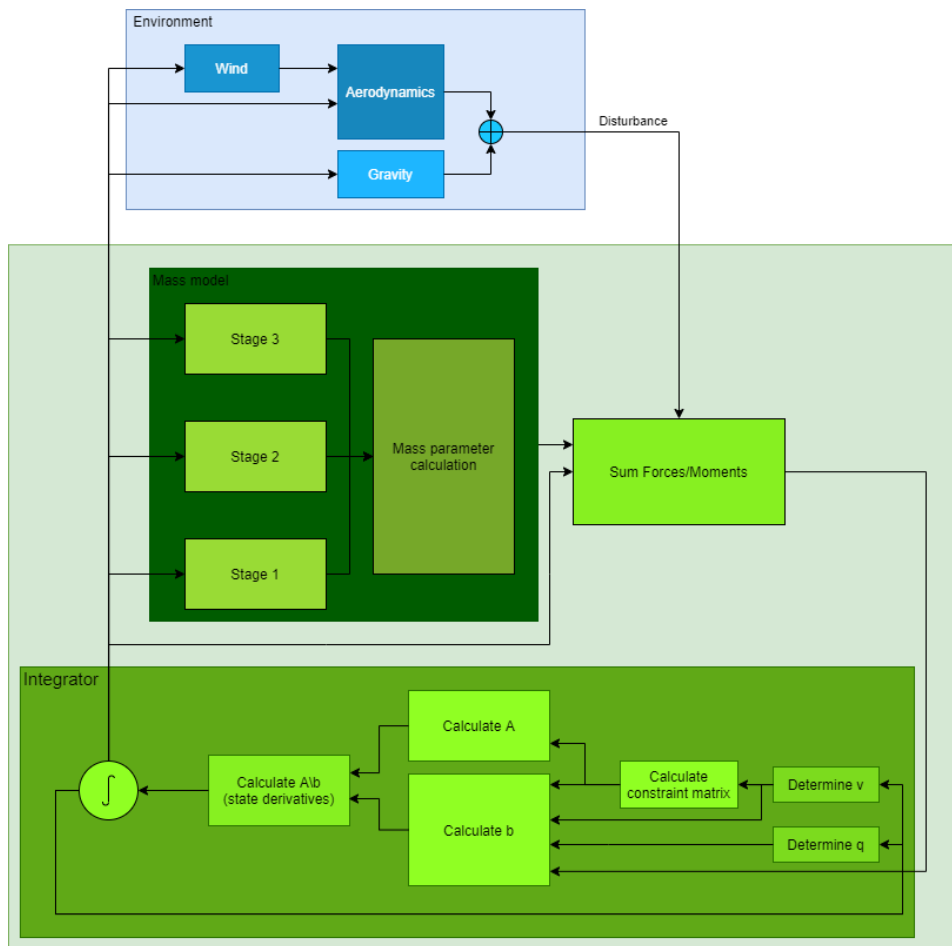
Figure 3.6: Complete overview of Figure 3.1
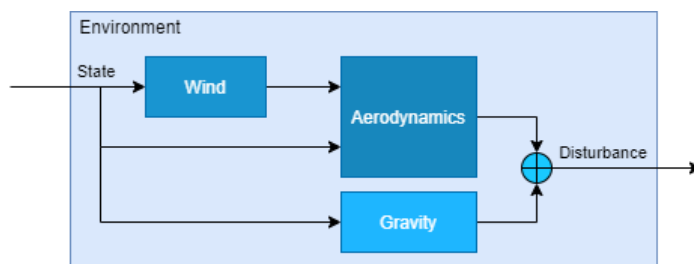
Figure 3.7: Schematic overview of the environment model
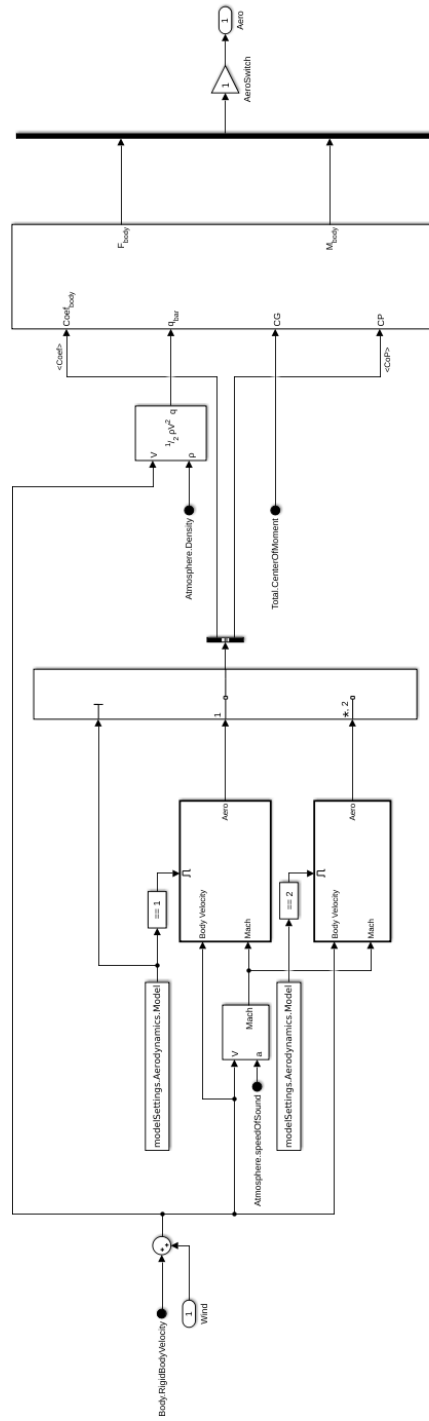
Figure 3.8: Simulink implementation of the aerodynamic forces and moments calculations
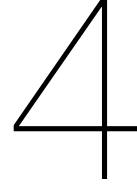
Model verification

The equations of motion that are established in Chapter 2 are implemented in a Matlab Simulink environment. The implementation is shown in Chapter 3. This implementation needs to be verified to ensure correct operation of the code. This is achieved by comparing the propagated results to analytical results for simplified scenarios. It is expected that the equations of motion conserve energy. An energy check is used to further verify the system.

The motion of the vehicle is described by three independent motions. Although these motions can be verified independently, it is chosen to adapt the final code to only show the effect of the motion of interest. This means that when, for example, the rigid body motion is verified, the slosh mass and flexibility is set to zero. This is chosen to ensure that the final implementation of a given motion is correct. The modifications to the final code are given in each section.

For the verification, the Runge-Kutta-4 integrator is selected with a fixed time-step of 1E-2 seconds unless specified otherwise. This fixed-step solver is chosen to allow for easy debugging and because of its good accuracy for a given computational time. It also proved to be more stable than a variable-step integrator such as ODE45. This integrator choice is verified at the end of this chapter.

First, the custom variable mass model is verified in Section 4.1. Next, in Section 4.2 the rigid body motion is verified for both a simple, straight trajectory as well as a more complex Multi Degree of Freedom trajectory. In Section 4.3 the slosh mass motion is verified. The combined equations of motion are verified by performing an energy check on the complete system in Section 4.4. Using the results from the verification, an integrator trade-off is performed in Section 4.5.

4.1. Custom mass model verification

In this section, the variable mass model for a two-stage rocket is considered. The tanks are assumed to be cylindrical and the structures are assumed to have a constant mass.

4.1.1. Liquid tank mass depletion model

The depletion of mass has a major impact on the mass parameters of the launch vehicle. The liquid propellant tanks are initialised by setting the density, tank fill ratio, tank diameter and tank height. The Oxidiser-to-Fuel (O/F) ratio and total mass flow are required to determine the mass depletion for both tanks over time. The mass flow rate is negative and integrated to calculate the instantaneous propellant mass. The mass flow can be directly coupled to the thrust of the vehicle using the well-known thrust equation

$$T = |\dot{m}|I_{sp}g_0 + A_e(p_e - p_0) \tag{4.1}$$

If one of the tanks is empty, the total mass flow rate is set to zero.

For the verification of the model, a simplified two stage liquid propellant launch vehicle is considered. Two cylindrical tanks are stacked on top of each other. For this simulation, two arbitrary liquids with a density of 800 kg/m^3 (fuel) and 1400 kg/m^3 (oxidiser) are used. The denser propellant is tank placed on top of the lighter tank. The structure and engine are added separately and are given a constant mass and centre of gravity location with respect to the top of the structure. The inertia of the structures is calculated with respect to the centre of gravity of the structure and is assumed to be constant.
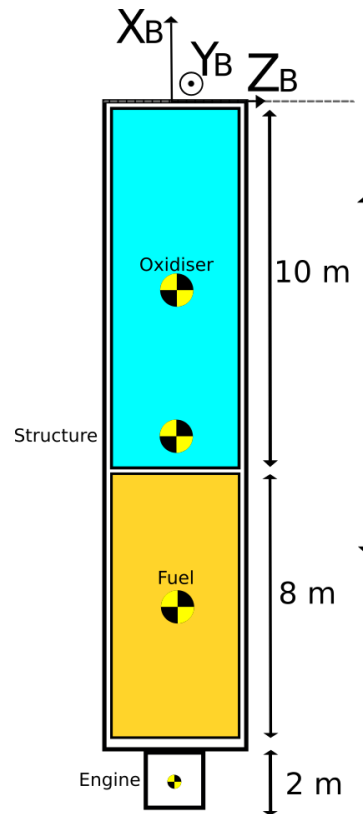
Figure 4.1: Graphical representation of the simplified massmodel at initial conditions

The table with all initialisation data can be found in Table 4.1 and Table 4.2. A figure representing this model can be seen in Figure 4.1.

4.1.2. Centre of Gravity location

The total mass of the vehicle decreases linearly for a constant mass flow. The final mass is higher than or equal to the dry mass of the stage since not all propellant might be used. In Figure 4.2, the centre of gravity of both tanks can be seen.

With the given initialisation data, it can be calculated that at $t = 0$, the centre of gravity should lie at

$$C.G_{ox} = \frac{h_{tank}}{2} - \frac{\dot{m}_{ox}t}{2\pi R^2 \rho_{ox}} = -5m$$

where the fill ratio is given by F, the height of the propellant tank is given by h, the inner radius of the propellant tanks is given by r and the density of the propellant is given by ρ. For the bottom tank, here represented by the lighter fuel tank, the centre of gravity with respect to the reference point is given by

$$C.G_{fuel} = h_{ox} + \frac{h_{fuel}}{2} - \frac{\dot{m}_{fuel}t}{2\pi R^2 \rho_{fuel}} = -10 - 4 = -14m$$

With an oxidiser-to-fuel ratio of 2, it can be calculated that the fuel tank will run out before the oxidiser tank.

Table 4.1: Initialisation data for the custom mass model - Propellant tanks

Propellant parameters		
Tank inner radius	2.00	[m]
O/F ratio	2.00	[-]
Distance top to Ox. Tank	0.00	[m]
Bessel parameter	1.84119	[-]
Oxidiser tank		
Height of tank	10.00	[m]
Tank fill ratio	1	[-]
Propellant density	1400	[kg/m^3]
Slipping factor	0.95	[-]
Fuel tank		
Height of tank	8.00	[m]
Tank fill ratio	1	[-]
Propellant density	800	[kg/m^3]
Slipping factor	0.95	[-]

Table 4.2: Initialisation data of custom mass model - Structure and engine

Structural parameters		
Total structure mass	1000	[kg]
Total structure inertia	[100,0,0; 0,10000,0; 0,0,10000]	[kgm^2]
Total structure centre of gravity	[-9; 0; 0]	[m]
Engine parameters		
Engine location	[-18; 0; 0]	[m]
Engine mass	100	[kg]
Engine inertia	0.01*Total structure inertia	[kgm^2]
Engine centre of gravity wrt engine top	[-1,0,0]	[m]

The time required to empty both tanks is given by

$$t_{empty_{ox}} = \frac{\pi r^2 \rho_{ox} h_{ox} F_{ox}}{\dot{m} * OF/(OF+1)} = 263.89s$$

$$t_{empty_{fuel}} = \frac{\pi r^2 \rho_{fuel} h_{fuel} F_{fuel}}{\dot{m}/(OF+1)} = 241.27s$$

This means that both tanks should stop expelling mass once the fuel tank is empty, meaning that the linearly decreasing line should flatten at $t = 241.27$ s, which is shown in Figure 4.2.

The slosh rod length is of important influence for the centre of gravity of the slosh mass. It is calculated based on Roberts [22]. The length of this rod is limited to the fluid height of the tank. In other words, if the calculated slosh rod length exceeds the fluid level, the rod length is set equal to the fluid level. This method gives a more accurate representation of a depleting tank since the analytical result converges to a slosh rod with an infinite length for low fluid levels. The slosh rod length is used to calculate the natural frequency of the motion of the slosh mass and the mass parameters such as inertia for the vehicle.
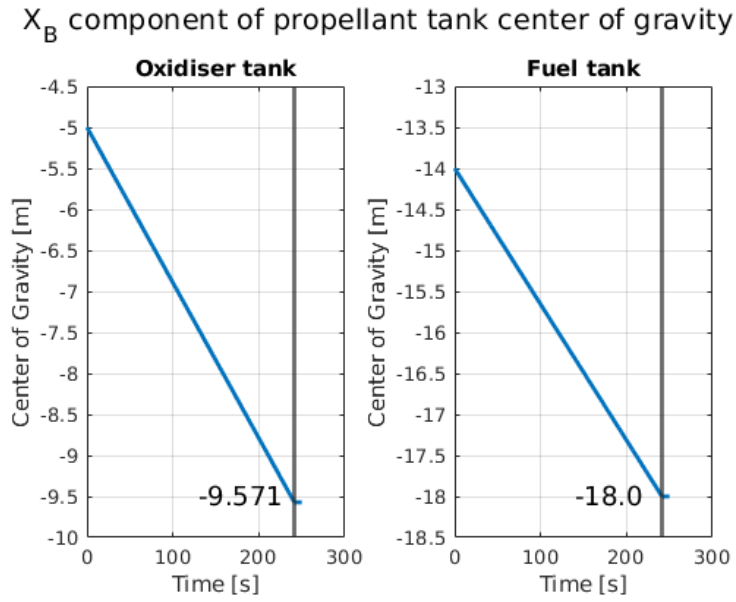
Figure 4.2: X_B component of the centre of gravity of both propellant tanks. Vertical line corresponds with $t = 241.27$ s

The centre of gravity of both propellants at $t = 241.27s$ is

$$C.G_{ox} = \frac{h_{tank}}{2} - \frac{\dot{m}_{ox} * 241.27}{2\pi R^2 \rho_{ox}} = -9.571m$$

$$C.G_{fuel} = h_{ox} + \frac{h_{fuel}}{2} - \frac{\dot{m}_{fuel} * 241.27}{2\pi R^2 \rho_{fuel}} = -18m$$

The centre of gravity of the complete vehicle can simply be calculated by using the additive property of mass. The centre of gravity of the complete vehicle is

$$C.G = \frac{\sum m_i d_i}{\sum m_i} \tag{4.2}$$

where m_i represents the ith mass with a centre of gravity with respect to the top of the structure d_i. The total center of mass for the full tanks becomes

$$C.G = \frac{C.G_{ox}m_{ox} + C.G_{slosh1}m_{slosh1} + C.G_{fuel}m_{fuel} + C.G_{slosh2}m_{slosh2} + \cdots}{m_{ox} + m_{slosh1} + m_{fuel} + m_{slosh2} + \cdots}$$

$$= \frac{-5 * 159937.11 - 2.17 * 15992.08 - 14 * 71286.45 - 12.2 * 9138.32 - \cdots}{159937.11 + 71286.45 + 15992.08 + 9138.32 + \cdots} = -7.593m$$

Similarly, at $t = 241.27$ s, the centre of gravity can be calculated to be C.G.

$$C.G = \frac{-9.571 * 4558.403 - 9.96 * 10520.785 - 9 * 1000 - 19 * 100}{4560.154 + 10522.367 + 1000 + 100} = -9.8469m$$

The comparison between the analytical and propagated results for the center of gravity can be found in Table 4.3

Table 4.3: Verification results for custom mass model

Parameter	Analytical result	Propagated result	Difference [%]
Centre of gravity [m] (X_B)			
$C.G_{ox}$ @ $t = 0$	-5	-5.00	0.000
$C.G_{ox}$ @ $t = 241.27$	-9.571	-9.57144	0.005
$C.G_{fuel}$ @ $t = 0$	-14	-14.00	0.000
$C.G_{fuel}$ @ $t = 241.27$	-18	-18.00	0.000
$C.G_{tot}$ @ $t = 0$	-7.593	-7.5918	-0.016
$C.G_{tot}$ @ $t = 241.27$	-9.8469	-9.85	-0.011

4.1.3. Variable inertia

The inertia of the structure, engine and propellant are calculated with respect to their respective centre of mass. For the propellant tanks, the inertia of the fluids is estimated by assuming that the propellant is a solid cylinder with a density equivalent to the density of the propellant. As a result, the inertia at any given time can simply be calculated using the standard equation for inertia of solid cylinders

$$I_{xx} = \frac{1}{2}mr^2 * (1 - K_{slip}) \tag{4.3}$$

$$I_{yy} = I_{zz} = \frac{1}{12}m(3r^2 + h^2) \tag{4.4}$$

where r represents the radius of the cylinder with mass m. Parameter h represents the height of the cylinder, here considered to be the fluid height. The propellant influences the inertia of the vehicle around the X_B axis only when there is friction between the walls and the propellant. This friction is represented by the slipping factor K_{slip} and chosen to be approximately 0.95, meaning only 5% of the inertia around X_B contributes to body inertia due to limited slipping. In reality, this value is highly dependent on the propellants that are used, as well as wall roughness of the tank. The slipping factor is a variable in the model, but is given a fixed value. If a viscosity model is available for the chosen propellant, minor model changes are required to make this value variable. It is assumed that a fixed value for the slipping coefficient is sufficient for this analysis. Rewritten to parameters that describe the propellant flow, the following result is obtained

$$I_{xx} = \frac{1}{2}(h_{tank}\pi r_{tank}^2 F\rho_{fluid} + \int_0^t \dot{m}_{fluid})r_{tank}^2 \tag{4.5}$$

$$I_{yy} = \frac{1}{12}(h_{tank}\pi r_{tank}^2 F\rho_{fluid} + \int_0^t \dot{m}_{fluid})(3r_{tank}^2 + (h_{tank} * F + \frac{\int_0^t \dot{m}_{fluid}}{\pi r_{tank}^2 \rho})^2) \tag{4.6}$$

$$I_{zz} = I_{yy} \tag{4.7}$$

In this model, the slosh mass is calculated based on the total remaining mass. The calculated slosh mass is subtracted from the total mass. Since the inertia is linearly dependent on mass, the inertia of the slosh mass and fixed propellant mass are calculated based on the fraction between the two masses. Therefore, the inertia of the propellant is calculated according to

$$I_{fixed} = f(m_{fixed}) \quad ; \quad m_{fixed} = m_{tot} - m_{slosh} \tag{4.8}$$

$$I_{slosh} = f(m_{frac}) \quad ; \quad m_{frac} = \frac{m_{slosh}}{m_{fixed}} \tag{4.9}$$

The moment of inertia of the structure and engine are considered constant. The inertia of each element is calculated with respect to its own center of mass.

Table 4.4: Verification results for custom mass model

Inertia	Analytical result	Propagated result	Difference [%]
Ixx_{ox} @ $t = 0$	15993.71	15992.711	-0.006
Ixx_{ox} @ $t = 241.27$	456.0154	456.015	0.000
Ixx_{fuel} @ $t = 0$	7128.644	7128.644	0.000
Ixx_{fuel} @ $t = 241.27$	0	0	0.000
Ixx_{tot} @ $t = 0$	25591.03	25590.1	-0.004
Ixx_{tot} @ $t = 241.27$	874.88127	874.851	-0.003
Iyy_{ox} @ $t = 0$	1492149.268	1492149.268	0.000
Iyy_{ox} @ $t = 241.27$	4837.518	4837.517	0.000
Iyy_{fuel} @ $t = 0$	451300.25	451300.25	0.000
Iyy_{fuel} @ $t = 241.27$	0	0	0.000
Iyy_{tot} @ $t = 0$	6825044.22	6825044	0.000
Iyy_{tot} @ $t = 241.27$	27880.50	27881.2	0.003

The center of mass of each item is calculated with respect to a common reference. In this model, the top of the vehicle is used. As a result, the inertia of the entire model can be calculated by using the additive properties of inertia. The well-known parallel axis theorem is used to calculate the total body inertia. The theory is rewritten to allow for better model implementation according to

$$\mathbf{I} = \mathbf{I}_c + m(|\bar{r}|\delta_{ij} - \bar{r}^T\bar{r}) \tag{4.10}$$

Parameter $\bar{r}$ indicates the difference between the multi-body centre of gravity and the mass of interest. δ_{ij} represents the Kronecker delta, which is expressed as an identity matrix. $\mathbf{I}_c$ represents the inertia of the body around its centre of gravity. For example, the inertia of the slosh mass is calculated using

$$\mathbf{I}_S = \mathbf{I}_{S_c} + m(|\bar{r}^{zs}|^2\delta_{ij} - (\bar{r}^{zs})^T\bar{r}^{zs}) \tag{4.11}$$

Using the equations above with the data from Table 4.1 and Table 4.2, the analytical results for the inertia can be calculated. The comparison between the analytical and propagated results can be seen in Table 4.4. Since the mass model calculations are exclusively based on analytical equations, it is expected that the only error that exists between the analytical and propagated solution are rounding errors. This can be seen in the table. Therefore, the custom mass model implementation can be considered verified.

4.2. Rigid body motion verification

The rigid body motion is the main component of the equations of motion and determines the inertial position of the vehicle over time. For a simplified simulator, this is the only motion that is considered. The motion is verified by comparing the simulated results to an analytical solution. In order to mitigate the effects of flexibility and slosh mass, the following modifications are performed.

- The slosh mass is set to a value of ≈ 0 kg[1]

- The rigid body moment due to slosh masses is forced to zero.

- The motion of the slosh masses is not integrated.

- The mode performances of the different nodes of the vehicle are set to zero.

- The mode performance is not integrated.

---

[1]Setting the slosh mass to zero would result in a zero division when solving for $\hat{v}$.
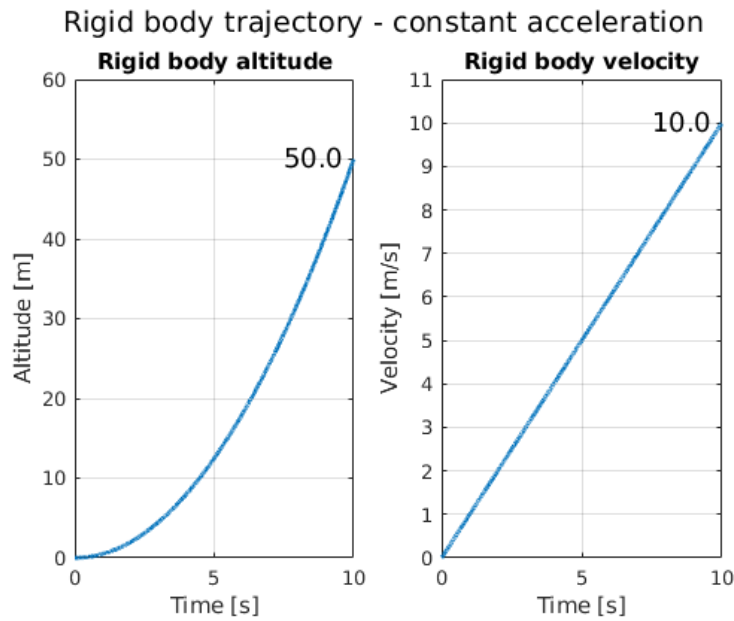
Figure 4.3: Simulated rigid body motion for constant acceleration

4.2.1. Straight trajectory in vacuum

The propellant tanks are initialised with 10,000 kg of propellant. The engine mass is set to 100 kg and the dry mass of the vehicle is set to 1000 kg. This results in a total rigid body mass of 21,100 kg. The mass flow rate is set to zero, and a constant acceleration of 1 m/s^2 is applied to the $+X_b$ axis of the rigid body for a time of 10 seconds. Analytically, this would result in an altitude of

$$h = h_0 + v_0 t \frac{1}{2} a t^2 = 0 + 0 + \frac{1}{2} * 1 * 10^2 = 50 \text{ m}$$

with a velocity of

$$v = at = 1 * 10 = 10 \text{ m/s}$$

The simulated motion can be seen in Figure 4.3. The data labels of the final value are indicated in the figure.

Next, the simulation is extended to change the acceleration over time. The acceleration profile is now simulated as follows

- Accelerate in the $+X_b$ direction with 1 m/s^2 for 5 seconds

- No acceleration for 5 seconds

- Accelerate in the $-X_b$ direction with 1 m/s^2 for 5 seconds

Analytically, this would result in a velocity of

$$v_1 = v_0 + at = 0 + 1 * 5 = 5 \text{ m/s} \quad \text{at time} \quad t = 5$$
$$v_2 = v_1 + at = 5 + 0 * 5 = 5 \text{ m/s} \quad \text{at time} \quad t = 10$$
$$v_3 = v_2 + at = t + -1 * 5 = 0 \text{ m/s} \quad \text{at time} \quad t = 15$$

Rigid body trajectory - constant acceleration
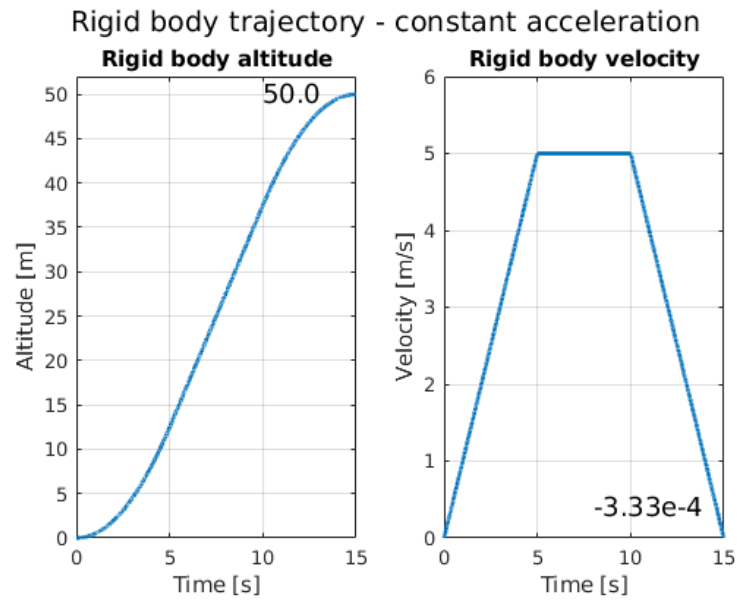
Figure 4.4: Simulated rigid body motion for varying acceleration

The corresponding altitude can be calculated to be

$$h_1 = h_0 + v_0 t + \frac{1}{2}at^2 = 0 + 0 + \frac{1}{2} * 1 * 10^2 = 12.5 \text{ m}$$

$$h_2 = h_1 + v_1 t + \frac{1}{2}at^2 = 12.5 + 5 * 5 + 0 = 37.5 \text{ m}$$

$$h_3 = h_2 + v_2 t + \frac{1}{2}at^2 = 37.5 + 5 * 5 + -\frac{1}{2} * 1 * 5^2 = 50.0 \text{ m}$$

The simulated results can be seen in Figure 4.4. Due to the instantaneous change in acceleration, the result differs a negligible amount (25 mm) from the analytical solution. This difference can be further reduced by changing the integrator settings at the cost of the required CPU time. This trade-off is further discussed in Section 4.5.

4.2.2. Complex trajectory in vacuum

The propellant tanks still both contain 10,000 kg of propellant. The inertia of these tanks are calculated according to Section 4.1.3. The structure and engine are given an arbitrary fixed inertia of

$$I_{engine} = 0.01 * I_{rigid} = 0.01 * \begin{bmatrix} 100 & 0 & 0 \\ 0 & 10000 & 0 \\ 0 & 0 & 10000 \end{bmatrix} \text{kgm}^2$$

This results in a total inertia of

$$I_{tot} = \begin{bmatrix} 2101 & 0 & 0 \\ 0 & 446509.3249 & 0 \\ 0 & 0 & 446509.3249 \end{bmatrix} \text{kgm}^2$$

which remains fixed for the entire simulation.

A pure torque is applied to the rigid body according to

$$M_{yy} = 0 Nm \quad \text{for} \quad 0 \leq t < 5s$$
$$M_{yy} = 10,000 Nm \quad \text{for} \quad 5 \leq t < 6s$$
$$M_{yy} = -10,000 Nm \quad \text{for} \quad 6 \leq t < 7s$$
$$M_{yy} = 0 Nm \quad \text{for} \quad 7 \leq t < 21s$$

This applied torque results in an angular displacement of the rigid body. For this simplified scenario, this displacement can be calculated analytically. For the given rigid body inertia and applied torque, the angular acceleration becomes

$$\alpha_1 = \alpha_4 = 0 \text{ rad/s}^2$$

$$\alpha_2 = -\alpha_3 = \frac{M_{yy}}{I_{yy}} = \frac{10,000}{446509.3249} = 0.0223959 \text{ rad/s}^2$$

At time $t = 5s$, this results in an angular velocity and displacement of

$$\omega_1 = \cancel{\omega_0}^{0} + \alpha_1 * t = 0 \quad \text{rad/s}$$

$$\theta_1 = \cancel{\theta_0}^{0} + \frac{1}{2}\cancel{\alpha_1}^{0} t^2 = 0 \quad \text{rad}$$

At time $t = 6$ s, the torque is applied, resulting in an angular velocity and displacement of

$$\omega_2 = \cancel{\omega_1}^{0} + \alpha_2 * t = 0.0223959 \quad \text{rad/s}$$

$$\theta_2 = \cancel{\theta_1}^{0} + \cancel{\omega_1}^{0} * t + \frac{1}{2}\alpha_2 t^2 = 0.01119795 \quad \text{rad}$$

At time $t = 7$, the torque is applied in the opposite direction, resulting in

$$\omega_3 = \omega_2 + \alpha_3 * t = 0 \quad \text{rad/s}$$

$$\theta_3 = \theta_2 + \omega_2 * t + \frac{1}{2}\alpha_3 t^2 = 0.0223959 \quad \text{rad}$$

Finally, it can be confirmed that the vehicle maintains this orientation since no torque is applied any more. Therefore, the final angular velocity and displacement at $t = 21$ s becomes

$$\omega_4 = \cancel{\omega_3}^{0} + \cancel{\alpha_4}^{0} * t = 0 \text{ rad/s}$$

$$\theta_4 = \cancel{\theta_3}^{0} + \cancel{\omega_3}^{0} * t + \frac{1}{2}\cancel{\alpha_4}^{0} t^2 = 0.0223959 \quad \text{rad}$$

The results can be compared by plotting the angular velocity and displacement of the rigid body with respect to time. This plot can be seen in Figure 4.5. As can be seen, the simulated accuracy is within 25 mm from the analytical result. It can therefore be stated that the rigid body motion is correctly implemented in the equations of motion.

4.3. Slosh mass motion verification

The flexibility of the vehicle is described based on the modal deformation at given points in the vehicle. These points are chosen to coincide with the attachment point of the slosh pendulum. As a result, a flexible motion of the vehicle will influence the motion of the slosh mass. Furthermore, an acceleration of the vehicle, angular or inertial, will result in a displacement of the slosh mass from the neutral position. To verify the motion of the slosh masses, these effects have to be mitigated in the final code.
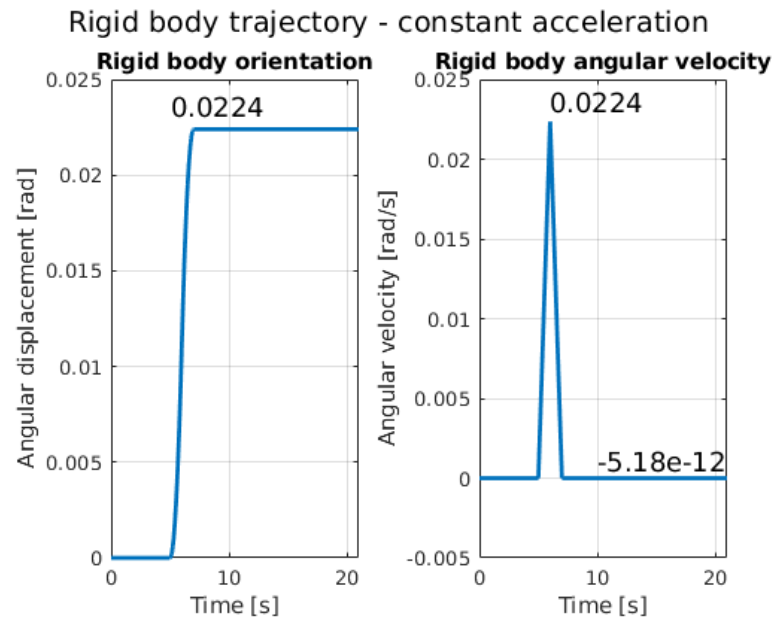
Figure 4.5: Simulated rigid body motion with constant acceleration and varying torque

To achieve this, the following changes are made to the model:

- Flexibility motion is not integrated.

- Nodal flexibility is set to zero.

- Motion of slosh mass 2 is not integrated.

- Slosh mass 2 is set to ≈ 0 kg.

The motion of the slosh mass in inertial space is predominantly determined by the motion of the rigid body through the constraints described in Section 2.4.2. This constraint is first checked by comparing the inertial location of the slosh mass with respect to that of the rigid body. The trajectory from Section 4.2.1 is considered here.

The slosh mass is given an initial offset of 5 degrees. The rod length is set to a fixed value of 2 m. The inertial location of the slosh mass and the rigid body are given in Figure 4.6. The Y and Z component of this location are shown separately in Figure 4.7.

The initial offset can easily be calculated as

$$Y_i^S = \sin 5° * 2 = 0.174311 m \qquad (4.12)$$

which can also be seen in Figure 4.7. The motion of the sloshmass is undamped. As can be seen, the trajectory is identical to the rigid body, with a small bias. This bias is the distance from the rigid body centre of gravity to the slosh mass. With a slosh rod length of 2 meters, this results in a distance in the X_b axis of

$$x_B = \cos 5° * 2 = 1.9929 m \qquad (4.13)$$

when the slosh mass is at its maximum offset of $5°$.

The period of the motion can't be easily calculated analytically, since the motion of the rigid body is forcing a movement on the slosh mass and vice versa. Therefore, the inertia of the rigid body is now set to a value of 1E20 times its original value. This ensures that the motion of the slosh mass doesn't affect the rigid body attitude. Furthermore, the forces and moments acting on the rigid body are forced to zero, fixing the vehicle in inertial space. The same slosh mass is set to an offset of 5 degrees. The inertia of the slosh mass is set to zero.
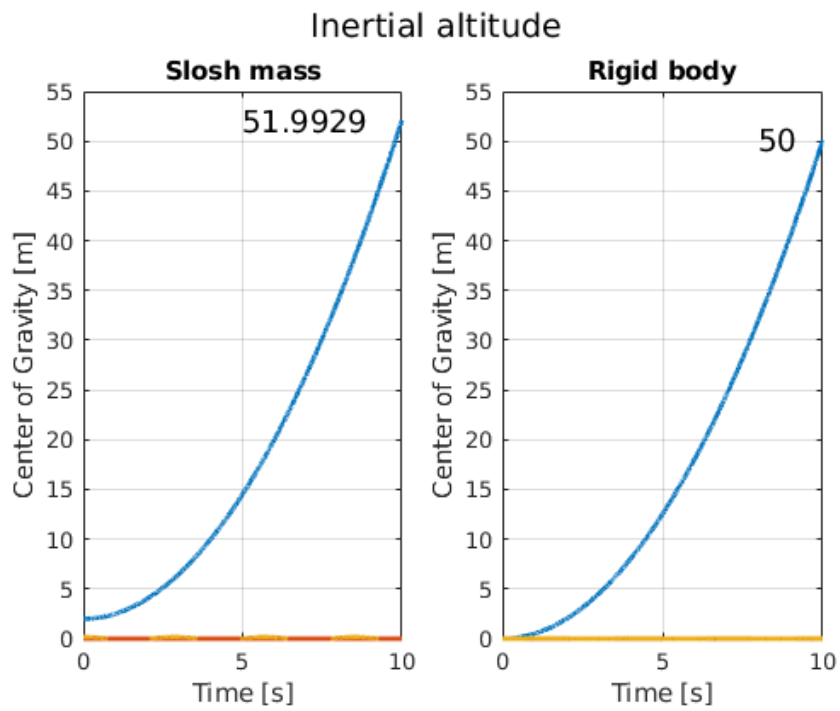
Figure 4.6: Inertial location of the rigid body and slosh mass 1. Blue indicates X_I location. Yellow and red indicate Y_I and Z_I respectively.

Figure 4.7: Inertial Y_S and Z_S components
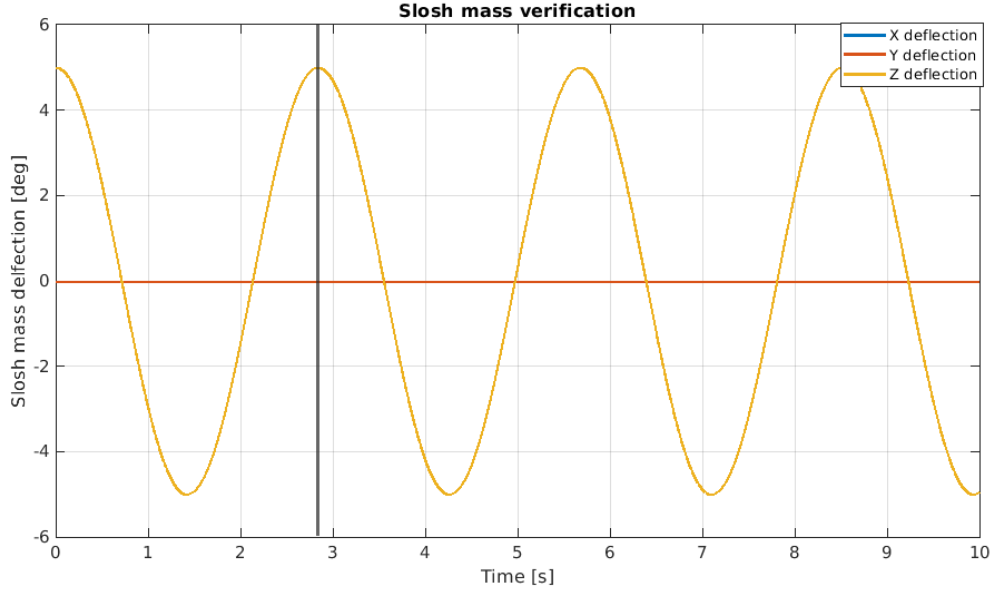
Figure 4.8: Verification of slosh mass motion. Vertical line indicates t = 2.8375 s

With these assumptions, the slosh mass is equivalent to a normal pendulum, for which the period can simply be calculated using

$$T = 2\pi \sqrt{\frac{L}{g}} = 2\pi \sqrt{\frac{2}{9.80665}} = 2.8375s \qquad (4.14)$$

In figure Figure 4.8, the motion of the slosh mass can be seen. The period is similar to the analytical period. Therefore, the motion of the slosh mass, as well as its constraint, are verified.

4.4. Energy Check

All motions can be verified individually by making adjustments to certain parts of the code. However, the interaction between the motions is too complex to calculate analytically. Therefore, the accuracy of the full system is checked by calculating the total energy in the system. Combined with the results of the individual movement verification, a constant system energy gives a solid indication of correct implementation of the equations of motion.

To check if the total energy of the system is constant, no external forces except gravity are applied to the system. All the motions are given an arbitrary nonquiescent initial condition. The initial conditions for the energy check for a body with two slosh masses is given in Table 4.5. For this system, the total kinetic energy is calculated according to

$$E_{kin} = \frac{1}{2}m_b(\bar{v}_b^{zw/i})^2 + \sum_1^N \frac{1}{2}m_{sN}(\bar{v}_{sN}^{c_Nw/i})^2 + \frac{1}{2}\mathbf{J_b}(\bar{\omega}_b^{bi})^2 + \sum_1^N \frac{1}{2}\mathbf{J}_{sN}(\bar{\omega}_{sN}^{s_Ni})^2 \qquad (4.15)$$

With the notation from Equation (2.40) for the equations of motion, several vehicle states are written as a single vector. This vector ν is given by

$$\bar{v} = [\bar{v}_i^{zw}, \bar{\omega}_b^{bi}, \dot{\bar{\eta}}, \bar{v}_i^{s_1w}, \bar{\omega}_s^{s_1i}, \bar{v}_i^{s_2w}, \bar{\omega}_s^{s_2i}]^T \qquad (4.16)$$

This means Equation (4.15) can be conveniently rewritten as a function of the state ν

$$E_{kin} = \frac{1}{2}(\mathbf{Y}\hat{v})^T \mathbf{M} \mathbf{Y} \hat{v} \qquad (4.17)$$

Table 4.5: Initial conditions of (state) parameters for energy check

Rigid body		
$\mathbf{C}_{bi}$	$\mathbf{1}$	Identity 3x3
$\bar{\omega}_b^{bi}$	$[0,0,0]^T$	
$\bar{r}_i^{zw}$	$[6379137,0,0]^T$	1000 meters altitude
$\bar{v}_i^{zw}$	$[500,0,0]^T$	
Slosh masses		
$\mathbf{C}_{s1,i}$	$\begin{pmatrix} 0.9962 & 0.0872 & 0 \\ -0.0872 & 0.9962 & 0 \\ 0 & 0 & 1 \end{pmatrix}$	+ 5 degrees around Z_{s1}
$\bar{\omega}_{s1}^{s1,i}$	$[0,0,0]^T$	
$\mathbf{C}_{s2,i}$	$\begin{pmatrix} 0.9962 & -0.0872 & 0 \\ 0.0872 & 0.9962 & 0 \\ 0 & 0 & 1 \end{pmatrix}$	- 5 degrees around Z_{s2}
$\bar{\omega}_{s2}^{s2,i}$	$[0,0,0]^T$	
Elasticity		
$\bar{\eta}$	$[0.2,0.5]^T$	
$\dot{\eta}$	$[0.1,-0.25]^T$	
$\bar{r}_b^{a1,z}$	$[3,0,0]^T$	
$\bar{r}_{s1}^{a1,c}$	$[1.09,0,0]^T$	
$\mathbf{\Psi}_b^{a1}$	$\begin{pmatrix} 0 & 0 \\ -0.32 & 0 \\ 0 & -0.32 \end{pmatrix}$	
$\bar{r}_b^{a2,z}$	$[-3,0,0]^T$	
$\bar{r}_{s2}^{a2,c}$	$[1.09,0,0]^T$	
$\mathbf{\Psi}_b^{a2}$	$\begin{pmatrix} 0 & 0 \\ 0.16 & 0 \\ 0 & 0.16 \end{pmatrix}$	
$\mathbf{Z}$	$\begin{pmatrix} 0 & 0 \\ 0 & 0 \end{pmatrix}$	Undamped for energy check
$\mathbf{\Omega}$	$\begin{pmatrix} 15*2\pi & 0 \\ 0 & 15*2\pi \end{pmatrix}$	

Next, the elastic potential energy is calculated. This potential is acquired similarly to the potential energy of a spring

$$E_{flex} = \frac{1}{2}Kx^2 \equiv \frac{1}{2}\bar{\eta}^T \Omega^2 \bar{\eta} \tag{4.18}$$

Finally, the gravitational potential energy is calculated. To avoid errors in the calculation, a simple constant gravitational acceleration of $[-9.81, 0, 0]^T$ is considered. The potential energy is then calculated as

$$E_{pot} = -m_b * \bar{g}^T r_i^{\bar{z}w} + \sum_1^N -m_{sN} \bar{g}^T r_i^{c_N w} \tag{4.19}$$

The slosh mass constraint made the inertial slosh velocity redundant as explained in Section 2.4.3. This means that the inertial slosh position needs to be calculated explicitly for the gravitational potential energy. The inertial slosh position is expressed in terms of the calculated state parameters following

$$r_i^{cw} = \underbrace{-\mathbf{C}_{si}^T * r_s^{pc}}_{1} + \underbrace{\mathbf{C}_{bi}^T * \Psi_b^a * \bar{\eta}}_{2} + \underbrace{\mathbf{C}_{bi}^T * r_b^{az}}_{3} + \underbrace{r_i^{zw}}_{4} \tag{4.20}$$

This equation describes the sum of the position of the slosh mass w.r.t. its attachment point (1), the attachment point w.r.t. its undeflected state (2), the undeflected attachment point w.r.t. the centre of gravity of the vehicle (3) and the location of the centre of gravity of the vehicle (4), all expressed in the inertial frame.

With these parameters, the total system energy can be calculated

$$E = E_{kin} + E_{pot} + E_{flex} \tag{4.21}$$

where the relative change in total energy is calculated according to

$$\Delta E \equiv \frac{E(t) - E(t = 0)}{E(t = 0)} \tag{4.22}$$

The RK-4 fixed-step integrator is used with a time step of 1E-3 seconds and the model is propagated for 15 seconds. This smaller time step is chosen to allow for more accurate results. The validity of this assumption is discussed in Section 4.5.

To ensure a correct implementation of the equations of motion, conservation of energy is required. The initial conditions for the energy check are given in Table 4.5. The total and relative change in energy of the system can be seen in Figure 4.9. The error or relative change in energy is in the order of O(E-16), which is the limit of the double floating point precision of Matlab. This means that the energy of the system is conserved throughout the propagation. With the verification of the separate motions, as well as the verification of conservation of energy, the model is considered verified.

4.5. Integrator selection

To validate the results and ensure accurate results in later simulations, a proper analysis of the different integrator settings is required. In this section, the error of different integrators are compared. A trade-off is made for the most suited integrator for further model analysis.

4.5.1. Error estimation

The error of each integrator can be easily determined using the energy check since the relative change in energy should be zero. As a result, different integrators can be directly compared to each other when the energy check initial conditions are used.
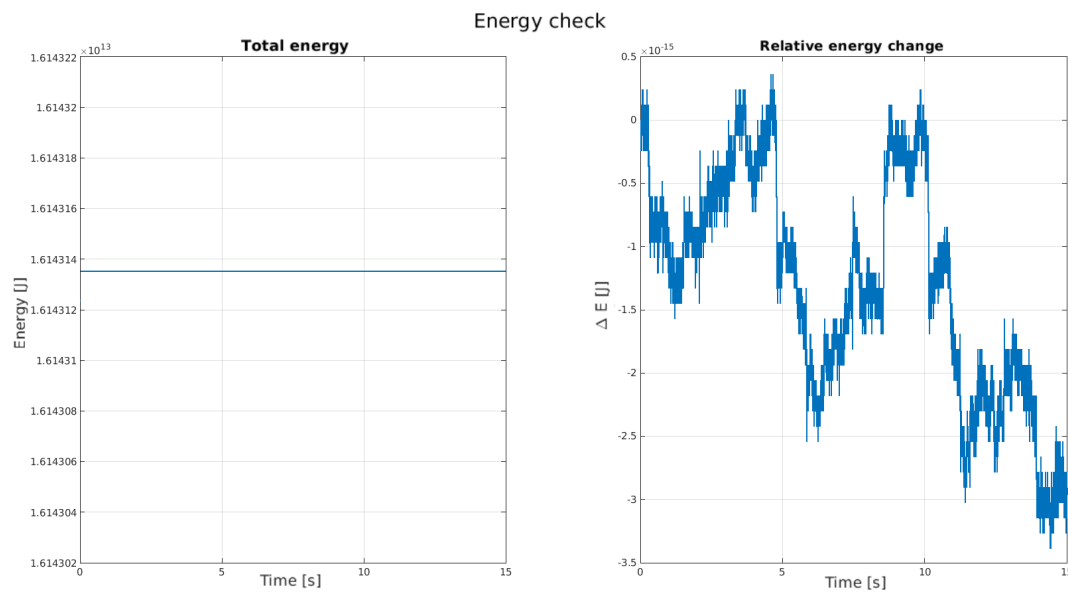
Figure 4.9: Total and relative change in energy of elastic sloshing launch vehicle

For this analysis, four integrators are considered.

- Runge-Kutta-4 (fixed step)

- Dormand Prince RK8(7) (fixed step)

- Explicit Runge-Kutta (4,5) (variable step)

- Adams-Bashfort-Moulton PECE (variable step)

For the Runge-Kutta-4 (ODE4) and Dormand Prince RK8(7) (ODE8), five different step sizes are considered ranging from 1E0 to 1E-4 seconds. For the Explicit Runge-Kutta (4,5) (ODE45) and Adams-Bashfort-Moulton PECE (ODE113) integrators, the absolute and relative tolerances are set between 1E-10 and 1E-14. The run times are also measured and used for the trade-off. For larger step sizes or less strict tolerances, it is possible that any of the state derivatives become non-finite. If this occurs, the error in the relative change in energy is considered to be 100%. The propagation error is considered to be the absolute value of the relative change in energy at the end of a 15 second simulation. A simulation *time-out* of 100 seconds is considered. The required 3.4 seconds for compilation are subtracted from the simulation time. The results can be seen in Figure 4.10 and Figure 4.11.

For the fixed-step integrators there was unstable behaviour for step-sizes larger than 5E-2 and 2E-2 seconds for the ODE8 and ODE4 integrator respectively. These time steps caused some state parameters to become infinite. The trend of decreasing global truncation error can still be observed in the first 3 steps of the ODE4 solver where it seems to level off for time steps smaller than 1E-2 seconds. A similar minimum for the global truncation error can be observed for the ODE8 solver. A small increase in error can be observed for increasingly smaller step-sizes. Random rounding errors due to floating point precision become more dominant for these smaller time steps.

The variable step solvers all timed out, regardless of the chosen tolerance settings. It was observed that this effect mainly occurred at the start of the simulation where time-steps as small as 1E-5 seconds were required. This effect is attributed to the variable step integrators not being able to handle the non-quiescent starting conditions that are used. As a result of the time-out, the error estimates are only based on less than a second of computational time and should be dismissed.

A launch vehicle generally does not start with large (angular) accelerations, slosh mass offsets and bending. A different set of simulations is performed with different starting parameters than those in Table 4.5. The mode performance $\bar{\eta}$ and its derivative $\dot{\bar{\eta}}$ are set to 0. The initial inertial velocity of the vehicle is also set to 0 with an altitude of 0 m. A non-zero massflow rate of $\dot{m} = -1000$ kg/s is introduced to the vehicle which produces a constant thrust of $2.936E6$ N.

The energy of a mass-varying system is not constant. This means that the error needs to be estimated based on simulated data.

Figure 4.10: Maximum simulation error of 10 second simulation for different integrators and settings using energy check starting parameters
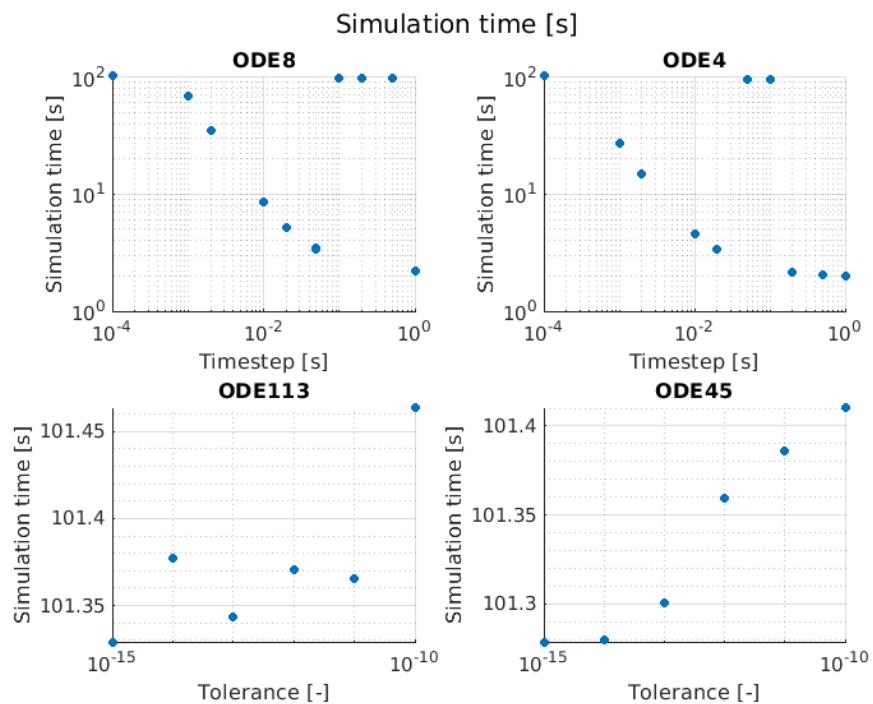
Figure 4.11: Simulation time of 10 second simulation for different integrators and settings using energy check starting parameters. Time of 100+ indicates simulation time-out

From Figure 4.10, it can be seen that minimum global truncation error is obtained with the ODE4 solver, at a time-step of approximately 1E-2 seconds. The simulation is ran for 10 seconds and the final altitude is stored. The error of this value is considered to be negligible. Knowing that random errors become more apparent for smaller step sizes, the minimum allowed step size for the variable step integrators is also set to 1E-3. The results can be seen in Figure 4.12 and Figure 4.13.

4.5.2. Trade-off

One of the requirements from NLR is the ability to run the code in a hard real-time environment. This allows for model implementation on the flight hardware for future NLR customers. As a results, the simulation time shall be lower than the runtime. For realistic simulation scenarios, fixed step integrators with step sizes smaller than 1E-3 are not feasible for this simulator. A similar pattern can be observed as with the energy check, where these smaller step sizes also introduce significant random rounding errors to the solution. The ODE8 solver shows no improvement in accuracy at the cost of a higher simulation time and is therefore discarded.

The minimum step-size setting of 1E-3 seconds allows the ODE45 integrator for very accurate and fast results, mostly independent of the tolerance setting. A different trend can be observed with the ODE113 solver, which shows a significant decrease in accuracy for tolerances below 1E-11. This is expected, since ODE113 generally requires more strict tolerances due to its large step sizes. It can be seen in Figure 4.12 that the error of the ODE45 solver is approximately 25 nm, which is considered to be well within run-to-run variance. The simulation time is similar to the ODE4 solver at time-steps equal to or larger than 1E-2 seconds.

It is recommended to use the simulator with either a fixed step Runge-Kutta-4 integrator using time-steps of 1E-2 seconds, or Explicit Runge-Kutta (4,5) with tolerance settings of approximately E-10 for both the relative and absolute, with a minimum allowed time-step of 1E-3 seconds.
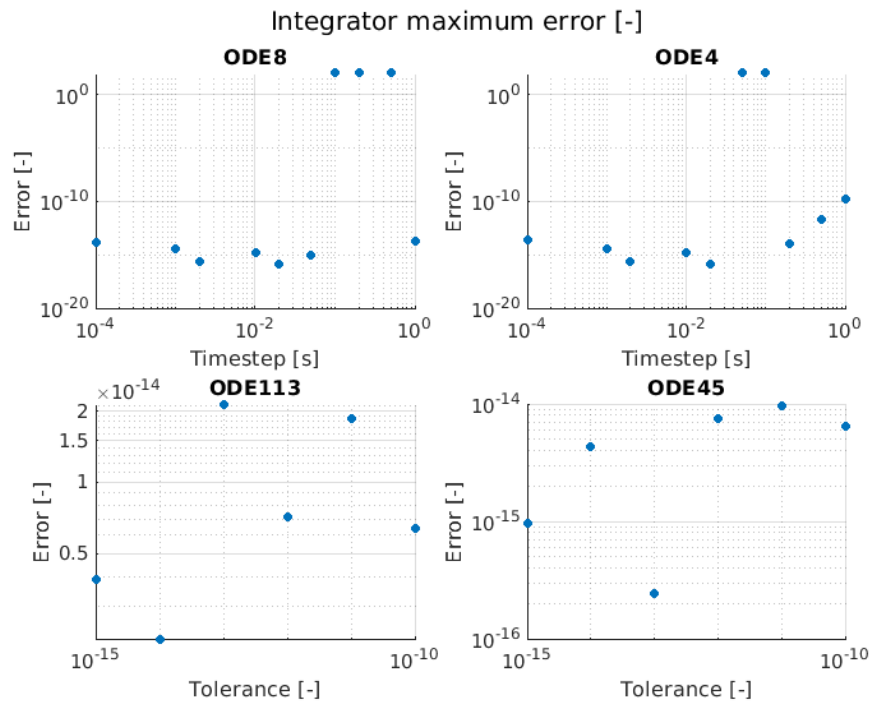

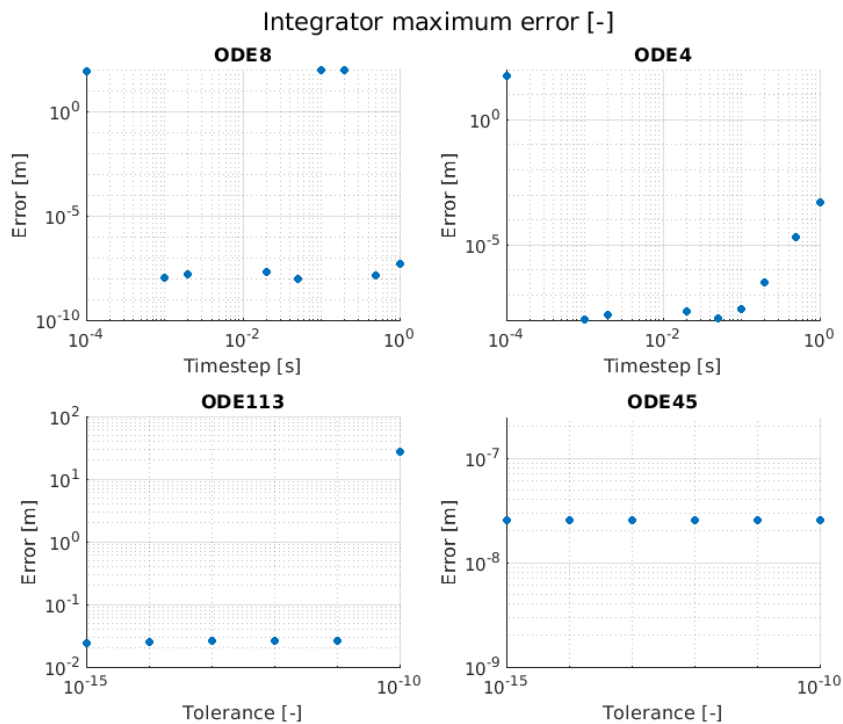Figure 4.12: Maximum simulation error of 10 second simulation for different integrators and settings during ascent
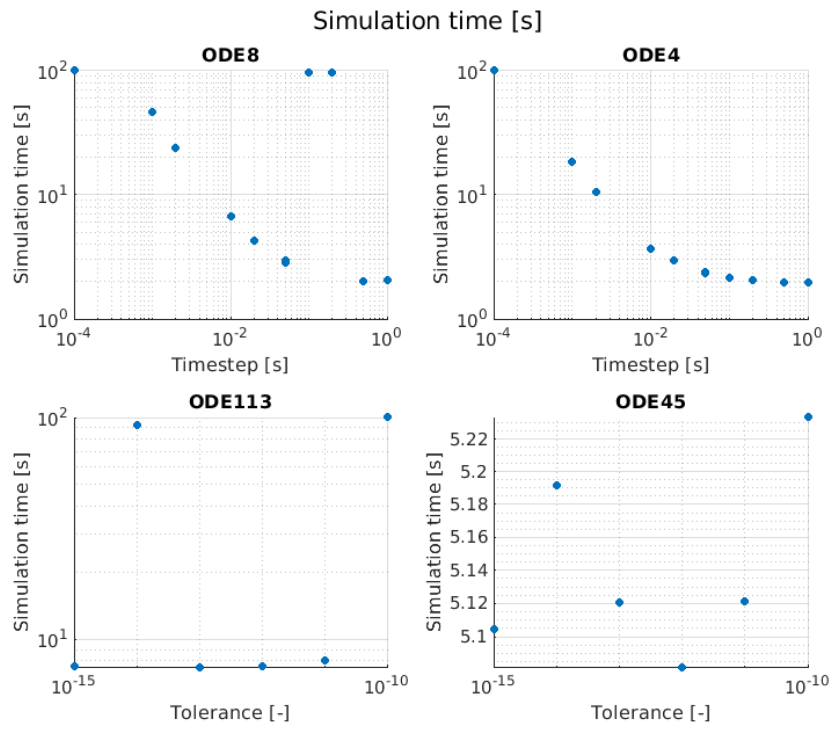
Figure 4.13: Simulation time of 10 second simulation for different integrators and settings during ascent

5

Model validity for sounding rockets

In this chapter, the validity of the non-rigid body model is determined using flight data from the Stratos III sounding rocket. The Stratos III sounding rocket is built by the student team Delft Aerospace Rocket Engineering (DARE) from the TU Delft. The launch of Stratos III took place on July 25, 2018 at 3.30 AM CEST. Approximately 20 seconds into the flight, an anomaly occurred which resulted in a loss of the vehicle.

This vehicle is chosen to determine the model validity since the anomaly was hypothesised to be a result of non-rigid body effects [29]. Specifically the flexibility of the vehicle is considered to be a potential cause of failure. By comparing a traditional rigid body simulation with the verified non-rigid body model, these effects can be further analysed, providing more information for solving the problem for future Stratos launches.

In Section 5.1, the general input parameters are given for the Stratos III rocket, including flight data. In Section 5.2, the flight data is compared to both a rigid body, as well as the developed non-rigid body model. A discussion on the results is given in Section 5.3.

5.1. Stratos III available data

Stratos III is a launch vehicle with a length of approximately 8.2 meters and made mostly from carbon fibre. A picture of Stratos III before launch can be seen in Figure 5.1.

It uses a hybrid propellant system: the oxidiser is Nitrous Oxide (NO_2), which is stored at 60 bars before launch. The oxidiser is self-pressurising to approximately 40 bars, discarding the need for any additional pressurants. The fuel is a self-made mixture of sorbitol and paraffin. The thrust of the vehicle changes significantly over the burn time, consisting of 2 distinct phases. In the first phase, the oxidiser tank mostly consists of liquid nitrous, resulting in a high (peak) thrust. Over the burn, the Oxidiser-To-Fuel (O/F) ratio changes significantly. The thrust decreases, with a sharp drop at approximately 20 to 25 seconds. At this point, the engine runs out of liquid nitrous and burns in the gaseous phase until the tank is empty. The solid fuel is cast in a cylindrical grain, slowly burning outwards towards the walls of the tank. For the model, the mass flow is purely estimated based on the change in mass in the payload manual of Stratos 3, and a constant O/F ratio is assumed. The thrust curve from one of the static engine tests, as well as the estimated curve used for input of the model is given in Figure 5.2.

Just before launch, during the filling procedure, the load sensor that was supposed to measure the fluid level was defective. As a result, it was uncertain how much oxidiser was present in the tank at launch. For this analysis, it is estimated that the tank was filled for 70%.

Using the information for the different vehicle dimensions from the Stratos III payload manual, approximations can be made for the mass parameters of the vehicle. The inertia for the model was obtained by performing the analytical calculations from Section 4.1.3. The values that are used to determine the mass parameters are given in Table 5.1.

The inertia around the roll-axis was approximately 2 times as high in the model, likely attributed to propellant slipping being considered here. Other differences, specifically the difference in the rate of change of these parameters, is mostly attributed to the assumption of a fixed O/F ratio. The modelled values are of the same order of magnitude and are considered to be sufficiently accurate to model the Stratos III flight. The modelled and payload manual values can be found in Figure 5.3.

For the flexibility of the vehicle, the eigenmode frequencies and mass-normalised deflection were not available. ANSYS was used to estimate the natural frequency of the first bending mode of Stratos III.

Figure 5.1: Stratos III in the launch tower

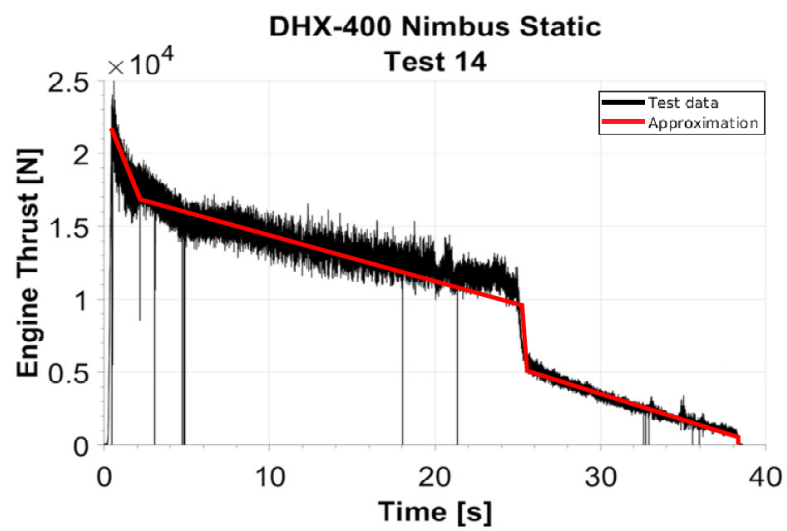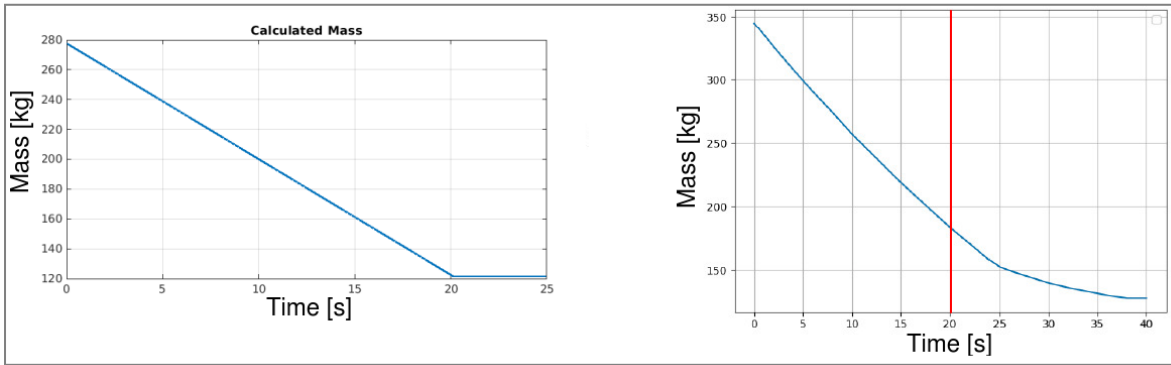

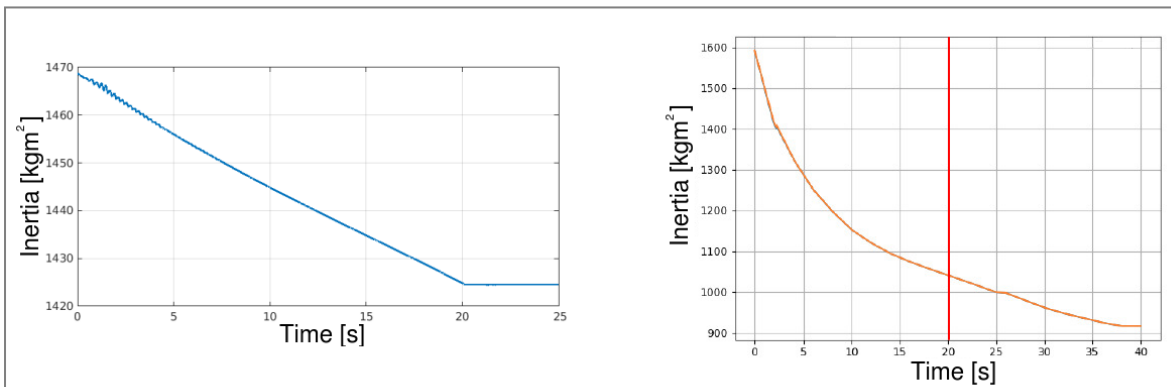Figure 5.2: Test data and estimated thrust curve for Stratos III
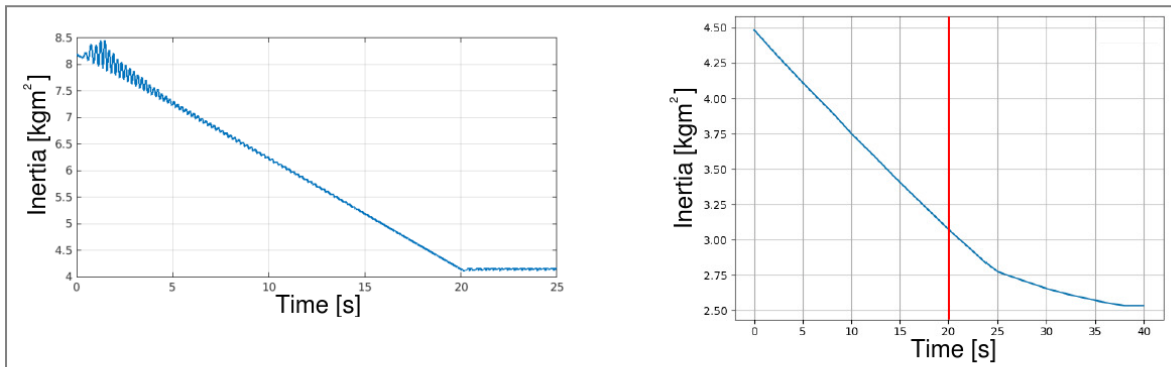
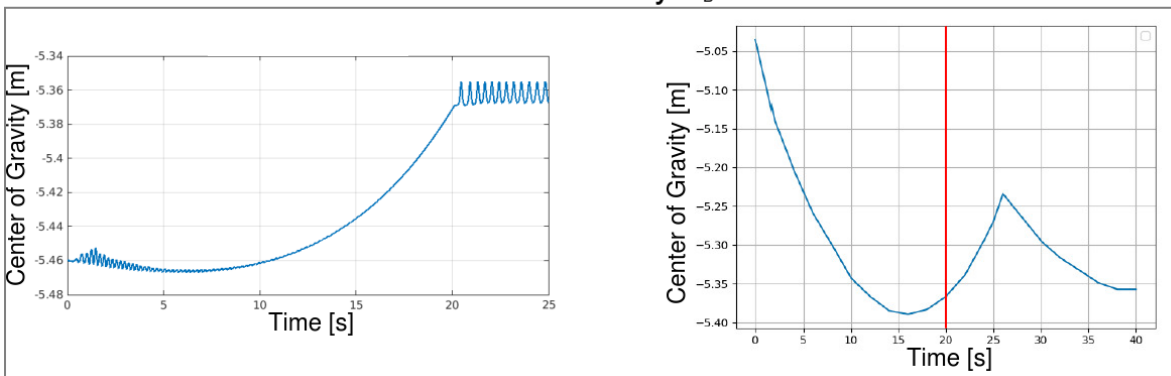Figure 5.3: Mass parameters based on approximations (L) and payload manual parameters (R). Area of interest from the payload manual is before 20 seconds, indicated by the red line

Table 5.1: Assumed vehicle parameters for Stratos III simulation

Structure mass	94	[kg]
Engine mass	10	[kg]
Structure inertia (I_{xx} , I_{yy})	4 , 1400	[kgm^2]
Engine inertia (I_{xx} , I_{yy})	0.112 , 0.088	[kgm^2]
Inner radius	0.28	[m]
Vehicle length	8.2	[m]
Oxidiser tank height	4.15	[m]
Fuel tank height	1.4	[m]

Due to restrictions in the TU Delft ANSYS license, only uniform materials such as aluminium or titanium could be used for the modal analysis. Stratos III is largely manufactured with carbon fibre which could not be used with the available ANSYS license. Aluminium was used for this analysis. Therefore a very conservative model, a hollow aluminium beam with equivalent length to Stratos III, was implemented. In reality, the carbon fibre will likely have a detrimental influence on the mass-normalised deflection compared to this model. When performing a free-free modal analysis on this model, it was found that the natural frequency of the first mode was approximately 33 Hz, with a maximum mass-normalised deflection of 0.27 m. This natural frequency is assumed to be constant throughout the flight.

5.2. Determining model validity using using Stratos III
With the parameters from Section 5.1, the validity of the non-rigid model for sounding rockets can be determined. A variety of O/F ratios were considered to see the effect on the flight of the Stratos III rocket. The modelled data from Figure 5.3 is the result of a constant O/F of 2.2. This results in an empty fuel tank at around 20 seconds, causing a large decrease in thrust at that time. When any of the tank empties, the thrust is quickly decreased to approximately half of its original value and decreasing to zero in approximately 10 seconds. This behaviour is equivalent to the engine moving from the liquid to the gaseous phase.

5.2.1. Comparing Mach number
To get a first estimate of the validity of the simulator, the simulated Mach number is compared to the estimated Mach number from the flight data. This comparison gives insight in the validity of the velocity calculations and atmosphere model (speed of sound). The comparison between the estimated and modelled Mach number can be seen in Figure 5.4.

The Mach number shows a good similarity over the flight time for the Stratos III rocket. In the final phase, the thrust of the vehicle seems to increase just before the anomaly. The estimated thrust curve from Figure 5.2 underestimates the thrust between 20 and 25 seconds. Furthermore, it was speculated that the mass flow rate and therefore thrust was higher than the ground tests, likely due to the acceleration acting on the vehicle. Both effects could've caused a higher thrust late in the flight, explaining the difference between both models.

5.2.2. Comparing body acceleration
Next, the acceleration acting on the vehicle is compared to the modelled acceleration in Figure 5.5. As stated before, the thrust drops significantly at approximately 20 seconds. In reality, it is unlikely that the fuel tank runs out of fuel before the oxidiser tank empties. This would result in a burn-through since the fuel itself acts as an insulation between the hot combustion gasses and the tank walls. Nonetheless, such a decrease in thrust is likely to have occurred due to a transition from the liquid to the gaseous phase. The measured and modelled acceleration can be seen in Figure 5.5.

A few interesting observations can be made from this figure. First of all, the heavy vibration at the start of the burn is shown in both datasets. Although it cannot be explained with certainty for the flight data due to the absence of wind data, in the model this occurred due to wind hitting the vehicle just after leaving the tower. This resulted in an aerodynamic disturbance that was damped out over time due to the static margin of the vehicle. At approximately 15 seconds, the vehicle starts to wobble. When the thrust decreases at 20 seconds, the vehicle starts to oscillate heavily. The magnitude of this oscillation increases when the rate of change in acceleration or the slosh mass increases. The slosh mass over time can be seen in Figure 5.6. The slosh mass at the time of decreasing thrust was approximately 15 kg.
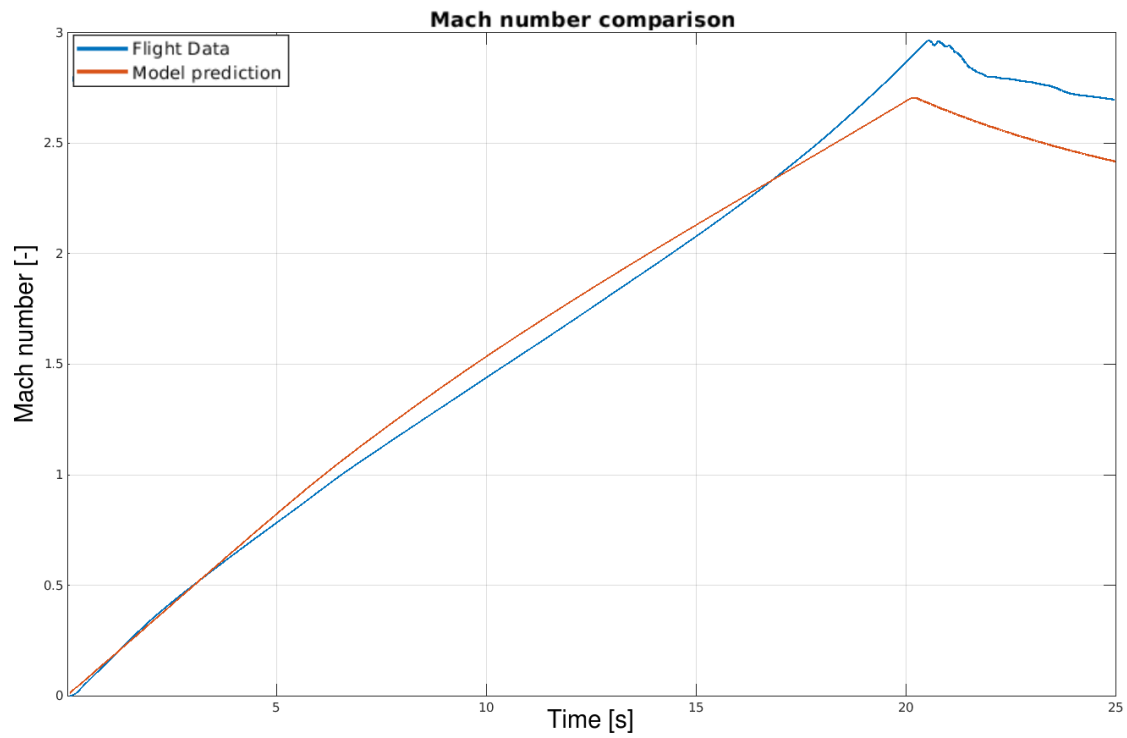
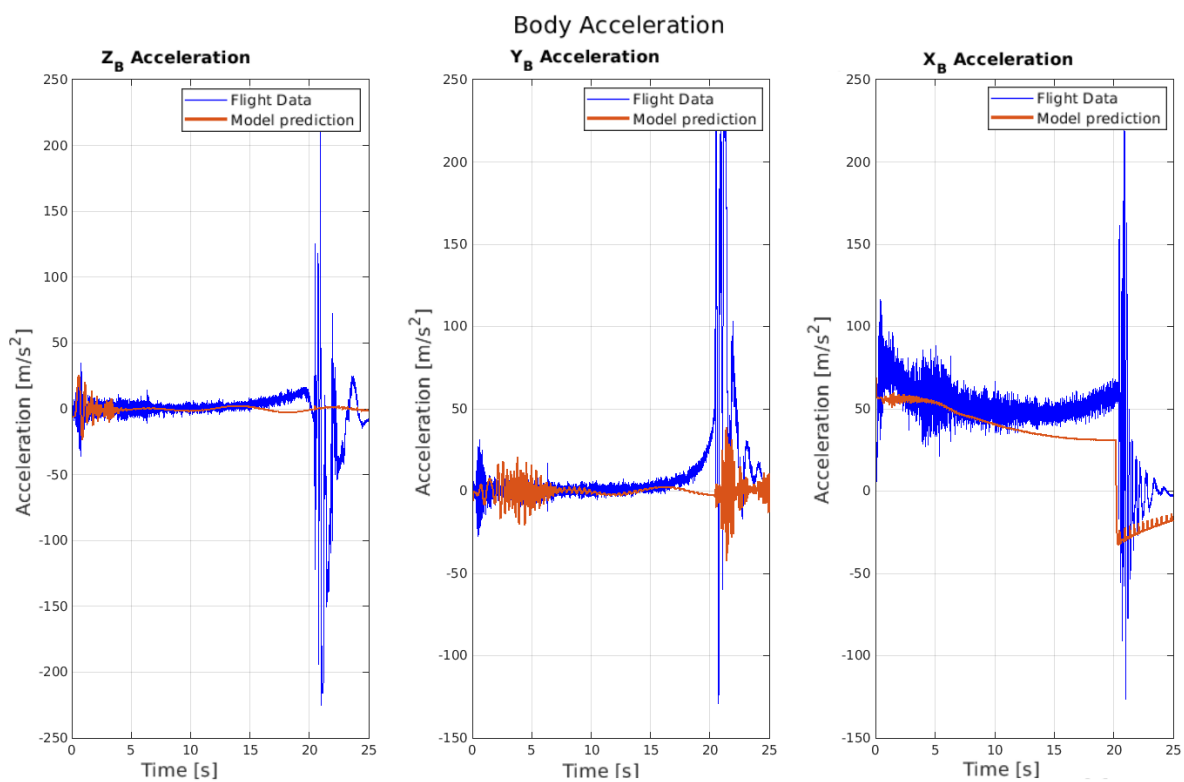Figure 5.4: Estimated and modelled Mach number

Figure 5.5: Estimated and modelled body acceleration
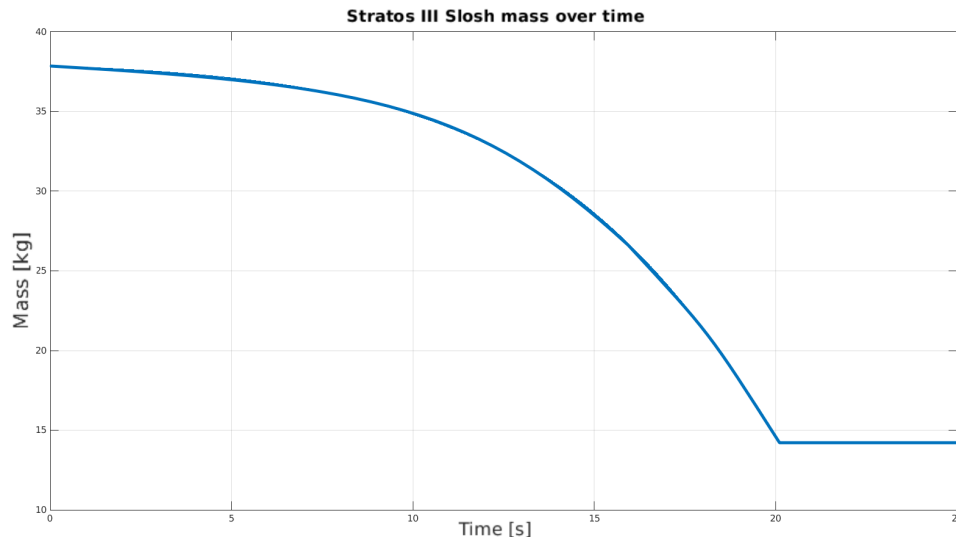
Figure 5.6: Calculated oxidiser slosh mass

This results becomes especially interesting when comparing it to the rigid-body data. As can be seen in Figure 5.7, the rigid body simulator does not destabilise for large changes in axial acceleration. This means that the destabilising either occurs due to the sloshing liquid, or due to the flexibility of the vehicle. Although not considered in the non-rigid body model, it is likely that a large portion of the liquid remains in the tank due to the rotational speed of the vehicle. This could result in a sloshing motion. The flexibility remains within margin when comparing it to the beginning of the flight as seen in Figure 5.8, providing strong evidence that the sloshing motion can have a destabilising effect on Stratos III.

Such an anomaly also occurred for different scenarios. When a sudden gust of wind hit the vehicle late in the flight, the quick change in resulting aerodynamic forces would cause the vehicle to tumble. This occurred for both the rigid and non-rigid body model, making it unlikely that this was the main cause of the Stratos III anomaly. More information on the different failure modes and their likelihood can be found in [29].

5.2.3. Comparing body angular velocity

The results can be further analysed by looking at the angular rates. The angular velocity shown here is the angular velocity between the rocket frame and the world frame, or ECI and BODY in the model. The results can be seen in Figure 5.9.

The anomaly can be clearly observed in the flight data, but is not as clear in the modelled data. First, the pitch and yaw rates from the flight data are taken separately and compared to the model data between 0 and 20 seconds. The results can be seen in Figure 5.10.

The pitch rate shows a similarity for a large part of the flight, diverging at around 12 seconds. This is a similar divergence that can be observed in the acceleration data. The yaw rate starts to diverge from 9 seconds, while still showing an osculating behaviour later in the flight. These differences can be partially explained by the difference in inertia between the flight data and model. However, it is more likely that the aerodynamics were different from the model. No recent wind data was available before launch. Small gusts of wind could have caused the yaw and pitch rate to increase. As discussed earlier, these gusts also caused a divergences of the body rates.

The roll rate, which is shown in Figure 5.11, also shows similar behaviour from 6 seconds onward, flattening out for most of the flight. The oscillation in the flight data for the first 6 seconds is not observed in the model.

The modelled roll rate is about 5 times smaller than the estimated roll rate from 7 seconds. This can be partially attributed to the higher inertia of the model which takes into consideration propellant slip. However, it is more likely that the aerodynamic properties of the vehicle were different than modelled. Fin-offset and other manufacturing tolerances can have a large influence on the aerodynamic properties of the vehicle which could have induced a higher roll rate. Fin flexibility also might have caused the roll rate of the vehicle to increase. The modelled aerodynamic coefficients are purely based on empirical relations and can also differ from the actual vehicle.

Figure 5.7: Flight, non-rigid model and rigid model acceleration data

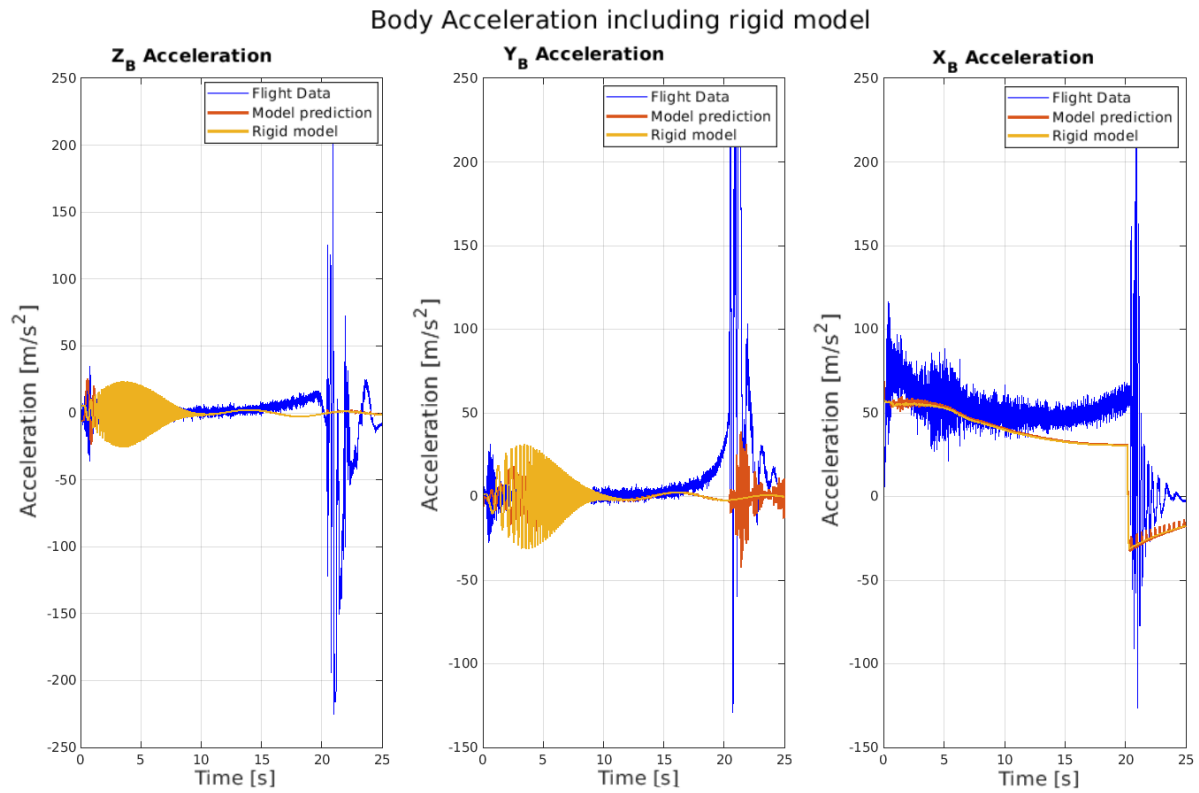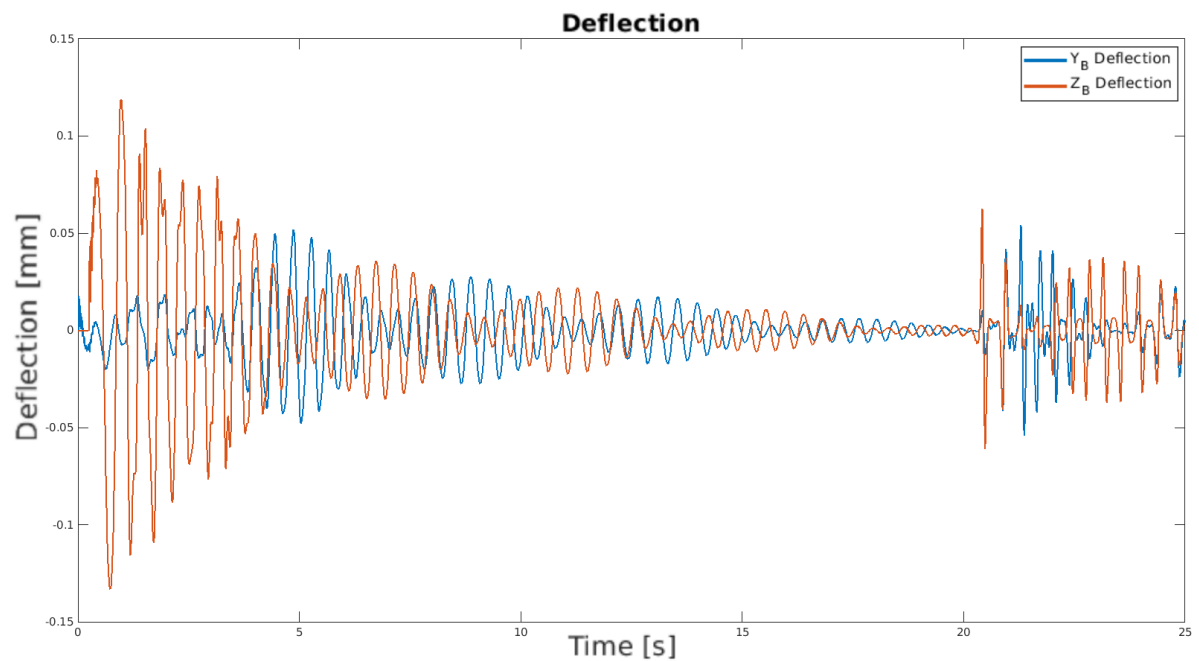Figure 5.8: Modelled Stratos III deflection
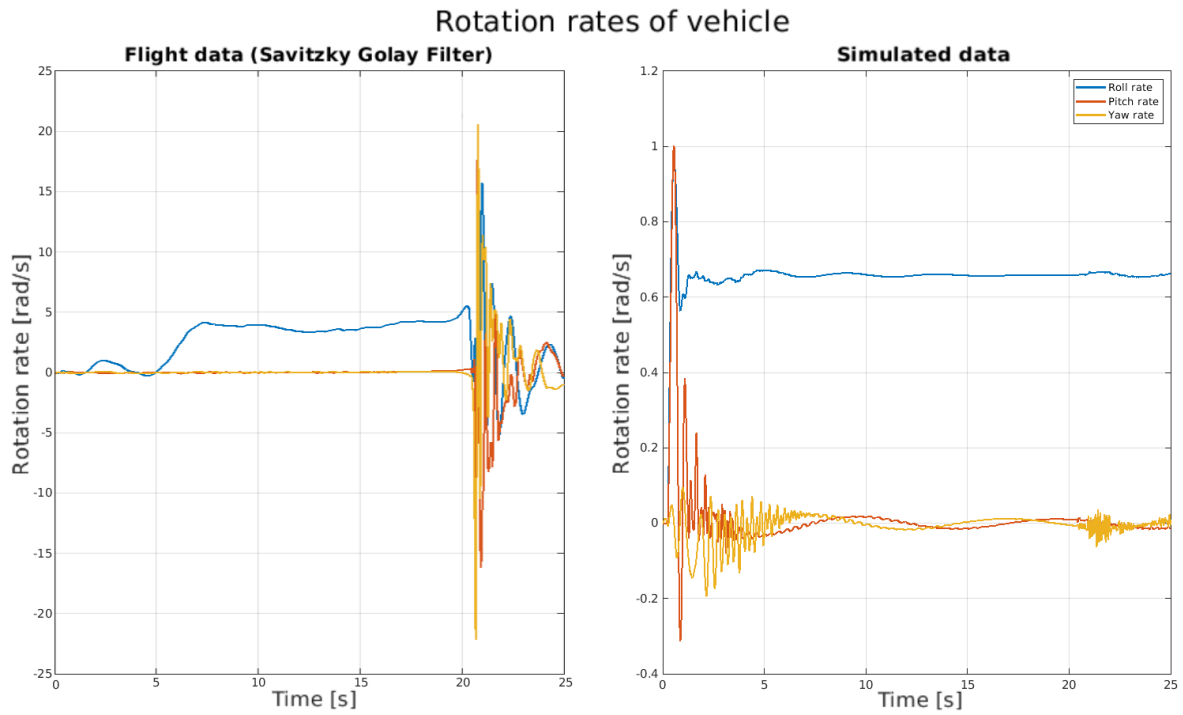
Figure 5.9: Angular rates of Stratos III during flight (L) and in the model (R). Stratos III shows higher rates as can be seen in the difference in Y-axis scaling
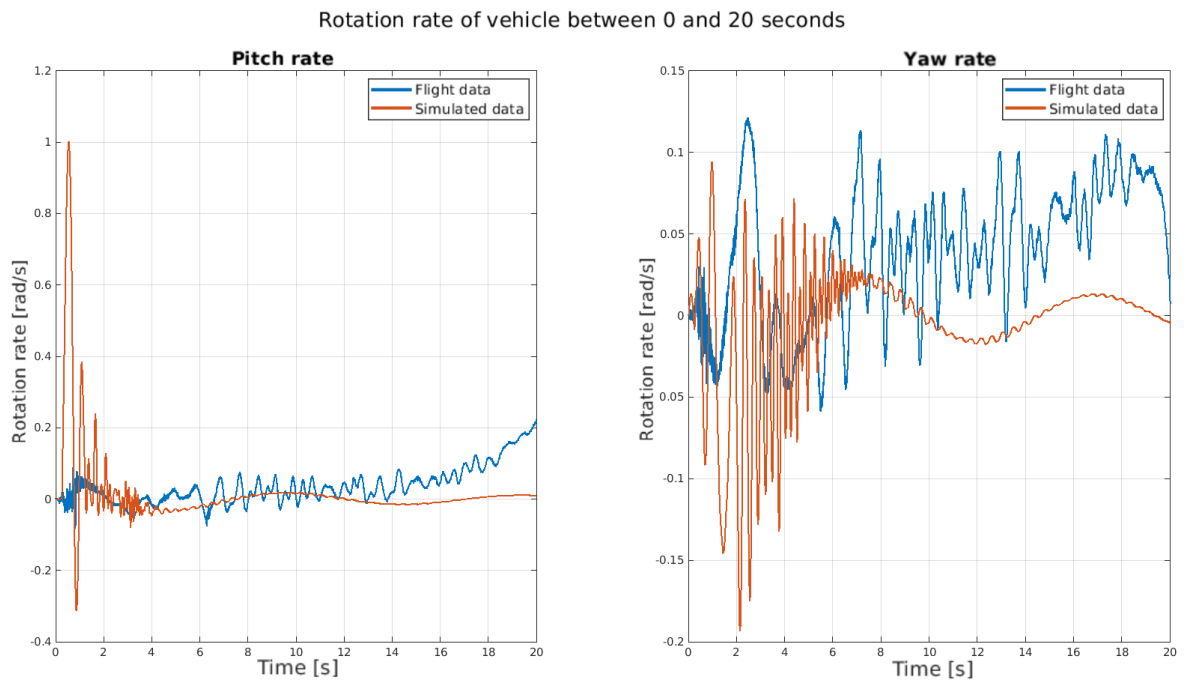
Figure 5.10: Pitch and Yaw rate of Stratos III
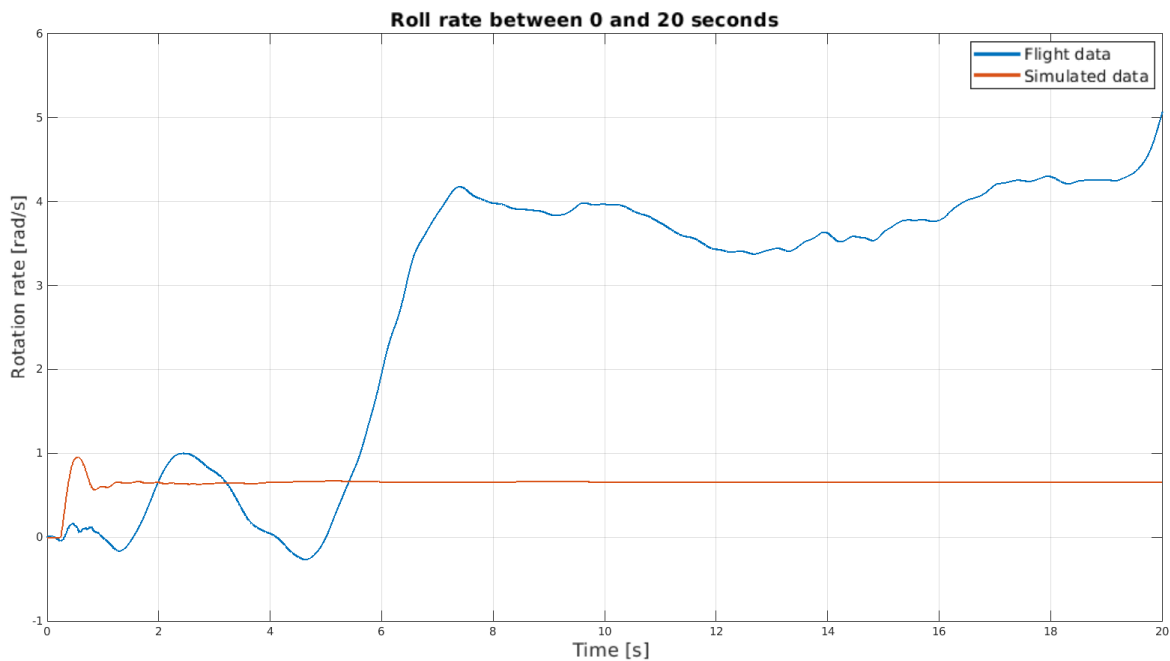
Figure 5.11: Roll rate of Stratos III

Several mitigation strategies are designed for the Stratos IV launch vehicle. These effects, such as a roll-control system, were also analysed. Stratos IV is planned to include a roll-control system with a bang-bang control algorithm that should reduce the roll-rate of the vehicle. This controller is added to the model to look at the effect that it has on the trajectory in this specific scenario of decreasing thrust. Even for very small rotational rates (<= 2 °/s), the roll-control system was not able to stabilise the vehicle for the decrease in thrust and wind gust scenario. It was able to successfully reduce the roll rate of the vehicle, but the sudden decrease in thrust still caused the remaining slosh mass to tumble. It should be stressed that this does not mean that the roll-control system will have no effect on Stratos IV. The roll-control system did seem to have a stabilising effect on the trajectory in general. The roll rate with and without roll control are given in Figure 5.12. This figure shows that the controller is able to effectively decrease the roll rate of the vehicle. The pitch and yaw rate are given in Figure 5.13. Regardless, the pitch rate still shows a destabilising behaviour when the thrust is decreased. However, by only controlling the roll rate, the pitch and yaw rate also seem significantly more stable during flight. Future research into this behaviour is recommended in Section 7.2.2.

5.3. Conclusion

Although the dataset is limited, Stratos III flight data was chosen to compare to the modelled data. Specifically, as stated before, because it is likely that non-rigid body effects caused the anomaly of the vehicle. This suggests that a non-rigid body simulator is required to observe this effect. Indeed, it was shown that a non-rigid body model is able to model effects that can't be observed in a rigid body model. However, the Stratos III launch vehicle was also chosen because the model requires complex aerodynamic information which is not readily available for other vehicles. Although this data was also available for the NLR SMILE launch vehicle, no flight data was available to compare with the model. Since the dataset is limited, and the flight can't be modelled exactly, it cannot be stated with certainty that the model is validated for flight.

Nonetheless, the model shows very promising results for the Stratos III launch vehicle. It can provide more insight into the non-rigid body effects of this sounding rocket. Important flight parameters, such as body velocity, environment and accelerations can be estimated with decent accuracy. Therefore, it can be concluded that the non-rigid body model is valid to be used to estimate the Stratos III flight. More detailed data, specifically aerodynamic, wind, mass flow rate and O/F ratio over time, is required to fully validate the model for flight. A more detailed analysis on the non-rigid body effects is performed in Chapter 6.
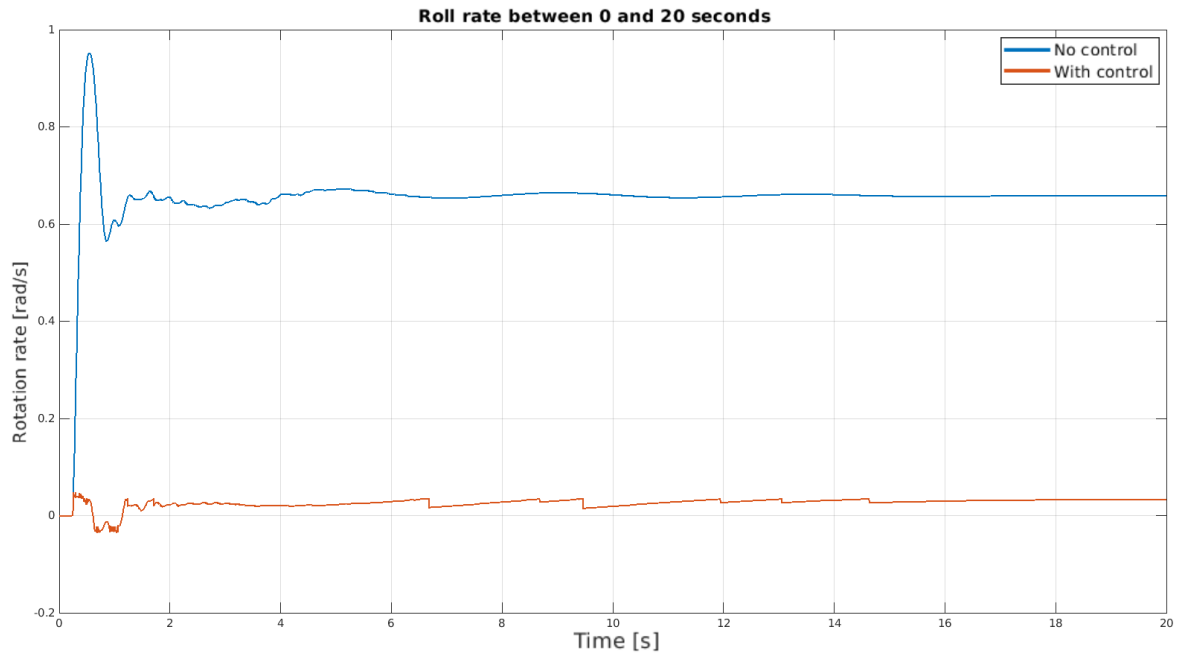
Figure 5.12: Comparison of roll rate with and without roll control
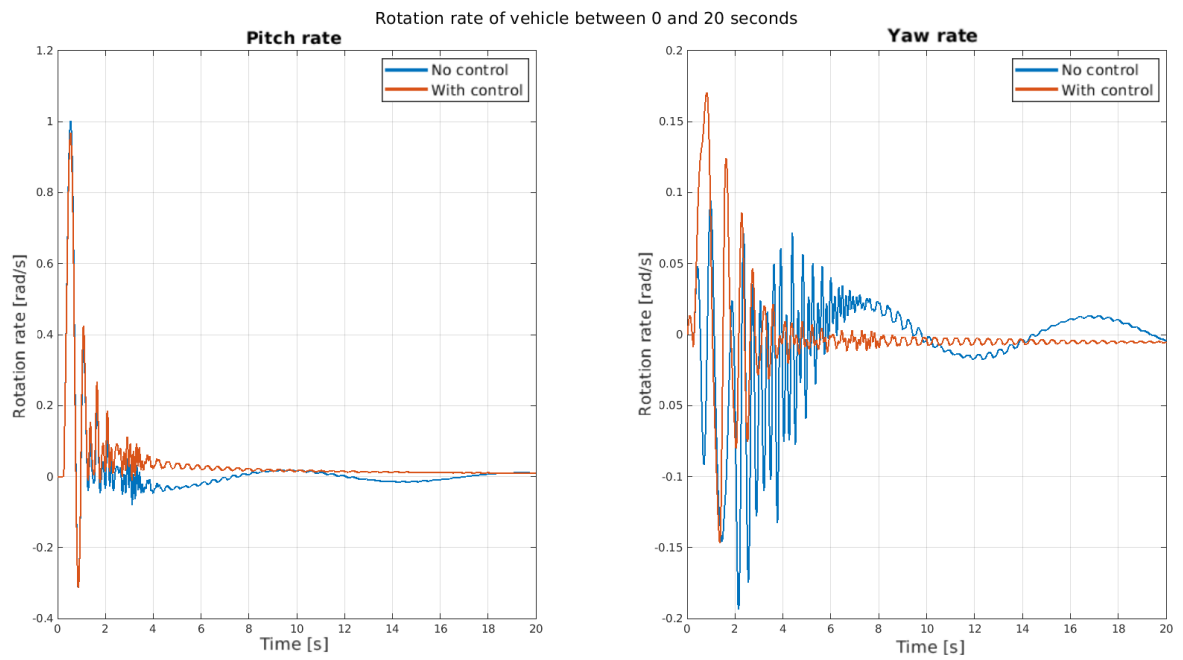
Figure 5.13: Comparison of pitch and yaw rate with and without roll control

6

Sensitive parameters for non-rigid body models

From Chapter 5, it was found that non-rigid body effects can potentially play an important role for sounding rockets. It was suggested multiple times that the slenderness of the vehicle, combined with the lack of slosh mitigation strategies, caused severe non-rigid body effects to occur in the Stratos III launch vehicle. In this chapter, a statistical analysis is performed on these suggested parameters to determine which variation of parameters shows significant changes in the body flexibility and sloshing motion. In Section 6.1, the key design parameters that are analysed are discussed and an N-way ANalysis Of VAriances (ANOVA) is performed. In Section 6.2, the sensitivity for changes in these key parameters is measured. Section 6.3 discusses the controller design process for non-rigid bodies using rigid-body models. The results are summarised in Section 6.4.

6.1. Key design parameters for non-rigid body effects

Based on the equations from Chapter 2, as well as knowledge from the launch of Stratos III, key parameters are determined that may cause a large disturbance to the rigid body due to non-rigid body effects. The effects that will be considered are

- Vehicle length (L)

- Vehicle diameter (D)

- Slosh damping ($Damp$)

- Mass flow rate ($\dot{m}$)

- Tank fill ratio (F)

These parameters are hereafter called the analysis parameters. The length of the vehicle largely determines the eigenfrequency of the vehicle, if all other parameters are kept the same. As a result, the frequency of the sloshing motion will also change. The diameter is the main driving parameter for the slosh mass, where a larger diameter results in a higher slosh mass. Increasing the diameter also causes an increase in natural frequency, which will change the flexible motion as well. The damping rate of the slosh mass determines how quickly a disturbance in the slosh pendulum is damped out. A higher damping ratio will cause less overall sloshing and is expected to result in a smaller disturbance. The mass flow rate is directly correlated to the thrust, which is the main driving force for the flexibility motion. Changing it can therefore dramatically change the flexibility and sloshing motion of the vehicle. It also directly influences the change in slosh mass over time. Finally, the tank fill ratio also has an influence on the slosh mass, where a smaller tank fill ratio (smaller fluid level) will result in a smaller slosh mass. Furthermore, it directly influences the relation between stationary and sloshing propellant mass. The expected effects are summarised in Table 6.1.

Parameters such as the stiffness are not considered. Stiffness generally can't be varied arbitrarily since it is material dependent. The choice of material is non-trivial and is not considered in this research. It is expected that this parameter only affects the flexibility.

Table 6.1: Expected effects in non-rigid body effects for an increased analysis parameter

Increased parameter	Expected effect on flex	Expected effect on C.G.
Length	Increase	Increase
Diameter	Decrease	Increase
Damping	Decrease	Decrease
Mass flow rate	Increase	Decrease
Fill ratio	Neutral	Increase

Table 6.2: Representation of Design of Experiments

Analysis parameters					
Run	Length	Diameter	Damping	Mass flow rate	Fill ratio
1	High	High	High	High	High
2	High	High	High	High	Low
3	High	High	High	Low	High
…	…	…	…	…	…
32	Low	Low	Low	Low	Low
Non-rigid parameters					
	η_{tot}	η_{max}	$C.G._{tot}$	$C.G._{max}$	
1	A_1	B_1	C_1	D_1	
2	A_2	B_2	C_2	D_2	
3	A_3	B_3	C_3	D_3	
…	…	…	…	…	
32	A_{32}	B_{32}	C_{32}	D_{32}	

This means that the mass-normalised deflection is purely based on length and diameter for this analysis. Different propellants are also not considered. The non-rigid slosh parameters that are considered for this analysis are normalised with respect to mass and the slosh mass ratio is independent of density. Therefore, it is expected that different propellants will result in negligible differences in non-rigid body effects on the total vehicle.

A Design of Experiments approach is chosen to determine which independent variables are significantly contributing to the non-rigid body effects of the vehicle. The analysis parameters are given a high and low value. By considering all combinations of variables, an analysis can be performed that gives the sensitivity of each parameter on the non-rigid body effects. An overview of this method can be found in Table 6.2. The variables that are considered to define the non-rigid body effects are the maximum and total mode performance η, as well as the maximum and total C.G. offset in the $Y - Z$ plane. These parameters are hereafter considered to be the non-rigid parameters. The mode performance is chosen because it provides a good representation of the flexibility of the entire vehicle over time. Since mode performance can be considered the normalised deformation of the vehicle, η is considered equivalent to vehicle flex. The $Y - Z$ C.G. offset is chosen as it gives a good representation of the slosh motion of the slosh masses, while directly normalising the motion to each sloshing mass. The C.G. offset will directly influence the moment that is induced on the vehicle due to sloshing effects. It is chosen to consider both the cumulative as well as the maximum values of these parameters as both can provide valuable insight to this analysis. The total flex is calculated using

$$\eta_{tot} = \int_0^t (|\eta_y| + |\eta_z|)dt \tag{6.1}$$

The maximum flex is calculated by simply taking the maximum of $\bar{\eta}$ over the simulation time. An equivalent approach is used to calculate the maximum and total C.G. offset. In order to avoid differences in simulation time due to tanks running empty, the simulation is run for $t = 12$ s.

6.1.1. N-way Analysis of Variance (ANOVA)
In order to determine the dependency of these variables on the non-rigid parameters, ANOVA is used. ANOVA is a test of the statistical significance of differences between several groups [13].

Table 6.3: ANOVA analysis parameters

Parameter	*High*	*Low*
Length	8.5 [m]	7.5 [m]
Diameter	0.3 [m]	0.26 [m]
Damping	0.8 [-]	0.5 [-]
Mass flow	30 [kg/s]	20 [kg/s]
Tank fill	1 [-]	0.8 [-]

Table 6.4: ANOVA analysis parameters

L - D [m]	ω_N [Hz]	Deflection [m]
8.5 - 0.26	28.43	0.286
8.5 - 0.3	32.13	0.266
7.5 - 0.26	36.4	0.305
7.5 - 0.3	41.16	0.283

For this study, each analysis parameter is one group which can have a value *high* and *low*. These values are given in Table 6.3.

With 5 parameters, and 2 options per parameter, the total number of required runs is $2^5 = 32$. For each of these 32 runs, the set of parameters that is considered is unique. For a changing length, diameter and tank fill, other vehicle parameters besides those considered here are also changed. Specifically for the length and diameter, the inertia and eigenfrequency of the vehicles will change. For this subset of 4 different options, a finite element analysis was performed to determine the eigenfrequency and maximum deflection of the first two bending modes. Since the vehicle is symmetric, these have the same frequency and deflection in orthogonal directions. A simple hollow beam with a thickness of 2 mm was considered for the analysis. The results are given in Table 6.4 and can be directly implemented in the model.

An input file is created which contains all of the 32 model variations. All non-rigid parameters are saved. The change in total and maximum flex for all different runs is shown in Figure 6.1. This figure shows 32 bars, each for one of the 32 settings for this analysis. The length of the bar represents the vehicle flex at the end of the run. Both the total flex and maximum flex are shown. Similar results can be presented for the C.G. offset, as shown in Figure 6.2. Although the absolute value differs only slightly, the variation between runs shows that there are some significant differences between each run.

This dataset can also be visualised per group. As an example, the total and maximum flexibility for different lengths are given in Figure 6.3. The figure shows two box-whisker plots. The first represents all the 16 results that have a high length setting (8.5 m). The second shows all the results for the low length setting (7.5m). This shows the variation within a specific group. A clear difference can be observed between the two plots, suggesting that the length is a relevant parameter since changing the length significantly changes the flex of the vehicle for otherwise identical settings. The total and maximum flex for different damping ratios are given in Figure 6.4. These values are almost identical, suggesting that damping has a negligible influence on the non-rigid body effects.

6.1.2. Parameter significance

Using Matlab, all groups as well as their interactions are analysed. The results of the 4 non-rigid parameters are considered to be the 4 response vectors. All analysis parameters are grouped. The analysis of variance of the total and maximum flexibility are given in Table 6.5 and Table 6.6.

Parameter F indicates the between-groups mean square divided by the within-group mean square. A large value of F suggests a large difference between the variation within a group as compared to the overall variation. The final column represents p. If this value is smaller than 0.05, the analysis parameter has a statistically significant influence on the non-rigid parameter.

For each of the non-rigid parameters, a table can be created which shows the significance of changing each analysis parameter. This means four tables are created: two for flexibility and two for C.G. offset. This is done since certain parameters might increase the frequency of a certain motion, but not necessarily the amplitude (maximum). This can be an important trade-off parameter if certain levels of flexibility are allowed. This is similar for the C.G. offset.
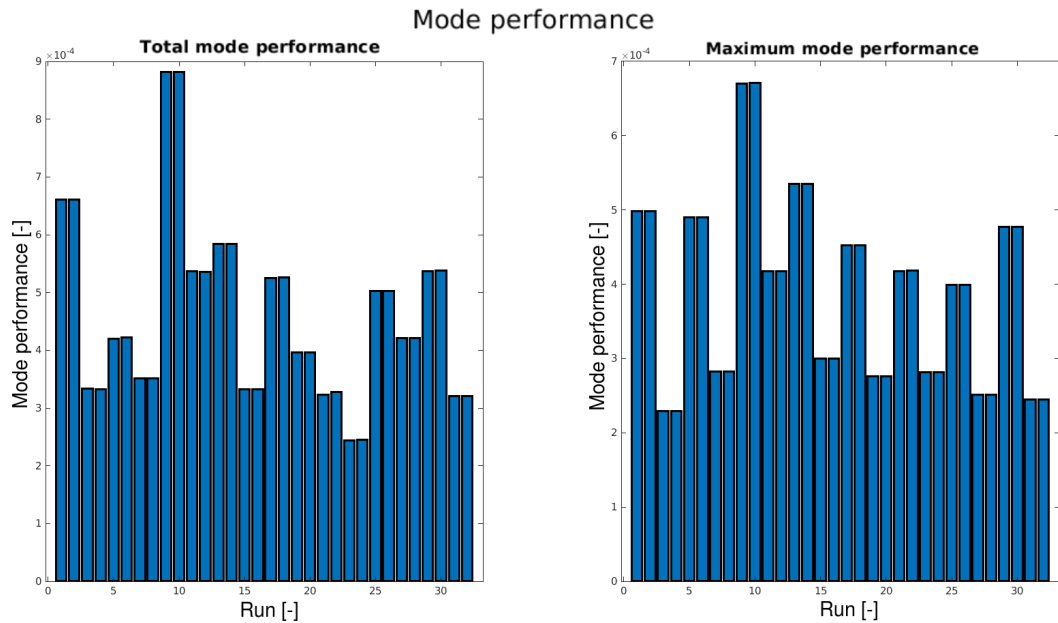
Figure 6.1: Variation in resulting flex for different model parameters
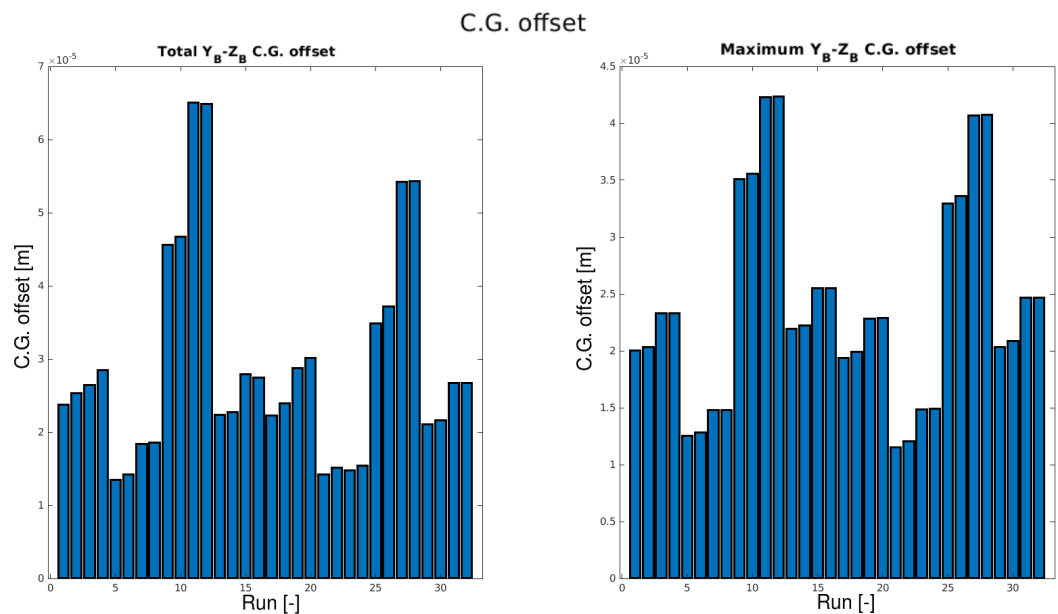
Figure 6.2: Variation in resulting slosh for different model parameters

It can be seen in Table 6.5 that the length ($p = 0.0008$), fill ratio ($p = 0$), mass flow rate ($p = 0$) and diameter ($p = 0.0006$) have a significant influence on the total flexibility of the vehicle. The interaction of the length and fill ratio also has a significant ($p = 0.028$) influence. Similar to the mass flow, this is attributed to the total slosh mass at a given time.

A smaller slosh mass oscillates at a higher frequency and is more likely to cause flexibility within the vehicle. Even for an equivalent simulation time, this can result in an overall larger total flexibility of the vehicle. The damping has no significant influence on the total flexibility of the vehicle.
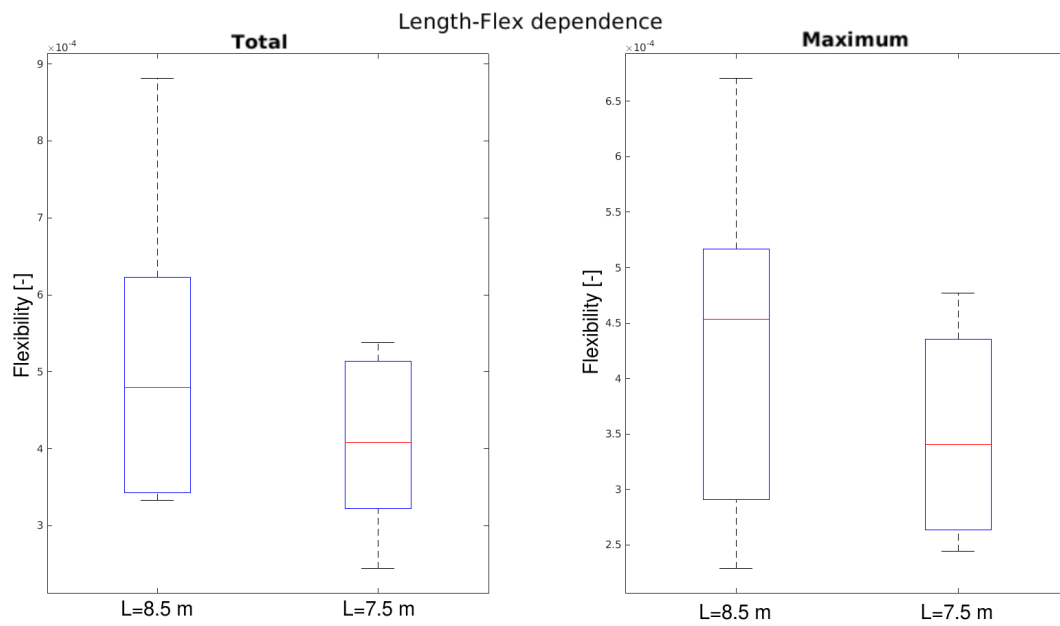
Figure 6.3: Variation in total and max flexibility for different lengths
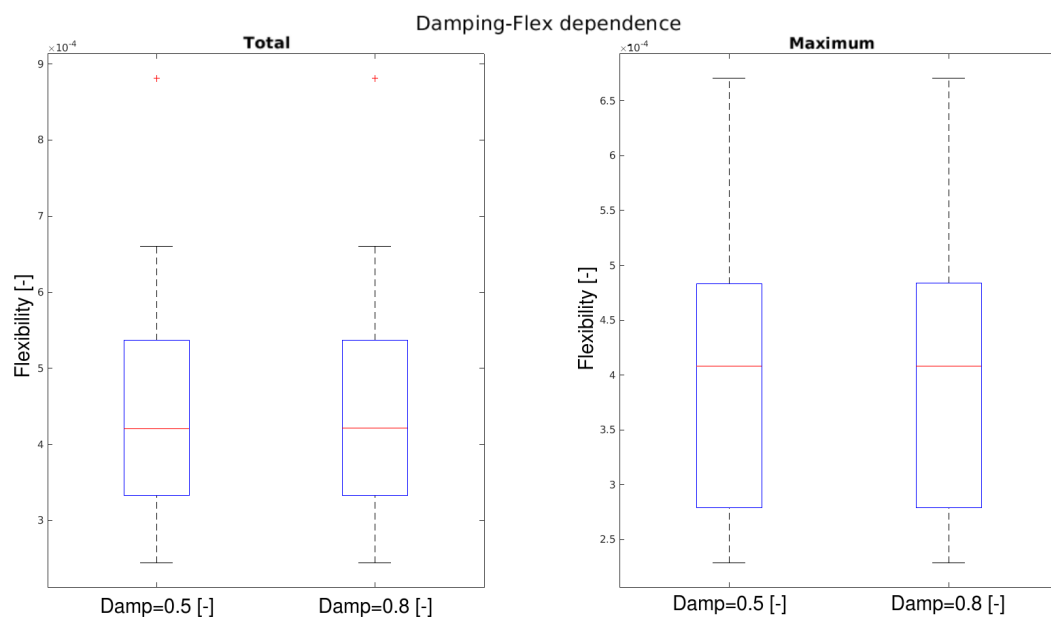
Figure 6.4: Variation in total and max flexibility for different damping ratios

The interaction between length and diameter has a significant ($p = 0.0007$) influence on the maximum flexibility of the vehicle as shown in Table 6.6. This was expected, since this is also considered to be one of the main causes of failure for the Stratos III rocket. The diameter itself has no significant ($p = 0.054$) influence on the maximum deflection of the vehicle.

Table 6.5: ANOVA for total flex

Parameter	Sum of squares	D.o.F	Mean square	F	p
Length	8.56709E-08	1	8.56709E-08	17	0.0008
Fill ratio	2.81970E-07	1	2.81970E-07	55.96	0
Mass flow rate	1.62025E-07	1	1.62025E-07	32.16	0
Damping ratio	2.07600E-12	1	2.07600E-12	0	0.9841
Diameter	9.22071E-08	1	9.22071E-08	18.3	0.0006
Length*Fill	2.94316E-08	1	2.94316E-08	5.84	0.028
Length*Mass flow	1.15392E-08	1	1.15392E-08	2.29	0.1497
Length*Damping	2.66887E-13	1	2.66887E-13	0	0.9943
Length*Diameter	9.65534E-09	1	9.65534E-09	1.92	0.1853
Fill*Mass flow	8.80533E-09	1	8.80533E-09	1.75	0.2048
Fill*Damping	3.00460E-12	1	3.00460E-12	0	0.9808
Fill*Diameter	1.03678E-08	1	1.03678E-08	2.06	0.1707
Mass flow*Damping	2.27041E-12	1	2.27041E-12	0	0.9833
Mass flow*Diameter	6.02253E-12	1	6.02253E-12	0	0.9728
Damping*Diameter	2.14107E-12	1	2.14107E-12	0	0.9838
Error	8.06174E-08	16	5.03859E-09	-	-
Total	7.72305E-07	31	-	-	-

Table 6.6: ANOVA for maximum flex

Parameter	Sum of squares	D.o.F	Mean square	F	p
Length	4.83567E-08	1	4.83567E-08	29.26	0.0001
Fill ratio	3.44632E-07	1	3.44632E-07	208.51	0
Mass flow rate	3.42420E-09	1	3.42420E-09	2.07	0.1693
Damping ratio	8.51292E-14	1	8.51292E-14	0	0.9944
Diameter	1.67280E-08	1	1.67280E-08	10.12	0.0058
Length*Fill	9.27134E-09	1	9.27134E-09	5.61	0.0308
Length*Mass flow	7.88954E-09	1	7.88954E-09	4.77	0.0441
Length*Damping	3.24942E-15	1	3.24942E-15	0	0.9989
Length*Diameter	2.86295E-08	1	2.86295E-08	17.32	0.0007
Fill*Mass flow	1.61295E-10	1	1.61295E-10	0.1	0.7588
Fill*Damping	9.27508E-14	1	9.27508E-14	0	0.9941
Fill*Diameter	7.82003E-10	1	7.82003E-10	0.47	0.5014
Mass flow*Damping	1.13291E-16	1	1.13291E-16	0	0.9998
Mass flow*Diameter	4.96042E-09	1	4.96042E-09	3	0.1024
Damping*Diameter	1.68937E-14	1	1.68937E-14	0	0.9975
Error	2.74447E-08	16	1.65280E-09	-	-
Total	4.91280E-07	31	-	-	-

For the slosh motion, the interaction between parameters become more pronounced. The results for the total and maximum C.G. offset are given in Table 6.7 and Table 6.8. The damping has still no significant ($p = 0.2$) influence on the non-rigid motion, suggesting that the motion is forced by other effects. The length-diameter interaction is still very significant for the maximum C.G. offset ($p = 0.0129$). The interaction between fill and mass flow also causes significant changes ($p = 0.0001$). This is expected since both largely influence the available mass at a given point in time. It can be seen that all interactions with the diameter, except the damping, are significant. This is attributed to the analytical equations that are used to calculate the slosh mass, which are a function of diameter and fluid level.

Table 6.7: ANOVA for total C.G. offset

Parameter	Sum of squares	D.o.F	Mean square	F	p
Length	7.78385E-11	1	7.78385E-11	9.1	0.00082
Fill ratio	4.77117E-10	1	4.77117E-10	55.77	0
Mass flow rate	2.64925E-09	1	2.64925E-09	309.66	0
Damping ratio	5.15294E-12	1	5.15294E-12	0.6	0.449
Diameter	2.21037E-09	1	2.21037E-09	258.36	0
Length*Fill	1.68091E-13	1	1.68091E-13	0.02	0.8903
Length*Mass flow	3.07645E-11	1	3.07645E-11	3.6	0.0761
Length*Damping	1.48595E-13	1	1.48595E-13	0.02	0.8968
Length*Diameter	5.52850E-11	1	5.52850E-11	6.46	0.0217
Fill*Mass flow	1.18031E-10	1	1.18031E-10	13.8	0.0019
Fill*Damping	9.77766E-13	1	9.77766E-13	0.11	0.7397
Fill*Diameter	1.39046E-10	1	1.39046E-10	16.25	0.001
Mass flow*Damping	1.58224E-12	1	1.58224E-12	0.18	0.6729
Mass flow*Diameter	4.60876E-10	1	4.60876E-10	53.87	0
Damping*Diameter	8.69594E-13	1	8.69594E-13	0.1	0.754
Error	1.36883E-10	16	8.55522E-12	-	-
Total	6.36436E-09	31	-	-	-

Table 6.8: ANOVA for maximum C.G. offset

Parameter	Sum of squares	D.o.F	Mean square	F	p
Length	7.38965E-12	1	7.38965E-12	25.79	0.0001
Fill ratio	1.39960E-10	1	1.39960E-10	488.55	0
Mass flow rate	1.02663E-09	1	1.02663E-09	3583.61	0
Damping ratio	5.11082E-13	1	5.11082E-13	1.78	0.2003
Diameter	1.36064E-09	1	1.36064E-09	4749.52	0
Length*Fill	5.92633E-13	1	5.92633E-13	2.07	0.1696
Length*Mass flow	2.95539E-13	1	2.95539E-13	1.03	0.3249
Length*Damping	2.98568E-14	1	2.98568E-14	0.1	0.751
Length*Diameter	2.24249E-12	1	2.24249E-12	7.83	0.0129
Fill*Mass flow	8.08862E-12	1	8.08862E-12	28.23	0.0001
Fill*Damping	3.33740E-13	1	3.33740E-13	1.16	0.2964
Fill*Diameter	1.34309E-11	1	1.34309E-11	46.88	0
Mass flow*Damping	4.87697E-15	1	4.87697E-15	0.02	0.8978
Mass flow*Diameter	9.16553E-11	1	9.16553E-11	319.94	0
Damping*Diameter	5.58018E-15	1	5.58018E-15	0.02	0.8907
Error	4.58369E-12	16	2.86480E-13	-	-
Total	2.65640E-09	31	-	-	-

6.1.3. Interactions

Significance of certain parameters, or interaction between parameters, only provides half the information. Further discrimination of interaction can be obtained by performing multiple one-way ANOVA's for certain significant parameters. It was found that the length and diameter ratio has a significant influence on the maximum flex, and the maximum and total C.G. offset. The analysis for the flexibility is shown in Figure 6.5.

It can be seen that the group that contains the larger length and diameter is significantly different from the rest.
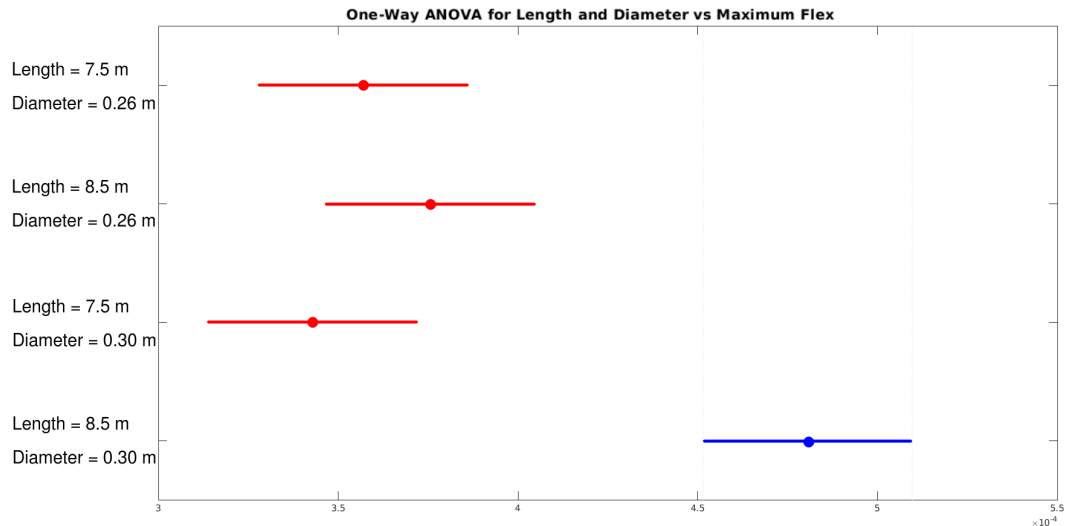
Figure 6.5: One-way ANOVA for Length and Diameter on maximum flex. Three groups (red) have population marginal means significantly different from Length=8.5m and Diameter=0.3m (blue)

The maximum deflection is the lowest of all four scenario's and the natural frequency is average compared to the other values. This effect is further discussed in Section 6.2.

The effects of the diameter and length are more pronounced for the C.G. offset. It can be clearly seen that the larger diameters have a significant influence on the total and maximum C.G. offset, or mass-normalised sloshing motion. The maximum and total values are several orders higher for the variation of parameters that contains the larger diameter. Vehicle length seems to have a marginal influence when the diameter is small enough, but a significant influence ($p = 0.0059$) when the diameter increases. This effect also provides further insight to the maximum flex, as the coupling of flexibility and sloshing likely caused an increase in the maximum flexibility of the vehicle.

From these results we can conclude that length, diameter and mass flow rate are key parameters for non-rigid body effects. Flexibility strongly depends on the length-diameter interaction or slenderness of the vehicle. High thrust to weight ratios also influence both the flexibility and sloshing of the vehicle.

6.2. Sensitivity analysis for key design parameters

In Section 6.1.3, the effects of increasing or decreasing certain parameters on the non-rigid body effects are analysed. However, it remains unclear when non-rigidity becomes destabilising. More data is required to determine for which analysis parameter values non-rigid body effects become most prevalent. Using the same launch vehicle model as Section 6.1, two parameters are considered one by one. For a fixed length, mass flow rate and fill ratio, the diameter is incrementally increased.

The simulation is run for 12 seconds and the non-rigid parameters are saved. The diameter is ranged from 0.2 to 0.5 m. This allows to determine the severity of the non-rigid body effects as a function of Length over Diameter (L/D) ratio. For a fixed diameter, length and fill-ratio, the mass flow rate is altered between 10 and 30 kg/s. The aerodynamic coefficients are assumed constant.

First, the diameter is considered. The diameter not only chances the value for the total propellant in the tank but also the natural frequency and maximum deflection. Therefore, 4 different ANSYS models are used to determine the trend line of the required parameters. The 4 data points are 0.1, 0.2, 0.3 and 0.4 m. The diameter 0.5 m is also measured in ANSYS and used as verification for the equation.
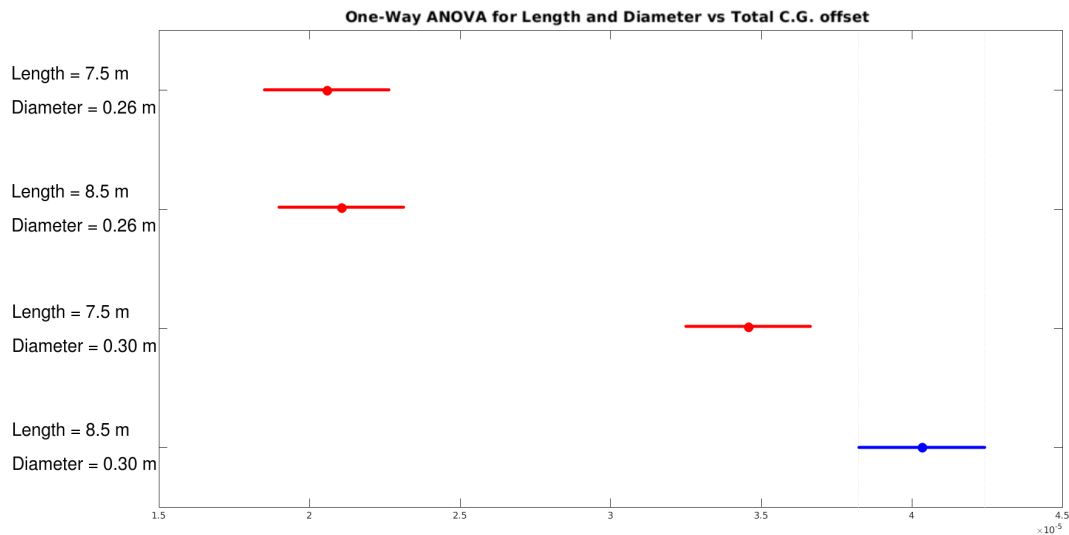
Figure 6.6: One-way ANOVA for Length and Diameter on total C.G. offset. Three groups (red) have population marginal means significantly different from Length=8.5m and Diameter=0.3m (blue)
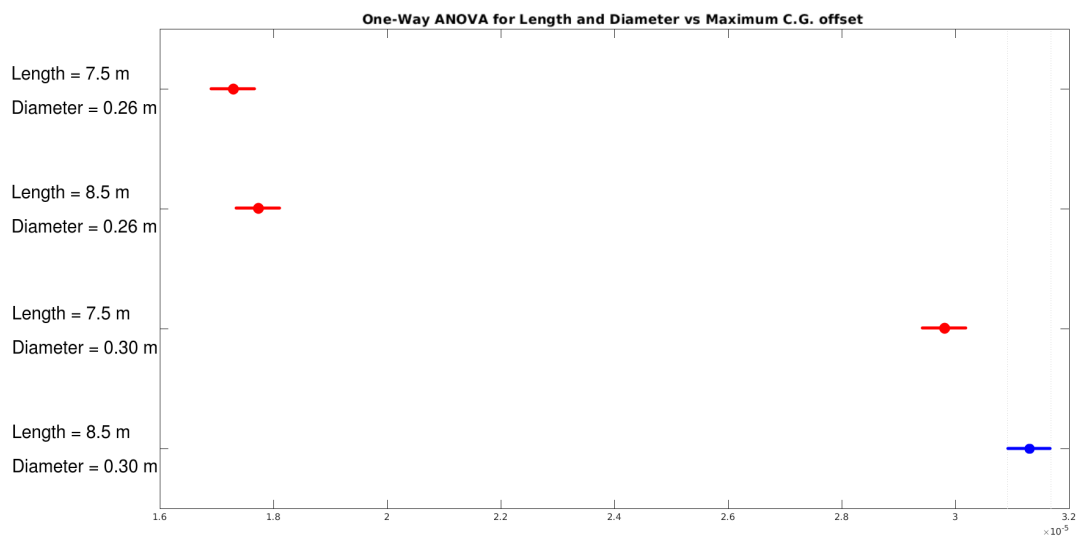
Figure 6.7: One-way ANOVA for Length and Diameter on maximum C.G. offset. Three groups (red) have population marginal means significantly different from Length=8.5m and Diameter=0.3m (blue)

Table 6.9: Natural frequency and mass-normalized maximum deflection for different diameters. Length is fixed at 8.5 m

Diameter	Real Freq	Est Freq	Dif [%]	Real Def	Est Def	Dif[%]
0.1	15.00	14.80	1.30	0.47	0.47	-0.09
0.2	23.26	23.48	-0.93	0.33	0.33	0.00
0.3	32.00	32.15	-0.48	0.27	0.27	-0.02
0.4	41.00	40.83	0.42	0.23	0.23	-0.07
0.5	50.71	49.50	2.39	0.20	0.20	-0.25
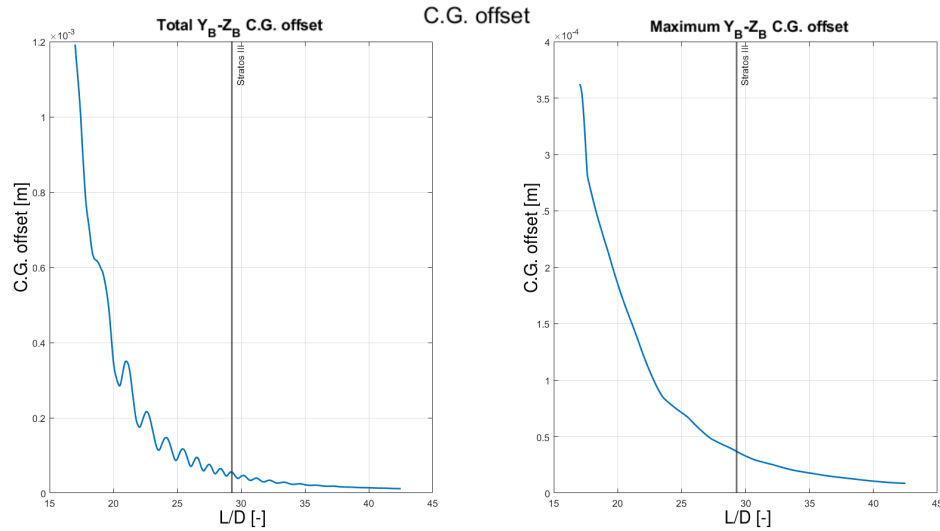
Figure 6.8: Maximum and total offset in C.G. for a given L/D ratio. Vertical line indicates L/D of the Stratos III rocket

From the four data points, it was found that the natural frequency for a fixed length can be described with an accuracy of $\pm 2\%$ as

$$\omega_n = 86.738D + 6.131 \quad ; \quad 0.1 \leq D \leq 0.5 \tag{6.2}$$

The maximum mass-normalized flex can be calculated with an accuracy of $\pm 0.2\%$ with

$$\Phi = 0.1438D^{-0.511} \quad ; \quad 0.1 \leq D \leq 0.5 \tag{6.3}$$

The results from the 4 runs are summarized in Table 6.9. This includes the differences between the estimated value from Equation (6.2) and Equation (6.3).

A more detailed analysis can be performed on the effect of the diameter on the non-rigid parameters of the model. The model is run for 12 seconds, increasing the diameter each run with 1 mm. Similarly to Section 6.1, the non-rigid parameters can be plotted based on the change in diameter. For the flexibility, it was found in the previous section that the length-diameter interaction plays a significant role in the maximum flexibility of the vehicle. The non-rigid parameters are plotted with respect to the Length over Diameter (L/D) ratio. The variation in maximum and total C.G. are given in Figure 6.8. The variation in maximum and total flexibility are given in Figure 6.9.

In Figure 6.8, the effects of sloshing become exponentially worse for smaller L/D ratios. For small L/D ratios, the diameter becomes significantly larger. The slosh mass is proportional to the square of the diameter. This means that the total and maximum offset will significantly increase for larger diameters. Figure 6.9 shows a different result, where the total and maximum mode performance reach a maximum at an L/D ratio of approximately 27, decreasing again when the L/D increases further. This seems counter-intuitive, since a more slender beam will have a larger deflection at the eigenfrequency as seen in Table 6.9. Therefore, it is likely that the combination of slosh, eigenfrequency and aerodynamic forces causes resonances in the vehicle, significantly increasing its flexible motion.

Stratos III shows to be close to the worst-case value of L/D for the slosh-flex-aero interaction. This further validates the claim that Stratos III likely failed due to non-rigid body effects as stated in Chapter 5. It would therefore be recommended for future Stratos missions to analyse slosh-flex-aero interaction for different vehicle configurations. Increasing the fin size increases static margin, changing the aerodynamic properties of the vehicle. As a result, the maximum flexibility can potentially occur at a different L/D ratio. Slosh dampers showed to have a minimum influence within the considered slosh regime for slender vehicles. Stiffening connections will change the natural frequency and therefore decrease the flexibility of the vehicle. Finally, active control systems can be considered. In Section 7.2.3, these mitigation strategies are discussed in more detail.
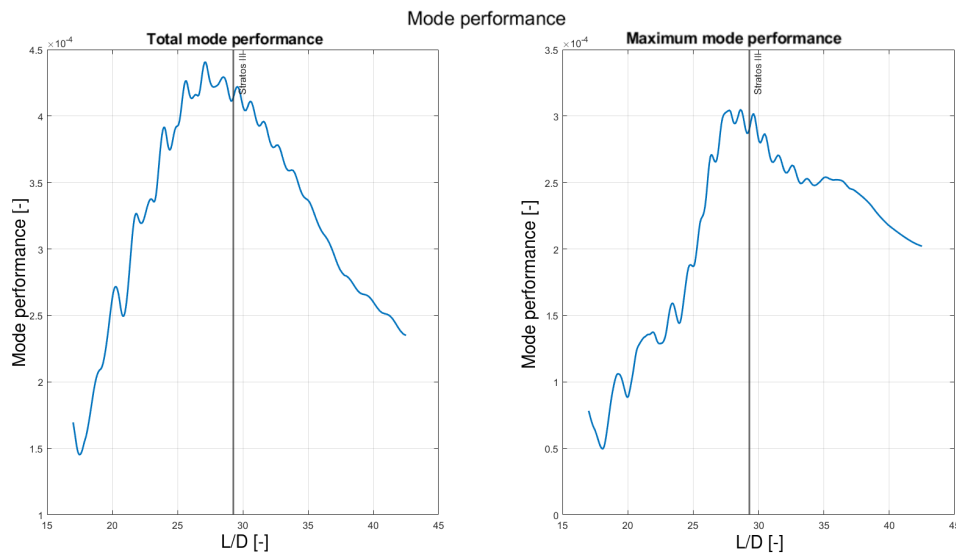
Figure 6.9: Maximum and total flexibility for a given L/D ratio. Vertical line indicates L/D of the Stratos III rocket

This effect is further investigated by analysing the data from specific L/D ratios. The slosh (pitch) angle, body (pitch) angle and mode performance are shown for an L/D of 21.25, 28.3 and 42.5. This corresponds to a diameter of 0.2, 0.3 and 0.4 m respectively. The results are shown in Figure 6.10 to Figure 6.12. All axes are equal to illustrate the difference. Although the slosh and body angle are about twice as high for an L/D of 21.25, the frequency is significantly lower, resulting in lower (peak) flexibility. The opposite is the case for the high L/D of 42.5. The damping ratios of the fluids seem different for the three plots. This is because the damping coefficient is chosen as a scalar value that determines the damping based on the current velocity of the fluid. Since the forces acting on a lighter slosh mass are smaller, the damping is more significant, resulting in a larger damping ratio. Although the ANOVA showed that damping has no significant effect on any of the non-rigid body effects, the same three values are considered when no damping is applied to the slosh mass. The results are shown in Figure 6.13 to Figure 6.15. Again, all axes are equal to illustrate the difference.

The same pattern can be observed for the undamped scenario. It also shows the interaction between the flexibility and the slosh angle. Although the model is undamped, the slosh angle loses approximately 60% of its amplitude for an L/D of 28.3. Simultaneously, the flexing strongly increases. Based on the sensitivity data, it can be observed that orbital launch vehicles such as the Horizon 2020 SMILE will experience a very small destabilising effect due to flexibility. With an L/D of 16.6 [6], the vehicle is expected to suffer mainly from sloshing effects.

The mass flow rate is directly coupled to the thrust, meaning it is indirectly coupled to the flexibility. The mass flow rate is directly coupled to the slosh mass over time. From Table 6.5 to Table 6.8, it was found that the mass flow rate has a significant influence on the total and maximum C.G. offset. It also has a significant influence on the total flex of the vehicle. It has no significant effect on the maximum flex. The mass flow rate is varied linearly with 0.1 kg/s increments and simulated for 12 seconds. An L/D of 30 is considered. The results can be seen in Figure 6.16 and Figure 6.17.
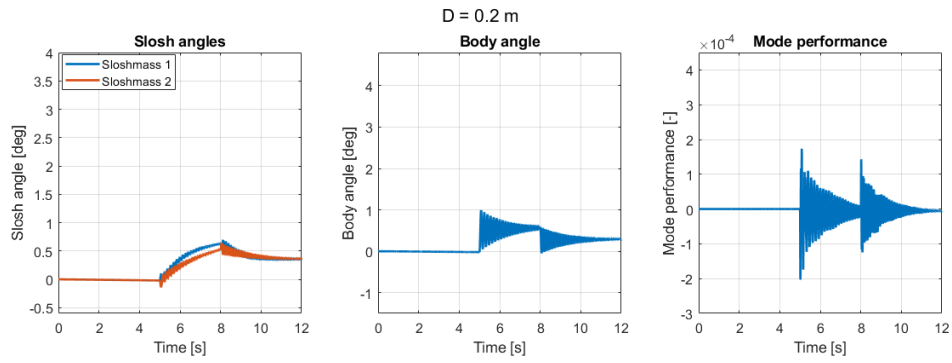
Figure 6.10: Slosh angles, body angle and mode performance for D=0.2 (L/D=42.5)
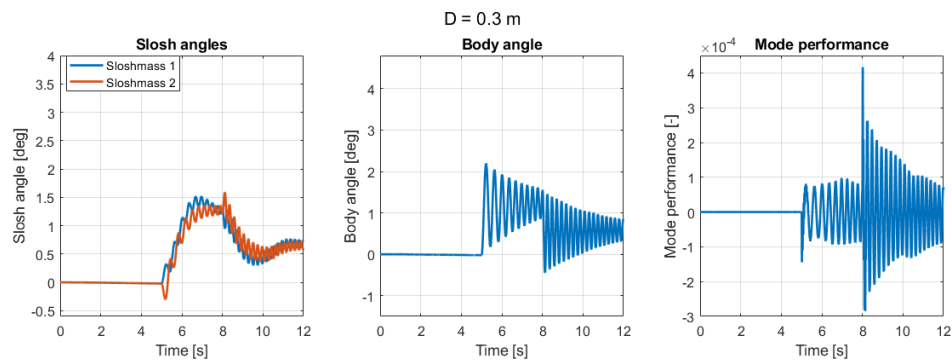
Figure 6.11: Slosh angles, body angle and mode performance for D=0.3 (L/D=28.3)
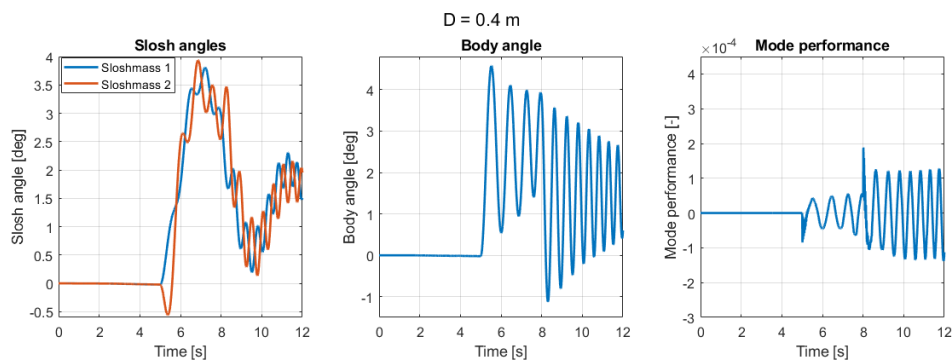
Figure 6.12: Slosh angles, body angle and mode performance for D=0.4 (L/D=21.25)
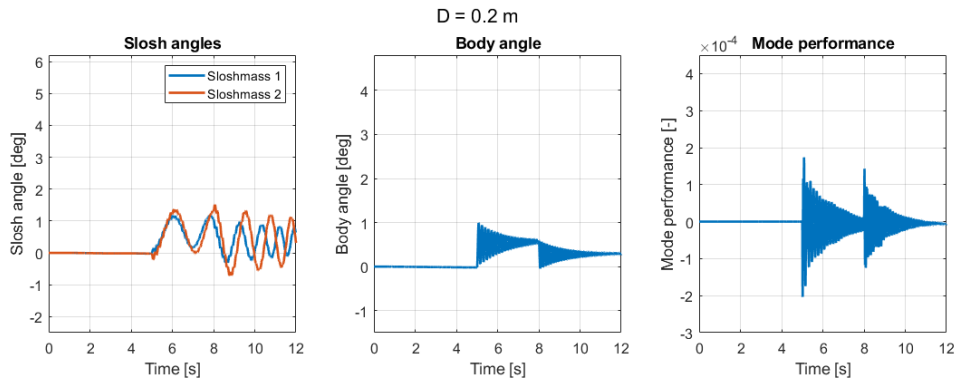
Figure 6.13: Undamped slosh angles, body angle and mode performance for D=0.2 (L/D=42.5)
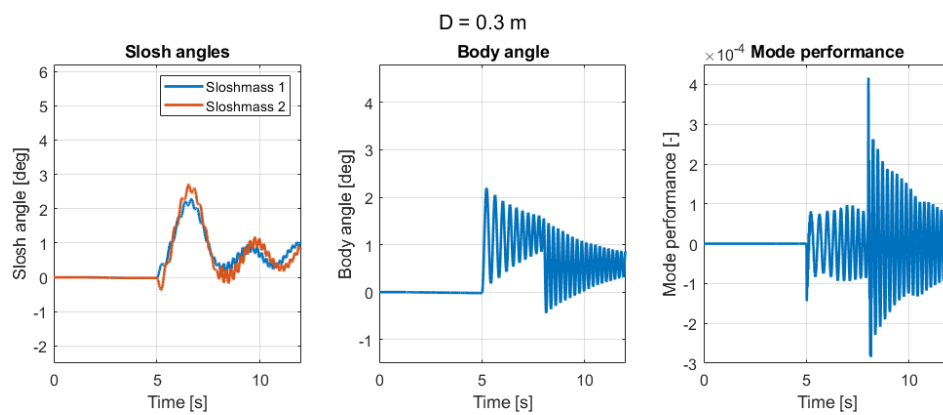
Figure 6.14: Undamped slosh angles, body angle and mode performance for D=0.3 (L/D=28.3)
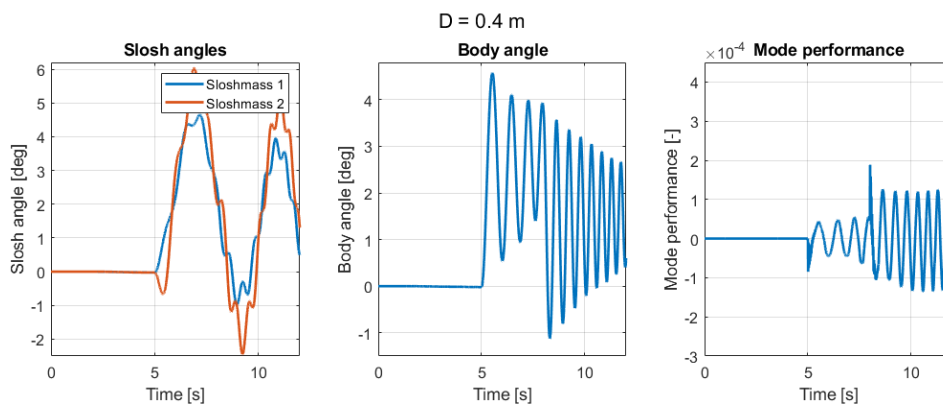
Figure 6.15: Undamped slosh angles, body angle and mode performance for D=0.4 (L/D=21.25)

The mass flow rate is converted to (initial) thrust to weight to further generalise the results. The observations from the ANOVA are confirmed here. The initial thrust to weight has no clear effect on the maximum flex of the vehicle. It does have an effect on the total flex of the vehicle. A larger mass flow rate simply means that there is less time for the slosh mass to slosh. As a result, the C.G. offset decreases for an increasing thrust to weight ratio. Again, Stratos III shows to be close to the worst case thrust to weight ratio for flexibility.
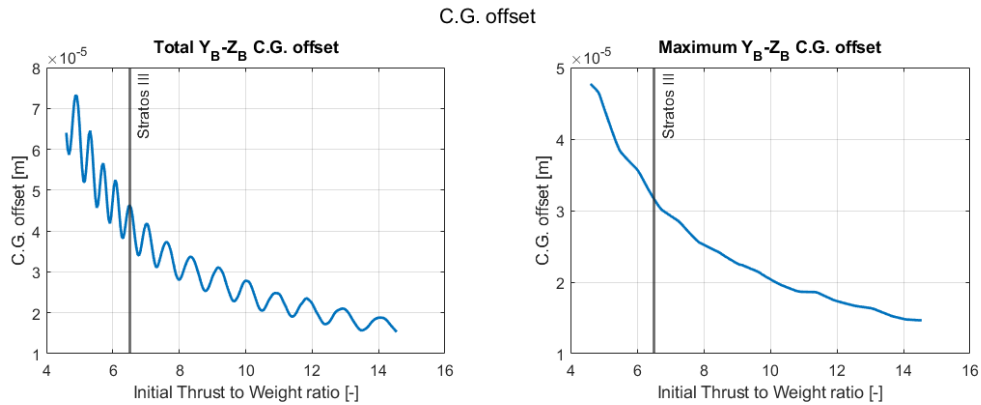
Figure 6.16: Maximum and total change in C.G. for different Thrust to Weight ratios
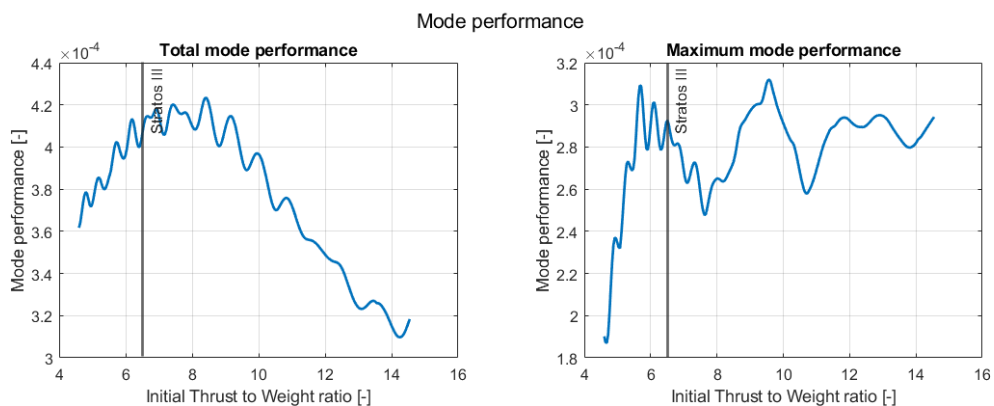
Figure 6.17: Maximum and total change in flex for different Thrust to Weight ratios

6.3. Controller design for non-rigid body models

Based on the data from Section 6.2, it can be assumed that flexibility is negligible for small-sat launch vehicles such as Horizon 2020 SMILE. However, sloshing still poses a challenge. The large diameter will result in large slosh masses and therefore larger variations in body angles. To see if this effect can be destabilising for small-sat launch vehicles, the endo-atmospheric phase of the SMILE launcher is considered. This includes first stage separation. In this section, a PID controller is designed around the rigid body equivalent of the SMILE launcher for the first 60 seconds of the flight. The equations of motion for the rigid body are implemented using the Matlab *Custom Variable Mass (ECEF)* block. The same environmental model is used for both simulators. The gains for the PID controller are placed in the non-rigid body model without changing any values. The cumulative control input (error) is measured to determine the effectiveness of the controller.

Maximum dynamic pressure occurs at 28.8 seconds, meaning that any destabilisation due to slosh-flex-aero interaction is expected to occur around this time. The first stage burns out at 43 seconds. The second stage ignites at 45 seconds. For the first 2 seconds of the flight and for the staging event, the controller is set to zero. The staging can have a large influence on the slosh mass due to the low gravity environment. In this environment, the slosh mass can move much more freely, potentially destabilising the vehicle when the second stage engine is turned on. An under-damped slosh mass is considered. The COESA atmosphere model is used, combined with the Horizontal Wind Model. Spherical Harmonics with degree and order 4 is used for the gravity model. The controller is designed around the rigid body model. Both a single set of gains, as well as gain-scheduling is considered. The gains are determined using the Matlab PID tuner.

Figure 6.18: Body attitude over time

6.3.1. Rigid body based controllers

Three scenarios are considered for this analysis. First, an uncontrolled model is considered to determine if a control system is required for an aerodynamically stable vehicle with 6 slosh masses. Next, a single set of PID gains is determined and used on the non-rigid body model with under-damped slosh masses. Finally, a gain-scheduled controller is created. For this 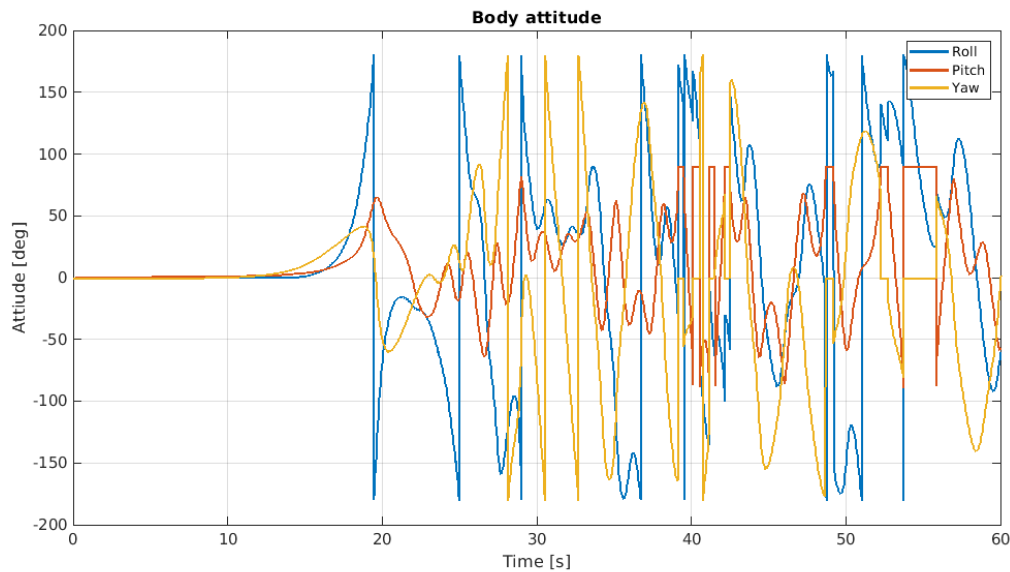simplified analysis, the vehicle is instructed to fly up while maintaining a zero body rate. A rate controller is used to avoid anomalies since the conversion from DCM to Euler angles around the starting position of 90 degrees can cause large jumps in the calculated angles. If the controller is able to keep the rate at zero, the euler angles will be constant.

Uncontrolled non-rigid body

The SMILE vehicle that is considered for this analysis is a three-stage liquid vehicle. It is aerodynamically stable ($C_M < 0$). The vehicle flies uncontrolled for 60 seconds. The body attitude can be seen in Figure 6.18. The dynamic pressure over time can be seen in Figure 6.19.

It can be seen that the vehicle experiences significant destabilisation near the point of maximum dynamic pressure. A controller is required to stabilise the vehicle during flight, even if it is aerodynamically stable.

Single gain PID

To control the vehicle, a PID controller with 1 set of gains is designed around the point of maximum dynamic pressure. From Figure 6.19, it can be seen that this occurs at 28.8 seconds. Using the matlab PID tuner block, the rigid-body model is linearised around this time. The actuators that control the engine deflection angle are modelled as a linear second order actuator. The parameters for the actuators are chosen equivalent to Mooij [16]. The natural frequency of the actuator is 15 rad/s with a damping ratio of 0.7.

The estimated bandwidth and phase margin are 75 rad/s and 35 deg respectively. This results in the following gains

$$K_p = 8.98 \quad ; \quad K_i = 3.92 \quad ; \quad K_d = 4.57$$

Since the vehicle is axi-symmetric, the gains are assumed the same for the pitch and yaw direction. The controller error for the rigid and non-rigid body can be seen in Figure 6.20. This figure shows the instantaneous error during the 60 second simulation. The insert shows a zoomed-in plot of the first 40 seconds to show the error before the staging event. The staging event itself can be clearly seen in the large error spike between 43 and 45 seconds. Before the staging event, the error is close to zero in both the rigid and non-rigid body model.

The cumulative error can be seen in Figure 6.21. The cumulative error is the integral of the absolute signal represented in Figure 6.20 and gives a good indication of the controller performance.
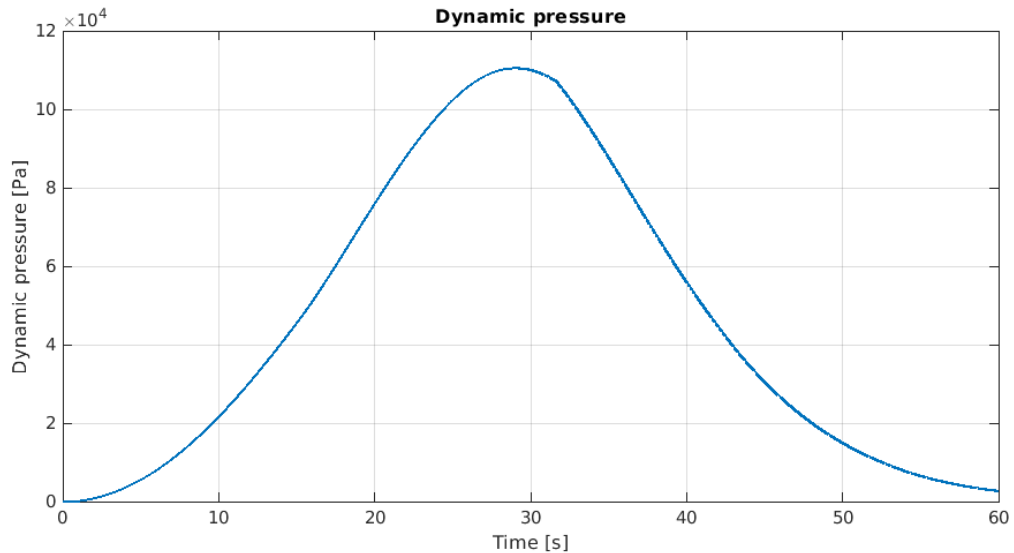
Figure 6.19: Dynamic pressure over time

The error shows similar behaviour for both models. During first stage separation, the error significantly increases. This is expected since no control input is given during this time. After second stage ignition at 45 seconds, an oscillation occurs in the controller. This is attributed to a high derivative gain for the controller and can be solved with gain-scheduling. The non-rigid body shows this oscillation earlier than the rigid body. The cumulative yaw error has a negligible difference between the two models. The pitch error is slightly higher in favour of the non-rigid body model. The slosh mass can damp sudden changes in movement due to the slosh-rigid interaction. From these results, it can be determined that a simple rigid body controller is able to effectively control a non-rigid body model.

Gain-scheduled PID
To remove the oscillations later in flight, gain-scheduling is considered. The scheduling parameter needs to be monotonically increasing or decreasing to ensure that lookup tables can be used. This means that dynamic pressure can't be used to schedule the gains.
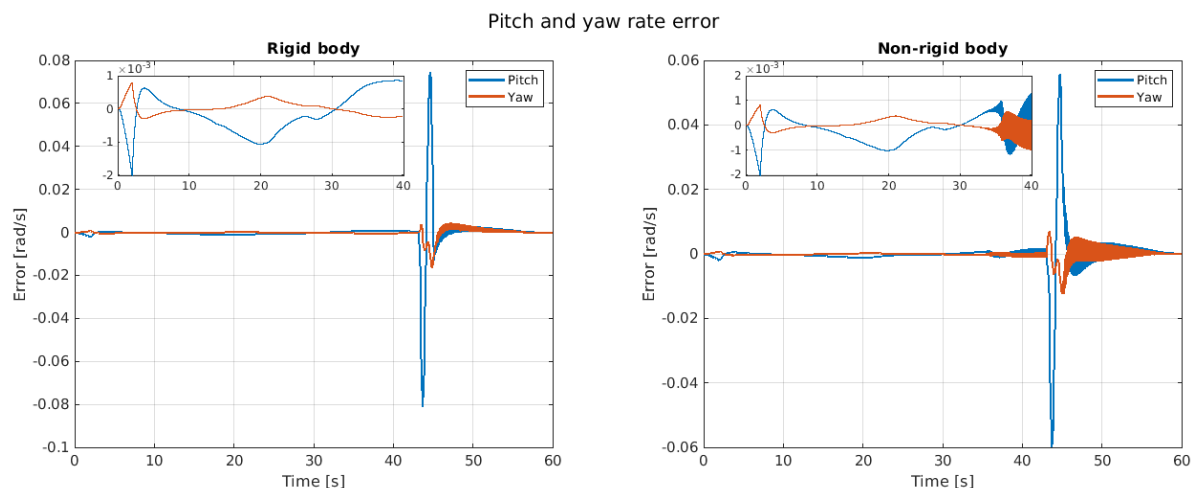
Figure 6.20: Comparison between rigid and non-rigid body body rates (control error)
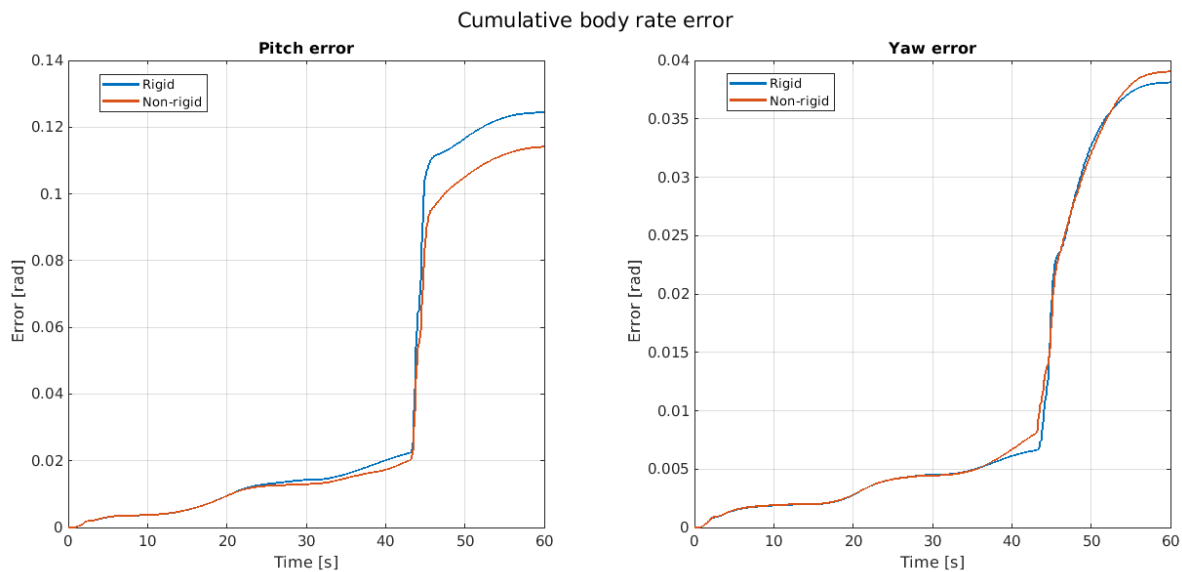
Figure 6.21: Comparison between rigid and non-rigid body cumulative control error

The control angle and inertia of the vehicle directly influences the rigid body motion. Therefore the mass is considered as a scheduling parameter. This value is monotonically decreasing and can take into account staging events if interpolation is performed appropriately.

Using the Matlab tuner block, a stabilising set of gains can be found for given vehicle masses according to Table 6.10.

The derivative gain is strongly decreased after the point of maximum dynamic pressure to reduce the observed oscillations from Figure 6.20. Since a filtered derivative is used, the value for N is increased to increase the filter derivative accuracy. The resulting rate errors can be seen in Figure 6.22. It can be seen that the error spike during stage separation is significantly higher for the non-rigid body. Before stage separation, the error is very close to zero. Again, a zoomed-in view of the first 40 seconds is given in the figure as well. In this section of the flight, the vehicles show an almost identical behaviour.

The cumulative control error can be seen in Figure 6.23. It can be clearly seen that with this set of gains, the error significantly increases for the non-rigid body model compared to the rigid body model. Up to 20 seconds, the error is almost identical, diverging just after stage separation. From this behaviour we can conclude that for nominal flight trajectories, the rigid body controller is able to stabilise the non-rigid body. However, when the controller is turned off for stage separation, the more complex non-rigid body model destabilises faster, resulting in larger errors.

From Figure 6.21 it can be observed that the pitch and yaw error are 0.125 and 0.038 rad for the rigid body. The pitch and yaw error from Figure 6.23 are 0.042 and 0.06 rad. With gain-scheduling, the error significantly improves in the pitch direction and worsens in the yaw direction. More yaw control effort is required to stabilise the vehicle after first stage separation.

For the non-rigid body, the errors for the pitch and yaw rate in Figure 6.21 are 0.115 and 0.039 rad. In Figure 6.23, these are 0.165 and 0.15 rad. Both directions show a larger error during stage separation. Because of the lower gains, the model responds more robustly to the acquired error during stage separation. This results in a slower response and larger cumulative error.

In both the rigid and non-rigid model it can be observed that no oscillation occurs after stage separation. A more aggressive set of gains can be chosen to decrease the cumulative error, at the cost of more oscillations.

Even though the error increases for gain-scheduling, oscillations that were observed for the single set of gains can be successfully removed by designing the PID controller around the rigid body plant model. The control algorithm is able to stabilise both the rigid and non-rigid body model with the same set of gains.

Table 6.10: Used gains for gain-scheduled PID controller

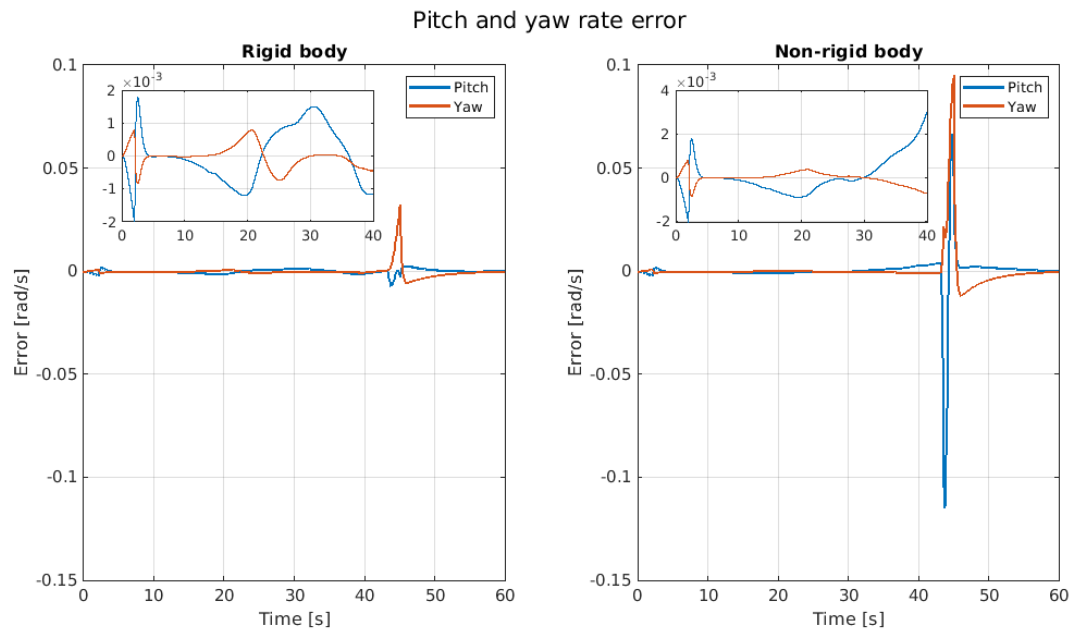| Time [s]	Mass [kg]	K_p	K_i	K_d	N
3	10165	3.63	5.46	0.58	500
15	8389	5.26	4.74	3.54	500
28.8	6347	8.98	3.92	4.57	500
40	4689	2.30	0.58	0.41	1900
46	1867	1.39	0.36	0.23	2100

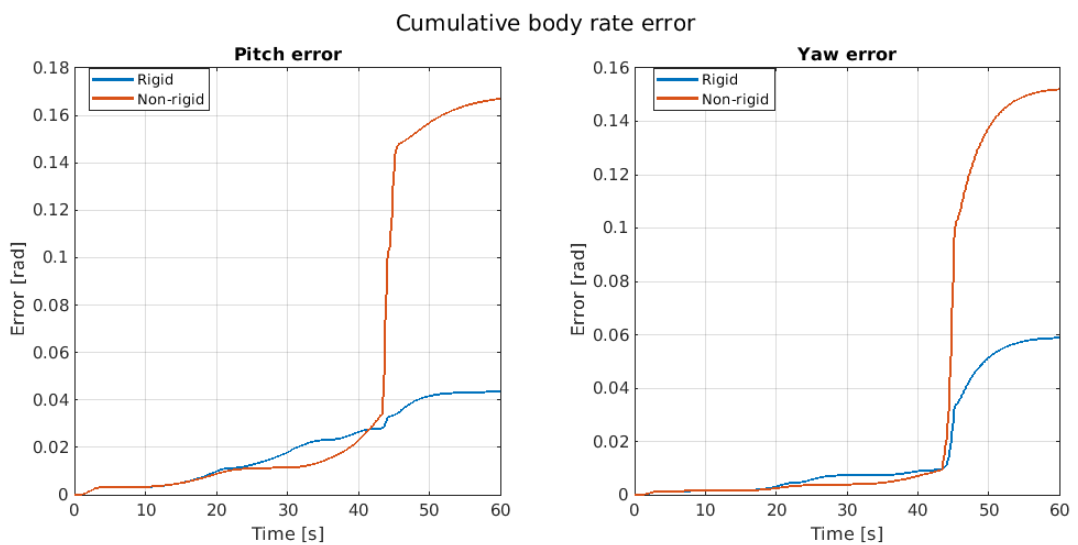Figure 6.22: Comparison between rigid and non-rigid body body rates (control error)

Figure 6.23: Comparison between rigid and non-rigid body cumulative control error

6.3.2. Non-rigid body controller conclusion

It can be seen that, for a small-sat launch vehicle such as SMILE or Electron, non-rigid body effects cause a disturbance to the model. Even when the model is aerodynamically stable, the vehicle can still destabilise during flight due to sloshing effects. Nonetheless, simple PID control algorithms that are designed for a rigid body model are still able to stabilise the non-rigid body model at the cost of a higher controller error in some situations.

For a single set of gains, oscillations occur for both models around stage separation. This oscillation occurs earlier in the non-rigid body model. These oscillations can successfully be avoided in both models by designing a gain-scheduled PID controller around the rigid body model at the cost of a larger cumulative control error for the non-rigid body model.

PID control is not an optimal control algorithm. No optimal set of gains exists for a given launch vehicle. Other control algorithms, such as H_∞, find an optimal set of gains for a chosen weighting function. Therefore it is expected that optimal control algorithms such as H_∞ can further decrease the control error. Alternatively, a non-linear controller such as (incremental) non-linear dynamic inversion can be used. These non-linear controllers show less controller error for elastic launch vehicles [16]. Incremental non-linear dynamic inversion requires knowledge of the equations of motion of the vehicle. This research focusses on the effect of rigid body controllers on non-rigid body models. It is expected that for this scenario, non-linear controllers that require knowledge of the state equations are at an inherent disadvantage. Given the different equations of motion, the non-linear controller will likely behave significantly different between the two models. If there is sufficient knowledge of the system (rigid or non-rigid), it is recommended to design a non-linear controller around this system. However, if the equations of motion are unknown, it can be shown that simple linear rigid-body controller can effectively control small-sat launch vehicles with average slenderness ratios.

6.4. Discussion on the results

In this chapter, an analysis was performed on the necessity of non-rigid body models. In Section 6.1, it was found that vehicle length, diameter, mass flow rate and fill ratio have a significant influence on the non-rigid body effects. The length over diameter (L/D) ratio showed to be an important parameter when considering the use of non-rigid body models. In Section 6.2, an L/D of 27 was found to result in a maximum destabilising effect due to the interaction between sloshing, flexibility and aerodynamics for the Stratos III aerodynamic coefficients. This lies close to the L/D ratio of 29.2 for Stratos III, which is speculated to have failed due to non-rigid body effects. Sloshing itself is negligible for L/D ratios above 20, but can still be destabilising for larger values due to this slosh-flex-aero interaction. Flexibility itself is negligible for L/D ratios below 20. This means that small-sat launch vehicles generally do not require the use of non-rigid body models to estimate the flight path. This is confirmed in Section 6.3, where a rigid body PID controller is directly implemented in the non-rigid body model. The controller still was able to successfully stabilise the vehicle at the cost of a slightly larger controller error. Oscillations that occured in both models, although at different times, were removed by designing a rigid body gain-scheduled controller. This resulted in a larger error for the non-rigid body model. Further tuning or other controller algorithms are expected to decrease this error.

<div style="text-align: right; font-size: 3em;">7</div>

Conclusion and recommendations

In previous research, the necessity of non-rigid body simulators was stated to be a requirement for long, slender bodies. This suggests that there is a slenderness ratio from which non-rigid body effects become destabilising. In this research, a length-over-diameter ratio was found from which non-rigid body effects become most apparent. This research aimed to examine the necessity of non-rigid body models for small-sat launch vehicles such as the Horizon 2020 SMILE.

In this final chapter, the results from the previous chapters are concluded. In Section 7.1, the research conclusions are presented. In Section 7.2, recommendations for future research are given.

7.1. Research conclusions

Three linearly independent motions are coupled using a constraint matrix to simulate a non-rigid launch vehicle. These are the rigid body motion, sloshing motion and flexibility motion. The flexibility motion is modelled using the method of assumed modes. The sloshing motion is modelled by assuming that the slosh mass behaves like a pendulum. To couple the different motions, a constraint matrix is used. This modular matrix allows fixing the attachment point of the slosh mass to the *deflected* state of the vehicle. As a result, the slosh mass and flexibility motion are directly coupled by this constraint. This means that the slosh motion will cause flexibility in the vehicle and vice versa. Since the matrix is modular, the model can be extended to allow for any number of slosh masses. If the constraints are rewritten, other rigid bodies such as stages could also be added to the system. Additionally, a detailed environment model is created. Different models can be chosen to simulate the Earth shape, gravity, atmosphere, wind and aerodynamics depending on the user requirements. The model is run using a fixed-step integrator with a time step between 1E-2 and 1E-3 seconds. These settings allow the model to run faster than real-time. This means that the model can be used in embedded systems for future NLR customers.

For the launch vehicle, a custom mass model is created. In this research, the custom mass model makes use of analytical equations to estimate the rigid body and slosh mass parameters at any moment in time. This means that the slosh mass parameters can vary, depending on the state of the vehicle. Since analytical equations are used, the difference compared to the analytical solutions is negligible. Using simplified scenarios, both the rigid body and slosh mass constraint were verified with analytical equations. This resulted in a difference of less than 0.1%. To further verify the equations of motion, the model energy was determined. Using non-quiescent starting conditions with no external forces acting on the vehicle except gravity, it was found that the energy of the system remained constant. Since the energy of the system is conserved, it provides strong evidence that the equations of motion are implemented correctly.

The flight data from the Stratos III launch vehicle was obtained and compared to the simulated non-rigid body model data. The model was adapted to a single-stage with 1 slosh mass. Mass parameters were determined using the custom mass model and compared to the available data from the Stratos III payload manual. This vehicle is especially interesting since it is speculated that this sounding rocket failed due to non-rigid body effects. Different settings for the wind and oxidiser to fuel ratio were used to analyse the anomaly that resulted in the failure of Stratos III. It was found that slosh motion can result in destabilisation when the vehicle experiences a sudden decrease in acceleration. For Stratos III, such a decrease in acceleration could have occurred when the vehicle transitioned from the liquid to the gaseous burn phase. Due to the rotational velocity of the vehicle, it is likely that some liquid propellant still resided in the oxidiser tank.

Table 7.1: L/D ratios of past and current launch vehicles

Vehicle	Developer	Length [m]	Diameter [m]	L/D [-]	Source
Falcon 9	SpaceX	70	3.7	18.9	[25]
Electron	Rocket Lab	18	1.2	15	[23]
Ariane V	ArianeGroup	50.5	5.4	9.35	[4]
Soyuz-2	Progress Rocket Space Centre	46.2	2.95	15.7	[5]
Saturn V	NASA	110	10.1	10.9	[18]

This propellant is free to slosh around in a microgravity environment. This effect is similar during staging events for large launch vehicles. The non-rigid body model was also compared to an equivalent rigid body model. The destabilisation that occurred could not be observed when rigid body equations of motion were used. The non-rigid body model was able to accurately estimate the acceleration and Mach number for most of the flight. It did show inconsistencies in the body rates later in the flight. The roll rate of Stratos III was significantly higher than simulated.

Using ANOVA, it was found that the length, diameter, mass flow rate and fill ratio are launch vehicle design parameters that significantly influence non-rigid body effects such as sloshing and flexibility. The length-diameter interaction is also significant for flexibility. This is in line with current research, which states that long, slender bodies are more susceptible to non-rigid body effects. In previous research, no slenderness ratios were presented from which non-rigid body effects become apparent. In this research, a slenderness ratio was found from which flexibility and sloshing effects become prominent. Based on a sensitivity analysis over a range of vehicle parameters, it is recommended for length over diameter (L/D) ratios above 20 to consider the use of non-rigid body models. From this ratio, the maximum and total flexibility strongly increase. A maximum deflection sensitivity was found for an L/D of 27, decreasing again for even larger ratios. This peak was attributed to an interaction between the limited sloshing motion, vehicle flexibility and aerodynamics.

With this sensitivity analysis, it was also determined that for L/D ratios below 20, flexibility is negligible and sloshing becomes the main perturbing factor. Most launch vehicles have an L/D ratio which is well below this value as shown in Table 7.1. This suggests modelling flexibility is not required for accurate GNC models of small-sat launch vehicles. The slosh motion still perturbs the vehicle during flight. It was found that even for passively stable launch vehicles, the slosh motion destabilises the vehicle when dynamic pressure increases. A simple PID controller was designed to stabilise this vehicle. The controller was designed using the Matlab PID tuner block. The gains were tuned using a rigid body model with equivalent mass, inertia and environment to the non-rigid body model. It was found that a PID controller that is designed using a rigid body model is still able to stabilise the non-rigid vehicle during flight. It was found that the error of the rigid and non-rigid body model was equivalent and both negligible for the first 43 seconds of the flight. This is well after the point of maximum dynamic pressure which occurred at 28 seconds. During the staging event, 2 seconds of microgravity result in a tumbling slosh mass which destabilises the non-rigid body. Regardless, the rigid body controller was still able to correct this after second stage ignition. Oscillations occurred in both the rigid and non-rigid body model when a single set of gains was used. These oscillations occurred earlier in the non-rigid body model. For both models, the oscillations were removed by introducing gain scheduling. A set of gains was scheduled based on the vehicle mass. By strongly decreasing the derivative gain at the point of stage separation, the oscillation could be avoided. This did result in larger errors for the non-rigid body model, meaning more tuning or better control algorithms might be required to increase the performance.

To summarise, this means that non-rigid body models are not required to keep the SMILE small-sat launch vehicle stable during ascent. With the L/D ratio of the SMILE launch vehicle, which is comparable to most other launch vehicles, the flexibility is negligible. Sloshing effects can be accounted for by simple linear controllers designed completely around rigid body models. The launch vehicle parameters that play an important role are the length, diameter, mass flow rate and fill ratio. Especially the length over diameter and thrust to weight ratio plays an important role. From an L/D 20, it is recommended to use non-rigid body models.

7.2. Recommendations for future improvements

In this section, several recommendations regarding this research are given. The recommendations are split into three sections. Potential Simulink model improvements are given in Section 7.2.1. In Section 7.2.2, recommendations to improve this research are given. Finally, Section 7.2.3 presents the recommendations for future research.

7.2.1. Model improvements

Although the model takes into consideration a lot of different effects, some of the assumptions used for this model require further investigation.

The aerodynamics model is equivalent to that of a rigid body model. In reality, flexibility will likely result in local angles of attack that are larger than the angle of attack that the vehicle experiences in this model. A node-wise lift model could improve this model at the cost of more computational time. The required equations for such a model are presented in Section 2.2. It was found in Section 6.2 that flexibility plays only a small role for orbital small-sat launch vehicles. It is therefore recommended to only consider this more detailed aerodynamic model for sounding rockets such as Stratos III.

The propellant viscosity is currently modelled using a propellant slipping factor, as discussed in Chapter 4. In reality, the contribution of the propellant to the (rotational) inertia of the vehicle is highly dependent on the propellant viscosity and wall roughness of the propellant tank. One model addition for the propellant tanks could be to add different viscosity models for often used propellants such as liquid oxygen (LOX) and refined kerosene (RP-1). Another addition to the propellant tanks could be to refine the slosh rod length calculations. For low fluid levels, the slosh rod equation converges to infinity. To avoid this, the slosh rod length is set equal to the fluid height for low fluid levels. However, this still results in zero divisions when the tank is completely emptied. Saturations, or other models, could be used to model this appropriately. Finally, most of the slosh parameters change dynamically over time. This includes the slosh mass, inertia and natural frequency. The location of the attachment point does not change over time. This was chosen since a fixed attachment point allows for easier finite element analysis. The deflection of the attachment point defines the interaction of the flexibility and the slosh mass. This means that a moving attachment point would require a more detailed analysis of the deflection at each mode.

Currently, the controller is assumed to have complete knowledge of its state. In reality, this knowledge is often limited to a small set of sensors such as GPS and accelerometers. Creating proper sensor (fusion) models would allow for a more accurate representation of the launch vehicle during flight.

Finally, it is recommended to add stage separation through constraints. Currently, once a stage is separated, the mass of the stage is set to zero. Effectively this means that that part of the vehicle has staged. However, it does not allow for tracking of the dropped stage. This might be especially interesting when re-entry profiles are being considered. One way to achieve this within the model would be to apply a constraint between two rigid bodies which is removed once a staging event occurs. Although possible in the current configuration, it would require further extension of the environment model as well to allow for different forces and moments acting on the vehicle.

7.2.2. Research recommendations

In this research, several assumptions have been made. In chapter 6, the aerodynamic coefficients were assumed to be constant for different vehicle configurations. This was mainly done since obtaining detailed aerodynamic coefficients was considered to be outside the scope of this research. The effect of changing aerodynamic coefficients on the slosh-flex-aero interaction was not considered. If the coefficients are available for different configurations, it is recommended to reassess the sensitivity for all the different configurations.

Another assumption was the constant eigenfrequency for a given vehicle. In reality, the eigenfrequency changes over time depending on the fill rate of the vehicle. This requires a more detailed finite element analysis. Although it is assumed that this change in eigenfrequency does not influence the conclusion, it is recommended to validate this claim further.

Finally, it is recommended to further evaluate the effectiveness of optimal control algorithms such as H_∞. It is expected that optimal control algorithms can further decrease the control error. It was shown that gain-scheduled PID controllers showed a significant difference in controller performance between both the rigid and non-rigid body model during stage separation. If an optimal control algorithm designed around a rigid body can increase controller performance, it would further validate the claim that non-rigid body models are not required for small-sat launch vehicles.

7.2.3. Future research

The first recommendation for future research would be to determine the effect of non-rigidity on the orbit insertion. Since the focus would be on orbital launch vehicles, it is recommended to only consider the effect of sloshing in this analysis. Although it was shown that a rigid body PID controller can stabilise the vehicle, large periods of microgravity combined with the slosh masses might decrease the orbital insertion accuracy.

Another recommendation would be to optimise the payload capacity of a given launch vehicle by decreasing

its dry mass and increasing its thrust to weight ratio. One way to achieve this is by decreasing the thickness of the vehicle walls. The would increase the flexibility of the vehicle. Since the non-rigid body model is available, this increase in flexibility can potentially be controlled using more sophisticated (non-linear) control algorithms. It is expected that this would marginally increase the payload capacity of a vehicle.

It was found that flexibility effects become apparent for launch vehicles with length over diameter ratios above 20. Stratos III, with its ratio of 29.3, was well above this value. No flexibility analysis was performed for the complete vehicle. All Stratos III simulations assume a rigid body model. For this vehicle, it is recommended to perform a more detailed analysis of the eigenmodes of the entire vehicle. Limited data was available meaning significant assumptions were required to determine the mass normalised deflection and eigenfrequency of the vehicle. The divergence of the angular rates and body acceleration near the anomaly suggests that there are other effects at play besides sloshing and flexibility. Potentially, this divergence is caused by the deflection of the vehicle, causing the local angle of attack to change, changing the aerodynamic properties of the vehicle. This effect could be checked by performing a more detailed modal analysis on the vehicle, using these values to validate this claim. However, the increase in acceleration compared to the model might suggest that one of the fins sheared off before the anomaly. This would have decreased the drag, resulting in higher acceleration and quick destabilisation of the vehicle.

Another effect might be the unstable combustion, causing an effective thrust that is not pointing through the centre of the vehicle. This could be modelled by applying a random control signal as input to the model, which gives the engine a random offset in the Y_B and Z_B direction. Multiple runs are required to analyse the effect of this combustion instability. It is expected that, combined with the slosh mass, this would (further) destabilise the vehicle.

Stratos III uses no slosh mitigation strategies such as slosh dampers. It was expected that the small diameter of the vehicle would mean that sloshing would have a limited effect on the vehicle. The slosh mass is calculated based on the diameter of the vehicle, as well as the fill ratio of the tank. For Stratos III, the slosh mass can be calculated to be approximately 38 kg for the full tank. In this scenario, the slosh mass at the moment of decreasing thrust was approximately 15 kg. Since this is approximately 10% of the mass of the entire vehicle, it is not unlikely that sloshing contributed to the destabilisation of the vehicle. It was shown in Section 6.2 that slosh damping has no significant influence. It was also shown that the slosh-flex-aero interaction is largely independent of slosh damping in the linear slosh regime that is considered here. For larger changes in body angles, sloshing can become more pronounced than modelled in this non-rigid body simulator. Therefore, it is proposed to consider the use of slosh dampers for future Stratos launch vehicles. In itself, this is expected to have a limited effect. But despite its small tank diameter, a slosh mass of 30-35 kg will otherwise be free to slosh around, causing a maximum shift in C.G. of 3 to 3.5 cm. For a peak thrust of 21 kN, this results in an applied moment of 630 Nm around the pitch and yaw axis.

Finally, it was found in Section 5.3 that the roll control system was not able to stabilise the vehicle in the scenario of a sudden decrease in acceleration. However, an interesting behaviour was observed when this analysis was performed. It was found that the bang-bang roll control system was able to successfully stabilise the roll, pitch and yaw rate. This means that by only controlling one axis of the vehicle, the body becomes significantly more stable. It is therefore recommended for future Stratos vehicles to include the roll control system if no other method of active stabilisation can be used. It is recommended to further research this behaviour.

Bibliography

[1] DAWN Aerospace. Our vision: A vibrant space economy. `https://www.dawnaerospace.com/mission`, . Online - Last accessed: 2020-07-07.

[2] Firefly Aerospace. Aerojet rocketdyne and firefly aerospace to provide flexible access to space. `https://firefly.com/aerojet-rocketdyne-and-firefly-aerospace-to-provide-flexible-access-to-space/`, . Online - Last accessed: 2020-07-07.

[3] E. Amani, M. Ebrahimi, and J. Roshanian. Application of the simple pendulum model to incorporate propellant slosh dynamics in 6-dof launcher flight. *Journal of Space Science and Technology*, 2011.

[4] ArianeGroup. Ariane v - the heavy launcher. `https://www.arianespace.com/vehicle/ariane-5/`, 2021. Online - Last accessed: 2021-04-22.

[5] ArianeGroup. Soyuz - the medium launcher. `https://www.arianespace.com/vehicle/soyuz/`, 2021. Online - Last accessed: 2021-04-22.

[6] G.J. Dominguez Calabuig and A.J.P. van Kleef. Guidance navigation and control concepts for a small satellite launcher. Technical report, Netherlands Aerospace Office, 2016.

[7] Charles Cossette, James R Forbes, and David Saussie. Modular derivation of the equations of motion of a flexible launch vehicle with propellant slosh. In *AIAA Scitech 2020 Forum*, page 1603, 2020. doi: 10.2514/6.2020-1603.

[8] Dr. Ray Millst Dr. Rick Fleeter, Dr. Frank McLoughlin. Increasing space access availability for small payloads: The pacastro launch vehicle. Herndon, VA, 1992.

[9] Delft Aerospace Rocket Engineering. Stratos iii technical overview. `https://dare.tudelft.nl/stratos3/tech/`, 2018. Online - Last accessed: 2021-04-22.

[10] Kevin Eppenga. Non-rigid body effects for launch vehicle ascent models - literature review. 2020.

[11] James Richard Forbes. Identities for deriving equations of motion using constrained attitude parameterizations. *Journal of Guidance, Control, and Dynamics*, 37(4):1283–1289, 2014. doi: 10.2514/1.G000221.

[12] PP Friedmann, JJ McNamara, BJ Thuruthimattam, and I Nydick. Aeroelastic analysis of hypersonic vehicles. *Journal of Fluids and Structures*, 19(5):681–712, 2004.

[13] Dennis Howitt and Duncan Cramer. Introduction to spss in psychology. Harlow, United Kingdom, 2014. Pearson. ISBN: 9781306771344.

[14] Minjiao Li, Xiaoting Rui, and Laith K Abbas. Elastic dynamic effects on the trajectory of a flexible launch vehicle. *Journal of Spacecraft and Rockets*, 52(6):1586–1602, 2015. doi: 10.2514/1.A33181.

[15] Jack J McNamara and Peretz P Friedmann. Aeroelastic and aerothermoelastic analysis in hypersonic flow: past, present, and future. *AIAA journal*, 49(6):1089–1122, 2011.

[16] Erwin Mooij. Robust control of a conventional aeroelastic launch vehicle. *AIAA Scitech 2020 Forum: 6-10 January 2020, Orlando, FL*, 2020. doi: 10.2514/6.2020-1103.

[17] Erwin Mooij and Xuerui Wang. Incremental sliding mode control for aeroelastic launch vehicles with propellant slosh. In *AIAA Scitech 2021 Forum*, page 1221, 2021.

[18] NASA. Launch vehicle / spacecraft key facts. `https://history.nasa.gov/SP-4029/Apollo_18-13_Launch_Vehicle-Spacecraft_Key_Facts.htm`, 2021. Online - Last accessed: 2021-04-22.

[19] Chetan Nichkawde, PM Harish, and N Ananthkrishnan. Stability analysis of a multibody system model for coupled slosh–vehicle dynamics. *Journal of Sound and Vibration*, 275(3-5):1069–1083, 2004. doi: 10.1016/j.jsv.2003.07.009.

[20] Jeb Orr, Matthew Johnson, Jonathan Wetherbee, and James McDuffie. State space implementation of linear perturbation dynamics equations for flexible launch vehicles. In *AIAA Guidance, Navigation, and Control Conference*, page 5962, 2009.

[21] Nikolaos K Pavlis, Simon A Holmes, Steve C Kenyon, and John K Factor. The development and evaluation of the earth gravitational model 2008 (egm2008). *Journal of geophysical research: solid earth*, 117(B4), 2012.

[22] James R Roberts, Eduardo R Basurto, and Pei-Ying Chen. *Slosh design handbook I*, volume 406. National Aeronautics and Space Administration, 1966.

[23] RocketLab. Electron - dedicated access to space for small satellites. `https://www.rocketlabusa.com/rockets/electron/`, 2021. Online - Last accessed: 2021-04-22.

[24] Relativity Space. Terran 1. `https://www.relativityspace.com/terran`. Online - Last accessed: 2020-07-07.

[25] SpaceX. Falcon 9 - first orbital class rocket capable of reflight. `https://www.spacex.com/vehicles/falcon-9/`, 2021. Online - Last accessed: 2021-04-22.

[26] Weihua Su, Cecilia K King, Scott R Clark, Edwin D Griffin, Jeffrey D Suhey, and Michael G Wolf. Dynamic beam solutions for real-time simulation and control development of flexible rockets. *Journal of Spacecraft and Rockets*, 54(2):403–416, 2017. doi: 10.2514/1.A33543.

[27] Leo Timmermans, Niels Bernving, Arnoud van Kleef, Bastien Haemmerli Markus Kuhn, Ilja Müller, Marina Petrozzi, and Geogia Psoni. Small innovative launcher for europe: Results of the h2020 project smile. In 69th *International Astronautical Congress*. Royal Netherlands Aerospace Centre, IAF, October 2018.

[28] Stephen P Timoshenko. Lxvi. on the correction for shear of the differential equation for transverse vibrations of prismatic bars. *The London, Edinburgh, and Dublin Philosophical Magazine and Journal of Science*, 41 (245):744–746, 1921.

[29] Rolf Wubben, Eoghan Gilleran, Krijn de Kievit, Bart Kevers, Maurits van Heijningen, and Martin Christiaan Olde. Isasi 2019 - investigation of the in-flight failure of the stratos iii sounding rocket. 2019.

[30] Dewei Zhang, Hui Qi, Jiangtao Xu, Ya Yang, and Bangsheng Fu. Modeling and analysis of aeroelasticity and sloshing for liquid rocket. *IEEE Access*, 7:4453–4465, 2018. doi: 10.1109/ACCESS.2018.2884544.